Department of Physics
Indian Institute of Technology Guwahati
Ph.D Thesis
June, 2014

Studying Disorder and Correlation Effects on the Phase Diagram of Bosons via Mean Field Theory

Apurba Barman

Supervisor: Prof. Saurabh Basu

Studying Disorder and Correlation Effects on the Phase Diagram of Bosons via Mean Field Theory

A thesis submitted by

Apurba Barman

Supervisor: Prof. Saurabh Basu

to

Indian Institute of Technology Guwahati

in partial fulfillment of the requirements
for the award of the degree of
Doctor of Philosophy in Physics

Department of Physics
Indian Institute of Technology Guwahati
Guwahati - 781039, Assam, India

Statement

The work contained in the thesis entitled "*Studying Disorder and Correlation Effects on the Phase Diagram of Bosons via Mean Field Theory*" has been carried out at the Department of Physics, Indian Institute of Technology Guwahati, India by me under the supervision of Prof. Saurabh Basu. No part of this thesis has been submitted elsewhere for any other degree. Works presented in the thesis are all my own unless referenced to the contrary in the text.

(Apurba Barman)
Department of Physics
Indian Institute of Technology Guwahati
Guwahati - 781039

June 10, 2014

Disclaimer

The bibliography included in this thesis is, by no means complete but contains the ones which are consulted thoroughly by me. I apologize for inadvertently missing out some of the research papers, review articles and other scientific documents pertaining to the focus of this thesis which should also have been cited.

Certificate

It is certified that the work contained in the thesis entitled "*Studying Disorder and Correlation Effects on the Phase Diagram of Bosons via Mean Field Theory*" by Mr. Apurba Barman, a Ph.D student of the Department of Physics, IIT Guwahati was carried out under my supervision and has not been submitted elsewhere for award of any degree.

(Prof. Saurabh Basu)
Department of Physics
Indian Institute of Technology Guwahati
Guwahati - 781039

June 10, 2014

To my parents...

Acknowledgements

First and foremost I would like to thank my supervisor Prof. Saurabh Basu for his able guidance, constant encouragement and support throughout my research work. His immense patience in dealing with me was exemplary. His knowledge and intelligent ideas have helped me to complete the work successfully, well in time. He always gave me freedom to work and encouraged me when I tried something new, which gave me a lot of confidence. The long discussions which we used to have helped me tremendously in solving the problems.

I would like to thank my doctoral committee members Prof. S. B. Santra, Prof. A. Khare and Dr. V. Wagh for reviewing my progress every year and for their frank comments and valuable suggestions. I am thankful to all other faculty members of the Physics department for their friendly behaviour whenever it was needed.

I gratefully acknowledge the help and assistance received from Prof. R. V. Pai, Department of Physics, Goa University during the early days of my Ph.D work.

I am grateful to Indian Institute of Technology, Guwahati for the financial support. I wish to thank Department of Physics, IITG for providing me the necessary computational facilities. I thank all the technical assistants of the department, specially Mr. Basab Bijoy Purkayastha for their assistance in various ways during my research period. I would like to thank all my group members Ravikumar Patta, Sudin, Noor for their cooperation and assistance. I would like to thank seniors Dr. Poulumi Dey, Dr. Biswanath Dutta, Dr. Jahir Abbas Ahmed, Dr. Supriya Roy, Dr. Rahul Das for their help and support. I also thank all of my colleagues and juniors for creating a pleasant work atmosphere. I would like to thank Ms. Sunayana Dutta and Dr. Ayan Khan for their cooperation. Special thanks to Himangsu, Souvik, Deepanwita, Tribedi, Bhargab, Biswajit, Bappaditya, Sujay, Tapas, Kartik, Sourav for their help and entertaining discussions over evening tea sessions.

Finally, I convey my gratitude and thanks to my parents for their unconditional love, constant support and inspiration during my entire career.

Abstract

The thesis investigates the ground state phase diagram of interacting bosons using mean field theory on a Bose Hubbard model (BHM). A number of different relevant issues have been addressed here. They include the effects of the periodic environment of the (optical) lattice on a Bose Einstein condensate. The work nicely portrays the interplay of the condensate properties and symmetry of the underlying lattice vis a vis its coordination number. A work on random disorder with a uniform distribution in a BHM follows. The Bose glass phase is seen to occur as the sites with integer fillings form a percolating cluster in a two dimensional square lattice, with the threshold being very similar to that of a random site percolation model that is well studied in statistical mechanics. The Bose glass phase seems to prolong the superfluid phase and occurs intervening to the superfluid and the insulating phases. Dipolar interactions are hence discussed to include long range (nearest neighbour density exchange) interactions in a BHM. In presence of such extended interactions, a variety of density ordered and supersolid phases are seen to emerge. The thesis has particularly focused on the prototype of a kagome lattice, a classic example of a non-bipartite lattice. As extension of the above study is made to include the harmonic trapping effects which are indispensable in the study of cold atomic gases in optical lattices. The trap renders the system inhomogeneous and a variety of phases, such as the superfluid, Mott insulating, density ordered, supersolid etc. are seen to coexist. The thesis finally concludes with a study of a three component bosonic mixture which shows exotic mixed phases, where one component may exhibit superfluid character while the other two may possess insulating properties. Thus correlation effects which go beyond incorporating interatomic interactions to include the effects of symmetry of underlying lattice, along with disorder effects on a system of interacting bosons form the central focus of the thesis.

List of Figures

List of Tables

List of Publications and Conferences

Publications in Journals (in reverse chronological order):

1. *Phase diagram of trapped bosons in a kagome lattice- application of inhomogeneous mean field theory*,

   Apurba Barman and Saurabh Basu, J. Phys. B: At. Mol. Opt. Phys. **47** 025302 (2014).

2. *Phase diagram of bosons in a tripartite lattice - emergence of exotic density ordered phases*,

   Apurba Barman and Saurabh Basu, J. Phys. B: At. Mol. Opt. Phys. **46** 125303 (2013).

3. *Understanding the Bose glass phase via a percolation scenario*,

   Apurba Barman, S. Dutta, A. Khan, and Saurabh Basu, Eur. Phys. J. B **86** 308 (2013).

4. *Interplay of optical potential and condensate properties for bosons in different optical lattice geometries*,

   Apurba Barman and Saurabh Basu, J. Phys. B: At. Mol. Opt. Phys. **45** 105303 (2012).

Paper Submitted to Journals:

5. *Phase diagram of multi-component bosonic mixtures: emergence of mixed superfluid and insulating phases*,

   Apurba Barman and Saurabh Basu, Submitted to J. Phys. B: At. Mol. Opt. Phys.

6. *Tunneling dynamics of a correlated bosons in a double well potential*,

S. Dutta, **Apurba Barman**, A. Siddharth, A. Khan and Saurabh Basu, Manuscript under preparation.

Publications in Conference Proceedings (in reverse chronological order):

1. *Emergence of Supersolid Order in a Disordered Bose Gas with Harmonic Trapping*,

   Apurba Barman and Saurabh Basu, to be published in AIP Conf. Proc. **1591**, 102 (2014).

2. *Phase diagram of correlated bosons in a tripartite lattice with harmonic confinement*,

   Apurba Barman and Saurabh Basu, to be published in JPS Conf. Proc. (2014).

3. *Interplay of Superfluidity and Lattice Geometry in Bose Systems*,

   Apurba Barman and Saurabh Basu, AIP Conf. Proc. **3149**, 921 (2010).

Conference Presentations (in reverse chronological order):

1. *Three component bosons: exciting possibilities of having mixed superfluid and insulating phases*, Apurba Barman and Saurabh Basu, SCES, July 7-11, 2014, Grenoble, France (accepted for poster presentation).

2. *Emergence of Supersolid Order in a Disordered Bose Gas with Harmonic Trapping*, Apurba Barman and Saurabh Basu, 58^{th} DAE-SSPS, December 17-21, 2013, Thapar University, Patiala, Punjab, India.

3. *Phase diagram of correlated bosons in a tripartite lattice with harmonic confinement*, Apurba Barman and Saurabh Basu, SCES, Auguest 5-9, 2013, Tokyo, Japan.

4. *Role of information entropy in determining the Bose glass phase*, Apurba Barman and Saurabh Basu, Gordon Research Conferences, June 24-29, 2012, Mount Holyoke College, MA, USA.

5. *Interplay of Superfluidity and Lattice Geometry in Bose Systems*, Apurba Barman and Saurabh Basu, 55^{th} DAE-SSPS, December 26-30, 2010, Manipal University, Manipal, Karnataka, India.

Contents

Chapter 1

Introduction

1.1 Optical Lattice

The study of cold atomic systems have seen an extremely intense growing research interest over the last two decades after the realization of the Bose-Einstein condensate (Anderson *et al.*, 1995[1]; Bradley *et al.*, 1995[2]; Davis *et al.*, 1995[3]). The experiments that were developed to achieve temperatures of the scale of a few nano-Kelvin or micro-Kelvin required for attaining Bose-Einstein condensation (BEC), are laser cooling techniques[4], evaporative cooling[5] etc. These kinds of research and development activities have helped in the fundamental progress in the study of a variety of many body phenomena, such as quantum phase transitions, superfluid properties, aspects of matter-wave coherence and collective excitations in trapped Bose gases etc.

The real crystals are usually very complex, due to the presence of Coulomb interactions among carriers, coupling of carriers to lattice vibrations, disorder and impurities present in the crystal etc. In a single theory it is often difficult to take into account all these effects at once and solve such a complicated many body system to our satisfaction. It is also very hard to point out which effects are relevant to describe a particular physical situation of a system and which are not while interpreting the outcome of experiments. An alternative was first developed by Jaksch *et al.*[6] and Greiner *et al.*[7], where the strongly correlated systems can be studied with cold atomic gases by loading them into optical lattices, with the latter being formed by standing waves of counter propagating laser beams. Coupled with techniques to achieve ultracold temperatures, the progress in the research on cold atoms in optical lattices from then on, has expanded in leaps and bounds.

Optical lattices are periodic potentials created by the interference pattern of

counter propagating laser beams by means of light-matter interactions. The atoms interact with the light field. The energy of internal states of an atom depends on the electric field intensity of laser light. Thus the interference pattern which has a spatial dependence, thereby creates a spatially dependent potential, known as an optical potential. Such optical potentials have a regular arrangement of maxima and minima which are separated by a distance of the order of the wavelength of the laser beam used. The neutral atoms can be trapped in these optical potentials when they are sufficiently cooled.

As said earlier, the cooling of atoms can be done via various techniques, such as laser cooling technique[8–11], evaporative cooling process[5] etc. In a laser cooling process, as an atom absorbs a photon from the incident laser beam, it receives an impulse along the direction of the incoming photon and creates an excitation. If the atom emits a photon, it will recoil in the opposite direction. Since emission is a random process, it therefore, may transfer zero momentum due to emission[8]. For red detuned laser (laser frequency is less than that of the atomic transitions), absorption of a photon is only possible when the atom is moving towards the laser field so that the Doppler shift compensates for the detuning. Hence the atom slows down resulting in a loss of kinetic energy and hence low temperatures. This method, sometime also known as "optical molasses" [8]. This process is the simplest way of laser cooling, while other sophisticated methods are also available e.g. Sisyphus cooling[10,12] etc.

The atoms thus cooled, as well can be trapped by the most commonly used device is the magneto-optical trap[10]. The main idea behind it is to use position dependent magnetic field, which induces a position dependent Zeeman-splitting. As a result, the force exerted by the laser beams also becomes position dependent, yielding a net force towards the center of the trap. Note that this trapping potential in general is approximated as harmonic, which makes the system inhomogeneous. To further achieve low temperatures, the method of "forced evaporative cooling" is used. The detailed discussions on cooling methods can be found in Ref.[13].

Cold atoms in an optical lattice potential resemble in many respects with that of electrons in an ion-lattice potential of real crystals studied in solid state physics. But the optical lattices have many advantages with respect to the real crystals. They are defect free and have no impurity. The lattice properties can be controlled easily by laser parameters. For example, the interaction between the atoms can be tuned using a magnetic field via Feshbach resonance (described later). The lattice depth can be controlled by changing the laser intensity, the orientation of the lattice can

be changed by tuning the polarization of the laser light, various lattice geometries such as square, triangular, honeycomb, kagome etc. can be achieved by changing the laser configuration. Also, quite importantly, the lattice spacing is typically 10^3 times larger compared to the real crystals. The atoms or ions play the role of electrons in solid, they hop through the lattice site as electrons would tunnel through a solid. Thus there are enough indications that cold atoms in optical lattices can provide a new paradigm for observing several quantum phenomena.

Let us now briefly discuss the physical principles governing the formation of optical lattices. The interaction between the cold atom and the effective laser field arising out of the interference pattern induces an electric dipole moment on the atoms. The atomic dipole in turn interacts with the electric field of the laser beams and modify the energy level via a phenomenon called as AC Stark effect. We briefly review the physics here.

1.1.1 Dipole Potential

Here we describe how the laser beams interact with the cold atoms and generate trapping potential. Let us consider a time varying electric field of the standing wave produced by counter propagating laser beams as,

$$\mathbf{E}(\mathbf{r},t) = \hat{\mathbf{e}}E(\mathbf{r})e^{-i\omega t}, \tag{1.1}$$

where $\hat{e}$ is the unit vector along the polarization direction, $E(\mathbf{r})$ is the spatial part of the electric field and ω is the driving frequency of the laser beams. When an atom is placed in this electric field, $\vec{E}$, an atomic dipole moment $\mathbf{P}$ is induced that oscillates by the driving frequency ω as,

$$\mathbf{P}(\mathbf{r},t) = \hat{\mathbf{e}}P(\mathbf{r})e^{-i\omega t} \tag{1.2}$$

$P(\mathbf{r})$ is the amplitude of the dipole oscillator. The relation between $P(\mathbf{r})$ and $E(\mathbf{r})$ (of Eq. (1.1)) is given by,

$$P(\mathbf{r}) = \alpha(\omega)E(\mathbf{r}), \tag{1.3}$$

where $\alpha(\omega)$ is the complex polarizability that depends on the driving frequency, ω. The induced dipole moment $\mathbf{P}(\mathbf{r},t)$ interacts with the laser field $\mathbf{E}(\mathbf{r},t)$ and gives rise to an effective potential, $V_{dip}(\mathbf{r})$ which is denoted by,

$$V_{dip}(\mathbf{r}) = -\frac{1}{2}\langle \mathbf{P}(\mathbf{r},t).\mathbf{E}(\mathbf{r},t)\rangle = -\frac{1}{2\epsilon_0 c}Re(\alpha)I(\mathbf{r}) \tag{1.4}$$

here the angular bracket denotes the time average over the rapidly oscillating term. The field intensity is related to the amplitude of the electric field as,

$$I(\mathbf{r}) = \epsilon_0 c |E(\mathbf{r})|^2. \tag{1.5}$$

Therefore the atom feels the potential that is proportional to the field intensity $I(\mathbf{r})$ and the real part of the polarizability. If $I(\mathbf{r})$ is periodic, there will be a number of minima or maxima, providing an environment that is akin to lattice potential for the atom.

The atomic dipole may also absorb energy from the field that leads to heating of the atom, which should be avoided. The scattering rate for the absorption of photons by the dipole is related to the field intensity and the imaginary part of the polarizability as shown in the following

$$\Gamma_{sc}(\mathbf{r}) = \frac{1}{\hbar \epsilon_0 c} Im(\alpha) I(\mathbf{r}). \tag{1.6}$$

Thus the two quantities, that is the effective dipole potential $V_{dip}(\mathbf{r})$ and the scattering rate $\Gamma_{sc}(\mathbf{r})$ play crucial roles for trapping of atoms in an optical lattice.

The field intensity can be easily calculated for a given configuration of laser beams. The polarizability, $\alpha(\omega)$ in general is a complex function of frequency, also depends on the electronic structure of the atoms and needs a quantum treatment. However when the driving frequency, ω, far from the atomic transition frequency, ω_0, it can be calculated by considering the atom in Lorentz's model of a classical oscillator. The detailed derivation of $\alpha(\omega)$ can be found in Ref.[14]. The effective potential and the scattering rate can be expressed as,

$$V_{dip}(\mathbf{r}) = -\frac{3\pi c^2}{2\omega_0^3} \left[\frac{\Gamma}{\delta}\right] I(\mathbf{r}) \tag{1.7}$$

$$\Gamma_{sc}(\mathbf{r}) = \frac{3\pi c^2}{2\hbar^3 \omega_0^3} \left[\frac{\Gamma}{\delta}\right]^2 I(\mathbf{r}) \tag{1.8}$$

where $\delta = \omega - \omega_0$ denotes the detuning parameter. The following observation can be made from the above two equations, which are important for practical uses:

• *Sign of detuning*: If $\delta < 0$ ("*red detuned*"), the dipole potential is negative and hence atoms are attracted to the potential minima, that is, regions with maximum field intensity $I(\mathbf{r})$. For $\delta > 0$ ("*blue detuning*"), the case is opposite and atoms are attracted towards the maximum intensity region.

• *Scaling with intensity and detuning*: The dipole potential scales as $\frac{I}{\delta}$, whereas the

scattering rate scales as $\frac{I}{\delta^2}$. To minimize the scattering rate and for a reasonable potential depth, one has to use high intensity and large detuning δ.

The other way to calculate the atomic polarizability is by considering the atoms as a two-level quantum system interacting with the classical radiation field in a semi-classical approach. In this approach, the damping rate Γ (corresponding to the spontaneous decay rate of the excited level) can be determined by the dipole matrix element between the ground state $|g\rangle$ and the excited state $|e\rangle$ as,

$$\Gamma_{sc}(\mathbf{r}) = \frac{\omega_0^3}{3\pi\epsilon_0\hbar c^3}|\langle e|\hat{\mu}|g\rangle|^2 \tag{1.9}$$

where $\hat{\mu}$ is the dipole operator. When the intensity of the driving field is very high, the excited state gets strongly populated, and the classical treatment fails to be valid[14].

1.1.2 The AC Stark Shift

In general, neutral atoms do not have an electric dipole moment. The interaction between the neutral atoms and the electric field of laser beams can induce an dipole moment by means of an AC Stark effect[14,15]. To describe the process, consider the effect of far-detuned laser light on a two level atom. The energy shift of the internal atomic states can be obtained from the second order energy correction, treating the electric field as a perturbation. The amount of energy shift can be shown (for non-degenerate states) to be

$$\Delta\epsilon = \sum_{i\neq j} \frac{|\langle i|H_{int}|j\rangle|^2}{\epsilon_i - \epsilon_j} \tag{1.10}$$

where $H_{int} = -\hat{\mu}.\mathbf{E}$ is the interactions between a single atom and the laser field with $\hat{\mu} = -e\mathbf{r}$ represents the atomic dipole operator, $\mathbf{E}$ is the laser field and ϵ_i are the energies of the atom in presence of a laser field. Here the ground state energy is the sum of the internal energy of the atom, which is zero, and the laser field energy $n\hbar\omega$ for n photons that yields a total energy $\epsilon_i = n\hbar\omega$ for the unperturbed ground state $|i\rangle$. When the atoms absorb a photon from the electric field, the total energy of the combined system becomes,

$$\epsilon_j = n\hbar\omega_0 + (n-1)\hbar\omega = -\hbar\delta_{i,j} + n\hbar\omega \tag{1.11}$$

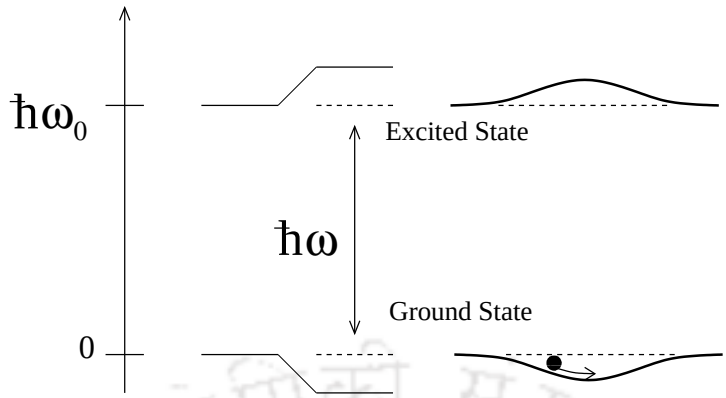

Figure 1.1: AC Stark shift for a two-level atom due to light-matter interaction. ω and ω_0 are the laser frequency and atomic transition frequency respectively. Red-detuned light ($\delta < 0$) shifts the ground state down and excited state up by same amount (in left) with respect to unperturbed situation. A Gaussian laser beam produces a ground state potential well, in which an atom can be trapped (right). The Figure is extracted from Ref.[14].

where $\delta_{i,j} = \omega - \omega_0$ is the detuning parameter. Thus for a two level atomic system with an internal ground state $|g\rangle$ ($= |i\rangle$) and an excited state $|e\rangle$ (a specific $|j\rangle$), Eq. (1.10) reduces to

$$\Delta\epsilon = \pm\frac{|\langle e|\mu|g\rangle|^2}{\delta}|E|^2 = \pm\frac{3\pi c^2}{2\omega_0}\frac{\Gamma}{\delta}I. \tag{1.12}$$

The upper and lower signs stand for ground and excited states respectively (see Fig. 1.1) where we have used the relation $I = 2\epsilon_0 c|E(\mathbf{r})|^2$. Thus the energy shift due to AC stark effect is directly proportional to the light intensity. Therefore, a spatially dependent light field can be used to generate different variation of the intensity profile, which equivalently can be thought of as a variety of potential wells in which the atoms can be trapped in its ground state at very low temperatures, as shown in Fig 1.1. In a similar way, the perturbation theory can be extended for the case of multi-level systems. The energy shift for multi-level systems further depends on the polarization of the light, magnetic sub-level m_F of a certain hyperfine ground state F. In a previous study[14], it was found that the *linearly polarized light* is usually a better choice for a dipole trap for the multi-level alkali atoms, the detailed discussion of which can be found in Ref.[14].

1.1.3 Lattice Geometry

We have discussed how artificial crystals can be formed by light and atom interaction, where atoms feel spatially dependent periodic potential due to AC Stark

effect. A variety of lattice geometries for the trapping potential can be formed with different configurations of laser light sources, which in turn may prove to be very useful for simulation of different condensed matter systems. The periodic potential can be formed by creating a standing wave profile formed by the interference pattern of two counter propagating laser beams. It is possible to generate various kinds of optical lattices by using different frequencies and orientations for each pair of the laser beams in one, two, or three dimensions. For example, consider two counter-propagating laser beams having frequency ω_L, wavelengths $\lambda_{1,2}$ and corresponding wavevectors $k_{1,2}$. If both the beams are linearly polarized, the resultant electric field in the x direction can be written as,

$$\mathbf{E} = E_0 \left[\hat{\mathbf{e}}_\mathbf{1} e^{i(k_1 x - \omega_L t)} + \hat{\mathbf{e}}_\mathbf{2} e^{-i(k_2 x + \omega_L t)}\right] \tag{1.13}$$

where $\hat{\mathbf{e}}_\mathbf{1}$ and $\hat{\mathbf{e}}_\mathbf{2}$ are the polarization vectors for the two beams and E_0 is the amplitude of the electric field. The field intensity, I, can be found as,

$$\begin{aligned} I \propto |\mathbf{E}|^2 &= E_0^2 \left[\hat{\mathbf{e}}_\mathbf{1} e^{i(k_1 x - \omega_L t)} + \hat{\mathbf{e}}_\mathbf{2} e^{-i(k_2 x + \omega_L t)}\right] . \left[\hat{\mathbf{e}}_\mathbf{1} e^{i(k_1 x - \omega_L t)} + \hat{\mathbf{e}}_\mathbf{2} e^{-i(k_2 x + \omega_L t)}\right]^* \\ &= 2E_0^2 \left[1 + \hat{\mathbf{e}}_\mathbf{1}.\hat{\mathbf{e}}_\mathbf{2} \cos(k_1 + k_2)x\right] . \end{aligned} \tag{1.14}$$

The atoms effectively feel the lattice potential, $V_{opt}(x) \propto I$. In Eq. (1.14), the last term corresponds to the interference between the two beams, and it vanishes if the polarizations of the two beams are orthogonal. For linearly polarized beams having same frequency, ω and wavevector, k, the time-averaged potential is hence given by

$$V_{opt}(x) \propto E_0^2 (1 + \cos 2kx). \tag{1.15}$$

In similar way, a periodic potential in higher dimensions can be created by super-imposing additional pairs of laser beams in different directions. For example, two orthogonal sets of counter-propagating beams the lattice potential takes the form,

$$V_{opt}(x, y) \propto E_0^2 \left[\cos^2(kx) + \cos^2(ky) + 2\hat{\mathbf{e}}_\mathbf{1}.\hat{\mathbf{e}}_\mathbf{2} \cos\phi \cos(kx) \cos(ky)\right] \tag{1.16}$$

where ϕ is the temporal phase between them, and $\hat{\mathbf{e}}_\mathbf{1}$ and $\hat{\mathbf{e}}_\mathbf{2}$ are the polarizations of the two laser beams along x and y directions respectively. The interference term in Eq. (1.16) only arises if the two lasers are coherently coupled, which can be avoided by choosing orthogonal polarization vectors and by using slightly different wavelengths for the standing wave.

Two and three dimensional optical lattices can be formed by superimposing two or three mutually perpendicular standing wave from two sets of counter propagation laser beams respectively having orthogonal polarizations. If the polarization vectors are not orthogonal but the laser frequencies are the same, they interfere and the optical potential changes depending on the relative phase of the beams. This leads to a variation of the geometry of the lattice having a checker board like pattern. A simple square lattice with one atomic basis can be created by choosing orthogonal polarizations between the standing waves. In this case the interference term vanishes and the resulting potential is just the sum of two superimposed 1D lattice potentials. A variety of two dimensional (2D) lattices can be created from the interference of three laser beams by changing their orientations and signs of the detuning parameter[16]. An elaborate discussion on the latter is included in chapter 2.

1.1.4 Atomic Interactions in an Optical Lattice and Feshbach Resonance

Interactions between the atoms play a crucial role in order in determining the principles of many body physics. Excellent control on a system of ultracold atoms in optical lattices implies the possibility of tuning the interaction among the atoms. In solid state physics, the origin of two particle interactions is short ranged arising due to a Van der Waals force and is often described by a Lennard-Jones potential which falls of $U(r-r^{'}) \propto \frac{1}{|r-r^{'}|^6}$. In cold atomic systems, at sufficiently low temperatures the interactions present in the cold atomic gases are also short ranged and may completely be described by the s-wave scattering length a_s. The two body interactions can be denoted by short range pseudopotential as,

$$U(r-r^{'}) \simeq \frac{4\pi\hbar^2 a_s}{2M_r}\delta(r-r^{'}) \tag{1.17}$$

where M_r is the reduced mass and the two-body s-wave scattering length, a_s can be tuned via a Feshbach resonance.

To make the discussion complete, we provide a brief note on the Feshbach resonance here. The direct way to control the interaction between the atoms in ultracold gases are Feshbach resonance, which allows an increase of the scattering lengths beyond the average interparticle spacing[17]. A Feshbach resonance in a two particle collision process appears when the bound molecular state in the closed channel en-

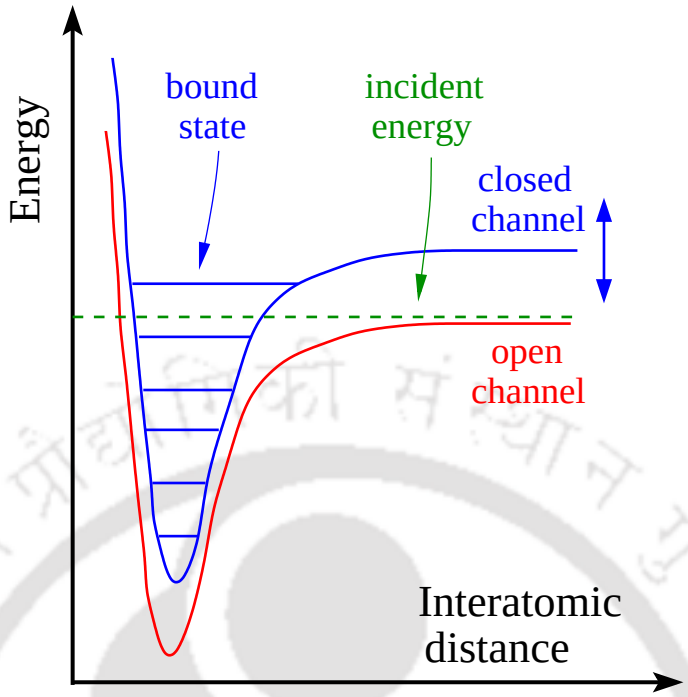

Figure 1.2: Figure from Ref.[17]. The two-channel model for a Feshbach resonance. Atoms prepared in the open channel, corresponding to the interaction potential $V_{op}(r)$ (red line), undergo a collision at low incident energy. In the course of the collision, the open channel is coupled to the closed channel V_{cl} (blue line). When a bound state of the closed channel has an energy close to zero, a scattering resonance occurs. The position of the closed channel can be tuned with respect to the open one, e.g., by varying the magnetic field B.

ergetically approaches the scattering state in the open channel (see Fig. 1.2). Then even weak coupling can lead to strong mixing between the two channels. The energy difference can be controlled by changing the magnetic field when the corresponding magnetic moment are different. The magnetically tuning method is the common way to achieve resonant coupling and it has numerous applications[18]. In a magnetically tuned Feshbach resonance, the s-wave scattering length, a_s as a function of the magnetic field B is given by[19],

$$a_s(B) = a_{bg}\left(1 - \frac{\Gamma}{B - B_0}\right) \tag{1.18}$$

where a_{bg} is the background scattering length associated with the interaction potential of the open channel and represents the off-resonant value. The parameter B_0 denotes the resonance position where the scattering length diverges ($a \to \infty$) and Γ is the resonance width[18]. Fig. 1.3 shows a schematic plot of the resonance expression. It can be noted that both a_{bg} and a_s can be negative or positive, which

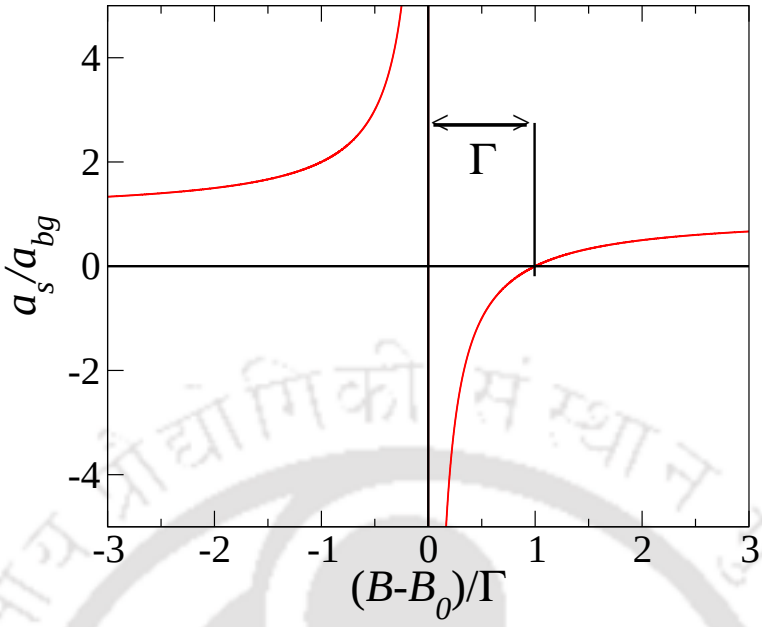

Figure 1.3: The variation of the (normalized) scattering length, a_s/a_{bg} as a function of magnetic field, B in a magnetically tuned Feshbach resonance.

means both attractive and repulsive interactions can be realized. Alternatively, Feshbach resonance can be achieved by optical methods, leading to optical Feshbach resonances that are very similar to the magnetically tuned ones.

1.1.5 Disorder in an Optical Lattice

The optical lattices offer an ultra-clean environment, and hence are defect-free, besides being free of phonons, and thus have the advantage over the conventional crystal lattices. Abilities to control the interparticle interaction potential make it possible to incorporate disorder in these systems with precisely tunable disorder strengths. The disorder in optical lattices can be generated by means of speckle lasers[20–23], two-colour superlattices[24–26] and other means[27].

A speckle is the random intensity pattern produced by a coherent laser light when scattered from a rough surface. Hence the resultant intensity pattern is characterized by a spatially modulated phase and amplitude of the electric field vectors. Such partial waves with no definite phase relationship among each other, originating from different scattering sites of the rough surface, interfere at any spatial position leading to constructive or destructive interferences[28]. This produces a high contrast pattern of randomly distributed grains of light. A fully developed speckle pattern is created when the rough surface contains sufficient number of scatterers to diffuse all the

incident light so that there is no directly transmitted light.

In the case of two colour superlattices, a nonuniform lattice potential is generated by superposing two collinear laser standing waves with different wavelengths of the laser beams[24]. The interference pattern of such standing waves produces a superlattice with a sinusoidal modulation of the depth of the lattice potential. More complex topologies can be realized experimentally by using a superposition of several laser beams with different wavelengths[29].

An immediate task is to utilize all the information collected so far and look for a simple model for a fluid of interacting bosonic atoms on a (optical) lattice. The following discussion will serve our purpose.

1.2 Ultracold Atoms on Optical Lattice and Bose Hubbard Model

In 1989 a simple model was proposed by Fisher *et al.*[30] for interacting bosons in a lattice potential. The model is known as Bose Hubbard model (BHM) which is capable of predicting a quantum phase transition from a superfluid (SF) to a Mott insulating phase (MI) at zero temperature[30]. The SF (MI) phase characterized by a non-zero (zero) SF order parameter and finite (vanishing) compressibility. A detailed discussion is included in the next subsection.

The Hamiltonian in its second quantization formulation reads,

$$H = -t\sum_{\langle i,j\rangle}(b_i^\dagger b_j + h.c.) + \frac{U}{2}\sum_i \hat{n}_i(\hat{n}_i - 1) + \sum_i(\epsilon_i - \mu)\hat{n}_i \qquad (1.19)$$

where the angular bracket indicates i and j as nearest neighbouring sites, $b_i^\dagger$ (b_i) creates (annihilates) a boson on site i, and $\hat{n}_i = b_i^\dagger b_i$, is the local density operator for bosons. The first term is the kinetic energy, describing the hopping with strength t between the neighbouring sites. The second term determines the onsite interaction energy between the bosons. The parameter U measures the strengths of interaction at a site i. In last term, chemical potential energy, μ controls the number of particles in the system and ϵ_i is the random onsite energy that may be used to model disorder. At this stage there is no way to ascertain the explicit presence of an optical lattice in the system under consideration, however the connection can be understood in the following sense (that also paves the way of our dealing with the interacting Bose gas on a lattice).

In 1998, Jaksch *et al.*[6] realized that the dynamics of cold atoms in optical lattices can be described by BHM with a excellent control on the Hamiltonian parameters by tuning the properties of the laser field. The Hamiltonian can be simulated with a great accuracy by loading bosonic atoms in an optical lattice to study SF-MI transition at $T = 0$ by varying the depth of the optical potential[6]. The atoms are thus held together by a trapping potential, V_T along with an optical lattice potential, V_0 thereby confining the atoms to individual lattice sites. As mentioned earlier, the interaction between the ultracold atoms are mostly determined by the s-wave scattering length a_s. The resulting many body Hamiltonian is given by,

$$\begin{aligned} H = & \int d^3x \psi^\dagger(x) \left(-\frac{\hbar^2}{2m}\nabla^2 + V_0(x) + V_T(x) \right) \psi(x) \\ & + \frac{1}{2}\frac{4\pi a_s \hbar^2}{m} \int d^3x \psi^\dagger(x)\psi^\dagger(x)\psi(x)\psi(x). \end{aligned} \tag{1.20}$$

Expanding the bosonic field operators ψ and $\psi^\dagger$ in site localized Wannier basis as[31],

$$\psi(x) = \sum_i w(x - x_i) b_i \tag{1.21}$$

where $w(x-x_i)$ represents the Wannier orbitals localized at site x_i. Considering the lowest vibrational states (assuming the energy scale involved is sufficient up to the excitation energy of the first band), Eq. (1.20) reduces to the BMH in Eq. (1.19), where the Hamiltonian parameters are defined as,

$$t = -\int d^3x \; w^*(x - x_i) \left[-\frac{\hbar^2}{2m}\nabla^2 + V_0(x) \right] w(x - x_j) \tag{1.22}$$

$$U = \frac{4\pi a_s \hbar^2}{m} \int d^3x \; |w(x)|^4. \tag{1.23}$$

In the limit $V_0 \gg E_r$ (E_r is the recoil energy of the atom), where a single band approximation is valid, the hopping parameter, t can be obtained as[32],

$$t = \frac{4}{\sqrt{\pi}} E_r \left(\frac{V_0}{E_r} \right)^{\frac{3}{4}} e^{-2\sqrt{V_0/E_r}}. \tag{1.24}$$

Also the form of the onsite interaction parameter, U in terms of V_0 and E_r is given by the equation,

$$U = \frac{8}{\sqrt{\pi}} E_r k a_s \left(\frac{V_0}{E_r} \right)^{\frac{3}{4}} \tag{1.25}$$

a_s being the s-wave scattering length and k is the wave vector of the laser field.

After such a connection being established between the BHM and atoms in an optical lattice, the signature of SF-MI quantum phase transition was observed experimentally by Greiner *et al.*[7] in 2002 in a gas of ultracold 87^Rb atoms in three dimensional optical lattice. This observation of the quantum phase transition from a SF to a MI phase has offered a first glimpse of the plethora of physical phenomena that were awaiting. Later on the SF-MI phase transition was found also in 1D[33] and 2D[34]. Thereafter, the theoretical studies of cold atomic gases have dramatically increased. These include the theoretical studies of disordered bosonic system[35–38] multi-component Bose mixture[39–41] Bose-Fermi mixture[42,43]. Besides, a large number of analytical and computational methods are proposed to study the BHM such as, strong coupling expansion[44,45], projection method[46,47], mean field theories (MFT)[48–54], Gutzwiller approach[46,55], quantum Monte Carlo (QMC) method[56–62] etc.

Recent progress in the experiments with cold Chromium atoms[63] suggested that an extension to the BHM is experimentally relevant. Unlike the alkali atoms, which have been used in most of the optical lattice experiments so far, ^{52}Cr atoms have a large dipole moment which leads to long range dipolar interactions. This makes ^{52}Cr atoms in an optical lattice a potentially ideal system for experimentally exploring the phase diagram of the BHM with long range interactions, known as the extended Bose Hubbard model (EBHM). To understand the effect of longer range repulsive interactions among the atoms, an intersite potential term of the form, $V\sum_{\langle i,j\rangle} n_i n_j$ is added to the Hamiltonian in Eq. (1.19) that takes into account the interaction between nearest neighbors, a scenario that is capable of giving rise to a rich quantum phase diagram, which should be experimentally accessible. A large number of theoretical studies have been carried out to investigate the possibility of different exotic phases in the EBHM[64–67].

1.2.1 SF-MI Transition

As emphasized in the preceding discussion, at zero temperature, bosons in a periodic potential exhibit two type of phases: a superfluid phase and a Mott insulating phase[30]. In the context of the BHM, let us see what it means. The model is characterized mainly by two energies. One is the tunneling energy, t which determines the probability amplitude of an atom to hop from a lattice site to another neighbouring site and the onsite interaction energy, U which is the interaction energy

between the atoms located in the same site. Depending upon the strengths of these parameter, the physics described by the BHM can be divided into two separate regimes. One is the kinetic energy dominated regime when the onsite interaction is small compared to the hopping amplitude, where the ground state is a superfluid as it tries to delocalize the bosons over the entire lattice. In the opposite limit, where onsite interaction supersedes the tunneling energy, the ground state is in the MI phase in which the bosons are localized and each lattice site having an integer occupation density.

When the kinetic energy term dominates the Hamiltonian, that is, when the tunneling amplitude is sufficient to delocalized the bosons, quantum correlation can be ignored and the system can be described by a macroscopic wavefunction (since the many body state is a product over single identical particle wavefunctions). There is a macroscopic well defined phase and the system is a superfluid. This is because when atoms are delocalized over the lattice with equal relative phases between adjacent sites, they exhibit an interference pattern from an array of phase coherent matter wave sources[68]. As interaction increases, the average kinetic energy required for an atom to hop from one site to the next becomes insufficient to overcome the potential energy cost. Thus atoms tend to get localized at individual lattice sites and number fluctuations are suppressed. Hence in the MI phase, the ground state of the system, instead consists of localized atomic wavefunctions with a fixed number of atoms per site. The lowest lying excitations that conserve particle number (U(1) symmetry) are the particle-hole excitations. This phase is characterized by the existence of an energy gap. The gap is determined by the energy necessary to create one such particle-hole pair.

In experiments, the SF-MI transition was observed by Greiner *et al.*[7] by loading ^{87}Rb atoms from a Bose-Einstein condensate into a three dimensional optical lattice potential. The condensate is a superfluid, where bosons can tunnel from one site to the next. When the lattice potential is turned on smoothly, the system remains in the SF phase, till the interaction between the atoms are small compared to tunneling strength. If the lattice potential depth is increased, the repulsive interaction between the atoms becomes large compared to the tunneling term, which whence induces the superfluid to a Mott insulator transition. In the MI phase the total energy is minimized when each lattice site is filled with a fixed numbers of bosons. Hence the fluctuation in atom number reduces on each site, leading to enhanced fluctuation in the phase of the wavefunction[69]. Thus the phase coherence is lost. These feature was observed in the experiment by recording absorption images af-

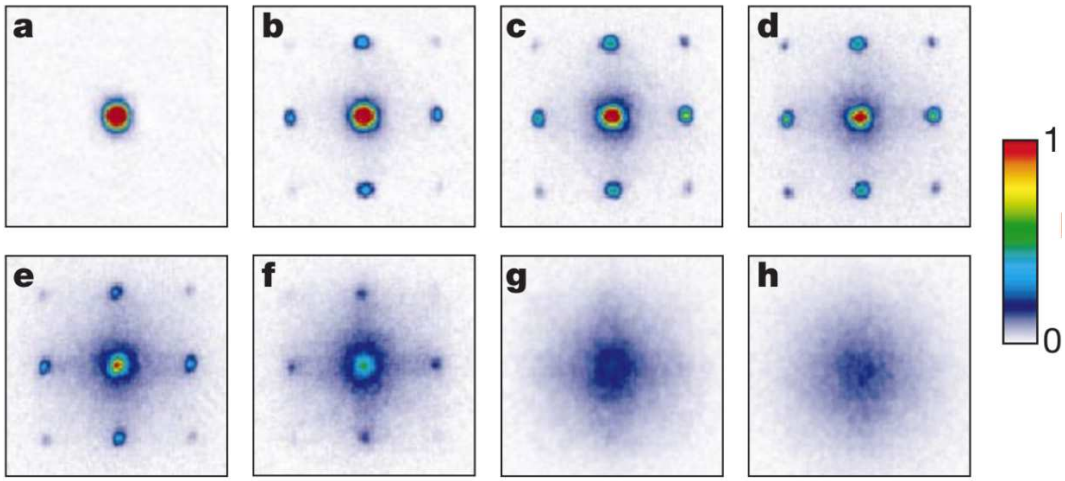

Figure 1.4: Figure from Ref.[7] of absorption images of multiple matter wave interference patterns of ultracold atoms released from an optical lattice across the superfluid to Mott insulator transition. As one goes from a to h, the depth of the lattice potential is increased. The time interval of imaging is fixed at $\tau = 15ms$. The SF phase yields to sharp interference peaks, the vanishing of pattern indicating transition to MI phase (g and h etc.).

ter suddenly releasing the atoms from the lattice potential at an interval of time $\tau = 15ms$. The respective images corresponding to the different values of the lattice potential depth are presented in Fig. 1.4 from Ref.[7]. The absorption images confirm the signature of SF-MI phase transition. When the depth of the potential is relatively small, the atoms have a reasonable kinetic energy. Hence the system is in superfluid state which signals the emergence of coherent matter waves during the expansion and appears as Bragg-like interference pattern provided by the absorption images (Fig. 1.4). With increasing the potential depth, sharp peaks in the absorption pattern vanish, indicating the transition to a Mott insulator phase. Further the critical ratio $(U/t)_c$ at which SF-MI transition occurs obtained from the experiment is in good agreement with the theoretical prediction[6,30,70,71].

1.2.2 Bose Glass Phase

Motivated by the experimental results on superfluidity in ^4He on Vicor glass[72], Fisher *et al.*[30] discussed the behaviour of bosons with short range interactions moving in random external potentials. Unlike the SF and MI phase for pure system, a Bose glass (BG) phase intervening to SF and MI phases, was predicted in presence of disorder[73]. The BG phase is characterized by a gap in the particle-hole excitations, however finite compressibility, but the system is still an insulator be-

cause of the localization effect of the random potential[30]. In this study it was argued that a direct transition between SF and MI phase was unlikely, though not fundamentally impossible. Since then, a large number of analytical, computational and experimental studies have been carried out for finding the correct answer about the location and nature of the BG phase and in many cases reaching contradicting conclusions[44,74–82].

The emergence of BG phase along with SF and MI phases described by the disordered BHM in its parameter space can be understand as follows. When the interaction is sufficiently strong and the total number of bosons is an integral multiple of the number of lattice sites, the model should describe a Mott insulator. In this phase, the bosons are strongly localized in the potential wells of the optical lattice. When both interaction and disorder strengths are weak, the model should describe a superfluid phase. In presence of disorder, depending on the system parameters, the BG phase appears and can be described either by localized single particle states or as an isolated superfluid region. The BG does not allow phase coherence to extend over the entire lattice, and as mentioned before, is characterized by a finite compressibility and gapless particle-hole excitations.

1.2.2.1 Theorem of Inclusions

A rigorous proof for the absence of a direct transition between a SF phase to an MI phase is given by Pollet *et al.*[73] in form of a theorem referred to as *'theorem of inclusions'*. The theorem asserts that *'rare regions'* of the competing phases always exist on either side of the transition line corresponding to a generic bounded disorder. Thus a BG phase will always intervene between the superfluid and the Mott insulator.

Numerical simulations using Worm algorithm Monte Carlo techniques have further provided important leads, where a critical value of the onsite interaction parameter, U (see Eq. (1.19)) is proposed for a direct transition from superfluid to a Mott insulator phase in presence of weak disorder. Summarizing the criterion, a direct transition from SF to MI phase is possible for $U > U_c^{(0)}$ ($U_c^{(0)}$ being the Mott transition point of the pure system) for weak disorder, where the disorder first destroys the Mott insulator, turning it into a compressible Bose glass and this will inevitably happen when the disorder strength (call it Δ_c, where Δ characterize the disorder potential) is greater than $E_g(U)/2$, where E_g is the Mott gap in the pure system at a given value of U.

1.3 Methods of Solution of the BHM

The techniques that are applied to study the BHM (or equivalent model, such as model in presence of disorder, long range interaction, trapping potential etc.) have included a large number of approaches. For example exact diagonalization (ED) method[6,83,84], MFT[70,71,85–88], QMC schemes[61,89–93] etc.

In this section, we review a few important methods that are used to solve and find the ground state of the BHM for a minimal characterization of the system by evaluating certain correlation functions. First we shall describe the simplest way (but numerically intense) of solving bosonic Hamiltonian exactly, known as exact diagonalization. This method is not suitable for large systems because of the exponential growth of the Hilbert space with increase in the system size. A mean field scheme can reduce the complexity of the problem by decoupling appropriate term in the Hamiltonian. A Bogoliubov approach is one of such scheme which decouple the interaction term. But it is unable to capture the SF-MI phase transition. This method turns out very useful for enumerating condensate properties of a quantum fluid in regime of weak interactions. A site decoupled mean field scheme based on the decoupling of the hopping term succeeds in providing a SF-MI phase transition. The method was first proposed by Sheshadri *et al.*[70] to study a homogeneous system. Latter it was extended to the inhomogeneous cases[88,94]. This approach is analogous to the the Gutzwiller method, which was first introduced to study the fermionic Hubbard model and then applied to the bosonic cases[6,85]. The QMC approach employs a wide class of techniques, some of which are statistically exact because they give unbiased estimates of physical quantities. Recently one most common QMC approach used to study bosonic system is based on the Worm algorithm[95].

It may be noted that we have used only a couple of techniques in this thesis to solve the BHM that are simple, but efficient, however, for the sake of completeness, present brief notes on a few other techniques that are mentioned above and have widely been used.

1.3.1 Exact Diagonalization

Here we briefly review the ED method. The procedure for diagonalizing the Hamiltonian is the following:
First choose the basis of the Hilbert space of the system. Let for the system consists of D states, the basis is $\{|\Phi\rangle\}_{j=1,....,D}$.
Construct the matrix representation of the Hamiltonian in the chosen basis by com-

puting the matrix element as $H_{i,j} = \langle\Phi_j|H|\Phi_j\rangle$. The dimension of the matrix is $D \times D$.

Find the set eigenvalues and eigenvectors $\{E_j, |V_j\rangle\}_{j=1,....,D}$ by diagonalizing the matrix $H_{i,j}$.

The lowest eigenvalue is identified as the ground state energy E_{gs} of the system and corresponding eigenvector $|V_{gs}\rangle$ is the ground state wavefunction in the basis $\{|\Phi\rangle\}_{j=1,....,D}$ as given by,

$$E_{gs} = \min\ (E_j)_{j=1,....,D} \tag{1.26}$$

$$H|V_{gs}\rangle = E_{gs}|V_{gs}\rangle. \tag{1.27}$$

Any observable that is describable through an operator $\hat{A}$ can be computed by taking an expectation value on the ground state, $|\Psi_0\rangle$ as,

$$\langle\Psi_0|\hat{A}|\Psi_0\rangle = \sum_{j=1}^{D} |V_{gs}^j|^2 \langle\phi_j|\hat{A}|\phi_j\rangle. \tag{1.28}$$

For a system of N_s lattice sites with N bosons, the dimension of the Hilbert space is given by,

$$D = \frac{(N + N_s - 1)!}{N!(N_s - 1)!}. \tag{1.29}$$

From the above equation it can be seen that even for a small lattice and having few bosons, the value of the D is large. For example, a system having $N_s = 16$ lattice sites with one boson per site, the dimension D is 300540195.

1.3.2 Bogoliubov Approximation

In this subsection we review the Bogoliuvov approach (BA) based on Ref.[71] which is applicable in the weak interaction regime. We consider a BHM as in Eq. (1.19) on a d-dimensional hypercubic lattice with spacing a. The Hamiltonian can be transformed in momentum space by introducing the the operators $b_{\mathbf{k}}^\dagger$ and $b_{\mathbf{k}}$ as,

$$b_i = \frac{1}{\sqrt{N_S}} \sum_{\mathbf{k}} a_{\mathbf{k}} e^- i\mathbf{k}.\mathbf{r}_i, \quad b_i^\dagger = \frac{1}{\sqrt{N_S}} \sum_{\mathbf{k}} a_{\mathbf{k}}^\dagger e^- i\mathbf{k}.\mathbf{r}_i \tag{1.30}$$

where N_s is the total number of lattice sites. Using the above transformation the Hamiltonian in momentum space can be written as,

$$H = \sum_{\mathbf{k}} (\bar{\epsilon} - \mu) a_{\mathbf{k}}^\dagger a_{\mathbf{k}} + \frac{1}{2}\frac{U}{N_s} \sum_{\mathbf{k},\mathbf{k}'} \sum_{\mathbf{k}'',\mathbf{k}'''} a_{\mathbf{k}}^\dagger a_{\mathbf{k}'}^\dagger a_{\mathbf{k}''} a_{\mathbf{k}'''} \delta_{\mathbf{k}+\mathbf{k}'} \delta_{\mathbf{k}''+\mathbf{k}'''}. \tag{1.31}$$

In the weak coupling regime, we can consider the number of condensate atoms $N_0 = \langle a_{\mathbf{k}}^\dagger a_{\mathbf{k}} \rangle_{\mathbf{k}=0}$ is much larger than one. Choosing the expectation value of $a_{\mathbf{k}=\mathbf{0}}^\dagger$ and $a_{\mathbf{k}=\mathbf{0}}$ (call them as $a_0^\dagger$ and a_0 respectively) to be real, the BA consists of replacing these operators with their average plus a fluctuation that are denoted by,

$$\begin{aligned} a_{\mathbf{0}} &\rightarrow \sqrt{N_0} + a_{\mathbf{0}} \\ a_{\mathbf{0}}^\dagger &\rightarrow \sqrt{N_0} + a_{\mathbf{0}}^\dagger. \end{aligned} \tag{1.32}$$

The above substitution up to second order in bosonic operators yields an effective Hamiltonian in $\mathbf{k}$-space of the type,

$$H^{eff} = -\frac{1}{2} U n_0 N_0 + \frac{1}{2} \sum_{\mathbf{k}} [\omega_{\mathbf{k}} - (\epsilon_{\mathbf{k}} + U n_0)] + \sum_{\mathbf{k}} \omega_{\mathbf{k}} b_{\mathbf{k}}^\dagger b_{\mathbf{k}} \tag{1.33}$$

where,

$$\omega_{\mathbf{k}} = \sqrt{\epsilon_{\mathbf{k}}^2 + 2 U n_0 \epsilon_{\mathbf{k}}} \tag{1.34}$$

$$|v_{\mathbf{k}}|^2 = |u_{\mathbf{k}}|^2 - 1 = \frac{1}{2} \left(\frac{\epsilon_{\mathbf{k}} + U n_0}{\omega_{\mathbf{k}}} - 1 \right) \tag{1.35}$$

$\omega_{\mathbf{k}}$ refers to the quasiparticle dispersion (these are called as Bogoliubov quasiparticles). The detailed derivation leading to the above form is given in chapter 2. To obtain the total density, n of bosonic atoms, we note that n consists of two parts − the condensate density, n_0 and the excited state density ($\mathbf{k} \neq 0$)

$$\begin{aligned} n &= \frac{1}{N_S} \sum_{\mathbf{k}} \langle a_{\mathbf{k}}^\dagger a_{\mathbf{k}} \rangle_{H^{eff}} \\ &= n_0 + \frac{1}{N_S} \sum_{\mathbf{k} \neq 0} \left[(|u_{\mathbf{k}}|^2 + |v_{\mathbf{k}}|^2) \frac{1}{e^{\beta \omega_{\mathbf{k}}} - 1} + |v_{\mathbf{k}}|^2 \right] \end{aligned} \tag{1.36}$$

where $\langle .. \rangle_{H^{eff}}$ denotes the expectation values calculated with respect to the effective Hamiltonian H^{eff}. At zero temperature, the condensate density is related to the total density in the following manner,

$$n = n_0 + \frac{1}{N_s} \sum_{\mathbf{k} \neq 0} \left(\frac{\epsilon_{\mathbf{k}} + U n_0}{2\, \omega_{\mathbf{k}}} - \frac{1}{2} \right). \tag{1.37}$$

Eq. (1.37) can be used to calculated the condensate fraction n_0/n for different filling factor n as a function of interaction parameter.

1.3.3 Other Mean Field Techniques

In this subsection we shall review the site decoupling mean field techniques for Bose Hubbard model[70,88,96,97]. This scheme is mainly based on the decoupling of the hopping term of the Hamiltonian. Unlike the BA, this approach succeeds in predicting the SF-MI transitions. A site decoupling mean field theory (MFT) transforms the BHM into a single site effective Hamiltonian and thus is expected to miss out on the intersite correlations. Although the fluctuations are inevitable, one still obtains a qualitatively correct phase diagram at zero temperature for all finite values of interaction parameters. A multisite version of the MFT is introduced, where the hopping among a cluster of sites is treated exactly, while the inter cluster couplings are treated within an MFT to capture the fluctuation in the physical variables[97–99]. A brief description of the single site and multisite mean field theories are presented in the following.

1.3.3.1 Single Site MFT

The method consists of decoupling the kinetic energy operator which can be shown as,

$$b_i^\dagger b_j \quad \rightarrow \quad \langle b_i^\dagger \rangle b_j + b_i^\dagger \langle b_j \rangle - \langle b_i^\dagger \rangle \langle b_j \rangle = \psi_i b_j + \psi_j b_i^\dagger - \psi_i \psi_j \tag{1.38}$$

where $\psi_i = \langle b_i^\dagger \rangle = \langle b_i \rangle$ is the order parameter which for the number conserving case, is real. In the single site mean field techniques, the couplings between the sites are completely replaced by average fields as shown in Fig. 1.5(a). Now the Hamiltonian in Eq. (1.19) can be written as a sum of single site Hamiltonian as,

$$H = \sum_i H_i^{MF}(\psi_i, \phi_i) \tag{1.39}$$

where $\phi_i = \sum_{j=1}^{z} \psi_j$, z being the coordination number of the lattice. H_i^{MF} is hence given by,

$$H_i^{MF}(\psi_i, \phi_i) = \left[\frac{U}{2}\hat{n}_i(\hat{n}_i - 1) - \mu \hat{n}_i\right] - zt\left[\phi_i(b_i + b_i^\dagger) + \psi_i \phi_i\right]. \tag{1.40}$$

For a homogeneous system, the observables are independent of the lattice site and we can set $\phi_i = \psi_i = \psi$. Hence the Hamiltonian becomes site independent and can

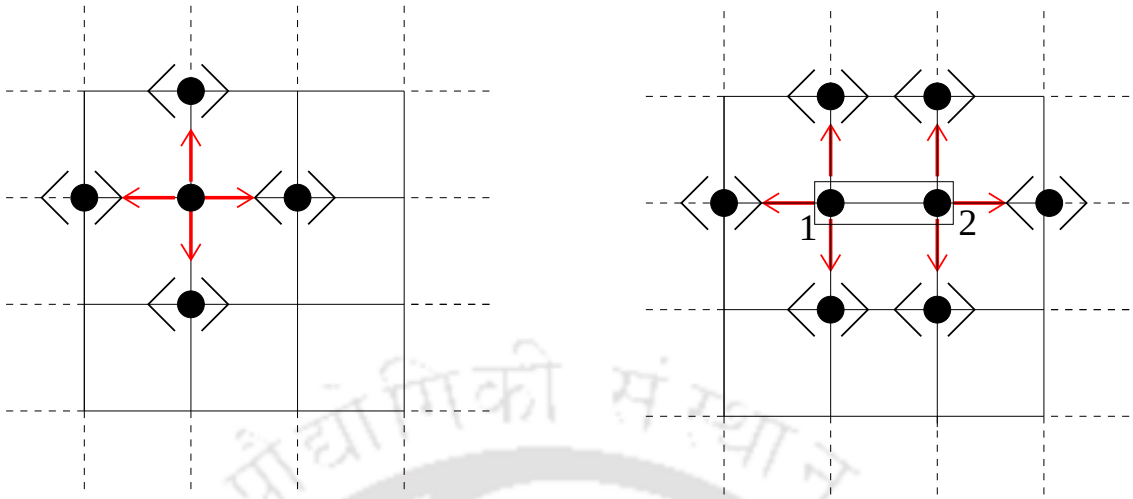

Figure 1.5: The decoupling scheme of a single site in (a) and for a cluster of two site in (b) is presented. The angular brackets is used to indicate average field of the bosonic operators.

be written as,

$$H^{MF} = \left[\frac{U}{2}\hat{n}(\hat{n}-1) - \mu\hat{n}\right] - \psi(b+b^{\dagger}) + \psi^2. \tag{1.41}$$

In the above equation the interaction parameter, U and the chemical potential, μ are scaled by the energy zt. The matrix representation of the above Hamiltonian can be obtained in the occupation number basis, $|n\rangle$ (truncated at some maximum value $n = n_{max}$) by computing the matrix elements as

$$\langle n^{'}|H^{MF}|n\rangle = \left[\psi^2 + \frac{U}{2}n(n-1) - \mu n\right]\delta_{n,n'} - \left[\psi(\sqrt{n+1}\delta_{n+1,n'} + \sqrt{n}\delta_{n-1,n'})\right] \tag{1.42}$$

where the operators $b_i^{\dagger}$ and b are the raising and lowering operators of the quantum harmonic oscillator. Thus,

$$\begin{aligned} b_i^{\dagger}|n\rangle &= \sqrt{n+1}|n+1\rangle \\ b_i|n\rangle &= \sqrt{n}|n-1\rangle. \end{aligned} \tag{1.43}$$

Suppose $n_{max} = 3$, then the order of the matrix becomes 4×4 and the matrix representation of the Hamiltonian is,

$$\begin{bmatrix} \psi^2 & -\psi & 0 & 0 \\ -\psi & \psi^2 - \mu & -\sqrt{2}\psi & 0 \\ 0 & -\sqrt{2}\psi & \psi^2 - 2\mu + U & -\sqrt{3}\psi \\ 0 & 0 & -\sqrt{3}\psi & \psi^2 - 3\mu + 3U \end{bmatrix}.$$

The eigenvalues and eigenstates for a homogeneous system can be found by diagonalizing the above matrix. The order parameter which is to be obtained self consistently as, $\psi = \langle b \rangle (= \langle b^\dagger \rangle$ for a real $\psi)$. In Fig. 1.6, the ground state energy (E_g) variation as function of n_{max} is shown which yields the following. When $n_{max} < 6$, E_g depends on the choice of n_{max}. So to attain a stable ground state, the value of n_{max} should be atleast 6. We have worked mostly $n_{max} = 8$.

For an inhomogeneous system (which can results from disorder, harmonic potential), the order parameter no longer remains site independent. Hence the Hamiltonian at each site will have to be treated individually and since each site is connected to z neighbours, a simultaneous selfconsistent solution of the problem at all sites is necessary.

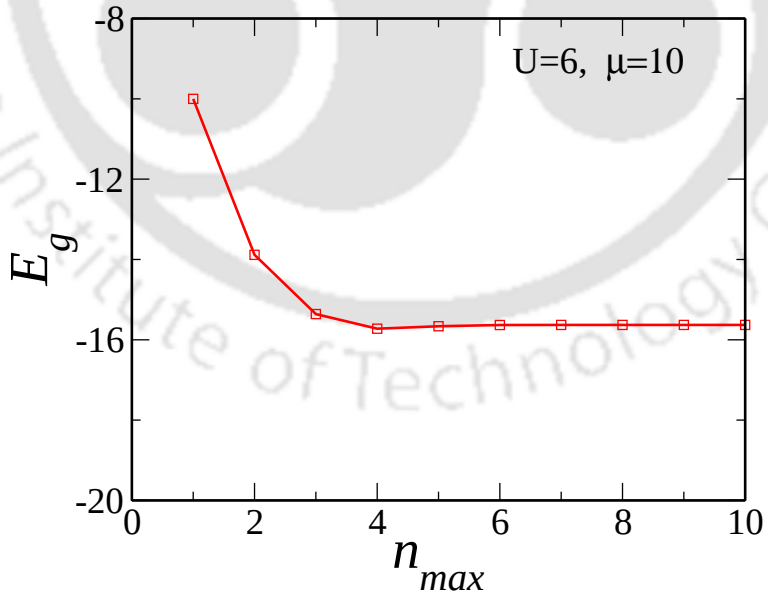

Figure 1.6: The plot shows the variation of ground state energy, E_g as a function of truncated occupation number, n_{max}. For $n_{max} < 6$, E_g depends on n_{max}. But after that values, E_g is independent of the choice of n_{max}.

1.3.3.2 Multisite MFT

In the site decoupled mean field theory, the intersite correlations which allow for fluctuations of various physical quantity are completely neglected. For example, the occupation density in the MI phase of a homogeneous system is precisely an integer, whereas in reality there must be some (albeit small) fluctuations occur in the occupation density[97]. These effects can be captured, at least to some extent, by the multisite MFT (MSMFT). In MSMFT, the hopping among a cluster of sites are treated exactly, while the inter cluster couplings are treated within a MFT[97,99,100]. This approximation has yielded systematic improvement of the results for the MI-SF phase boundary and in particular, the critical values of the phase space parameters are refined as the size of the cluster is increased. This approach is used in many cases such as to study the the MI-SF transition in superlattices[99] and also for the disordered BHM[101]. Here we describe a two site cluster mean field theory by treating two lattice site exactly and taking the average contributions from their neighbours (see Fig. 1.5(b)) in the following manner. In the homogeneous BHM, the hopping term decouples as,

$$H_t^{MF} = -t\sum_{\langle i,j\rangle} b_i^\dagger b_j = -t\left[b_1^\dagger b_2 + b_2^\dagger b_1 + 3\psi(b_1^\dagger + b_1 + b_2^\dagger + b_2 - 2\psi)\right] \tag{1.44}$$

here the subscripts of the bosonic operator denote lattice site indices that are treated exactly. Therefore the MF Hamiltonian becomes,

$$H^{MF} = H_t^{MF} + \frac{U}{2}\big[\hat{n}_1(\hat{n}_1-1) + \hat{n}_2(\hat{n}_2-1)\big] - \mu\big[\hat{n}_1+\hat{n}_2\big]. \tag{1.45}$$

The matrix representation of the above Hamiltonian can be found by computing the matrix element in the occupation number basis. In this case the basis is chosen as $|n_1, n_2\rangle$ truncated at sum maximum occupancies n_{1max} and n_{2max} corresponding to the two sites. If the maximum occupation number for both the sites choose $n_{1max} = n_{2max} = 3$, in this case the dimension of the matrix becomes $4^2 \times 4^2$. The matrix elements of the MF Hamiltonian are calculated as,

$$\begin{aligned}\langle n_1^{'}, n_2^{'}|H^{MF}|n_1, n_2\rangle &= \langle n_1^{'} n_2^{'}|H_t^{MF}|n_1, n_2\rangle \\ &+ \frac{U}{2}\langle n_1^{'}, n_2^{'}|\hat{n}_1(\hat{n}_1-1) + \hat{n}_2(\hat{n}_2-1)|n_1, n_2\rangle \\ &- \mu\langle n_1^{'}, n_2^{'}|\hat{n}_1+\hat{n}_2|n_1, n_2\rangle \end{aligned} \tag{1.46}$$

where each term on the right hand side is calculated as,

$$\begin{aligned}\langle n_1^{'} n_2^{'}|H_t^{MF}|n_1,n_2\rangle &= -t\big[\sqrt{n_1+1}\sqrt{n_2}\delta_{n_1+1,n_1^{'}}\delta_{n_2-1,n_2^{'}} \\ &+ \sqrt{n_1}\sqrt{n_2+1}\delta_{n_1-1,n_1^{'}-1}\delta_{n_2+1,n_2^{'}} \\ &+ 3\psi(\sqrt{n_1+1}\delta_{n_1+1,n_1^{'}}\delta_{n_2,n_2^{'}}+\sqrt{n_1}\delta_{n_1-1},n_1^{'}\delta_{n_2,n_2^{'}} \\ &+ \sqrt{n_2+1}\delta_{n_1,n_1^{'}}\delta_{n_2+1,n_2^{'}}+\sqrt{n_2}\delta_{n_1},n_1^{'}\delta_{n_2-1,n_2^{'}})\big], \quad (1.47)\end{aligned}$$

$$\begin{aligned}\frac{U}{2}\langle n_1^{'},n_2^{'}|\hat{n}_1(\hat{n}_1-1)+\hat{n}_2(\hat{n}_2-1)|n_1,n_2\rangle &= \frac{U}{2}\big[n_1(n_1-1) \\ &+ n_2(n_2-1)\big]\delta_{n_1,n_1^{'}}\delta_{n_2,n_2^{'}} \quad (1.48)\end{aligned}$$

and

$$\mu\langle n_1^{'},n_2^{'}|\hat{n}_1+\hat{n}_2|n_1,n_2\rangle = \mu\big[n_1+n_2\big]\delta_{n_1,n_1^{'}}\delta_{n_2,n_2^{'}}. \quad (1.49)$$

The matrix can subsequently be diagonalized to yield the ground state energy and wavefunction of the system from the lowest eigenvalue and the corresponding eigenvector respectively.

1.3.3.3 Limitations of MFT

It may be noted that the agreement between the MFT and the other more refined techniques is only qualitative in one dimension[102], but it becomes progressively better in two and three dimensions[47,103]. In Ref.[103] the deviation of various techniques, such as the MFT, strong coupling expansions, variational methods and field theoretic methods with that of the quantum Monte Carlo data for the critical parameters are presented in the context of two and three dimensions. It should further be stressed that the MFT results agree with those obtained from other techniques in most parts of the boundary that separates the compressible (SF) and incompressible (MI) phases, however the agreement becomes poor at the tip of the Mott lobes which is the most sensitive region. This can be understood as follows. The fluctuation in the order parameter is ignored by MFT and hence it yields a continuous phase boundary with smooth boundaries separating the SF-MI phases, while more refined methods, such as a field theoretic method and a QMC may miss a real solution at certain discrete values of the chemical potential near the tip lobe.

1.3.4 Strong Coupling Perturbation Technique

In the limit $\frac{U}{t} \to \infty$, the mean field Hamiltonian in Eq. (1.41) can be written as sum of unperturbed Hamiltonian, $H^{(0)}$ and a perturbation term, $H^{'}$ as,

$$H = H^0 + \psi H^{'} \tag{1.50}$$

where

$$H^0 = \left[\frac{U}{2}\hat{n}(\hat{n}-1) - \mu\hat{n} + \psi^2\right]. \tag{1.51}$$

The perturbation term comprises of the boson operators as,

$$H^{'} = -\psi(b + b^{\dagger}). \tag{1.52}$$

The ground state energy corresponding to H^0 in the occupation number basis $|g\rangle$ (g is the occupation number corresponding to ground state) is computed as,

$$E_g^{(0)} = \langle g|H^0|g\rangle. \tag{1.53}$$

The first order correction to the energy due to perturbation term, $H^{'}$ is zero, because it is linear in the bosonic operators. The second order correction to the ground state energy is given by,

$$E_g^{(2)} = \psi^2 \sum_{n \neq g} \frac{|\langle g|H^{'}|n\rangle|^2}{E_g^{(0)} - E_n^{(0)}}. \tag{1.54}$$

Therefore the total energy up to a second order correction is,

$$E = E_g^{(0)} + E_g^{(2)}. \tag{1.55}$$

The minimization of above energy with respect to the SF order parameter, ψ will give the phase boundaries between various incompressible and compressible phases.

1.3.5 Gutzwiller Ansatz

The Gutzwiller method is a variational ansatz that was first introduced to study the fermionic Hubbard model then it has then been applied also in the context of the bosonic model[46,55]. The variational ansatz is that the ground state is written

as a product of independent wavefunctions on every site as,

$$|\Psi_g\rangle = \prod_{i=1}^{N_S} \left[\sum_{n_i=0}^{\infty} f_{n_i}^i |n_i\rangle \right], \tag{1.56}$$

where the coefficients f_n^i are to be optimized in the variational procedure and N_s is the number of lattice sites. In the above choice of the wavefunction, the dimension D of Hilbert space is restricted to

$$D = N_S \times (n_{max+1}), \tag{1.57}$$

where n_{max} is the maximum site occupation number. This quantity (D) increases only linearly with the system size, thus making it possible to study larger systems, as compared to the ones that can be studied by exact diagonalization methods. The drawback is that the Gutzwiller wavefunction ignores the correlations between different sites of the lattice. Using the Gutzwiller ansatz, the different ground state correlation functions can be calculated using,

$$\langle b_i^\dagger b_j \rangle_g = \left(\sum_{n_i=0}^{\infty} f_{n_i+1}^{*i} f_{n_i}^i \sqrt{n_i+1} \right) \left(\sum_{n_j=0}^{\infty} f_{n_j}^{*j} f_{n_j+1}^j \sqrt{n_j+1} \right) \tag{1.58}$$

$$\langle b_i^\dagger b_i \rangle_g = \sum_{n_i=0}^{\infty} |f_{n_i}^i|^2 n_i \tag{1.59}$$

$$\langle b_i^\dagger b_i^\dagger b_i b_i \rangle_g = \sum_{n_i=0}^{\infty} |f_{n_i}^i|^2 n_i(n_i-1) \tag{1.60}$$

$$\langle b_i \rangle_g = \sum_{n_i=0}^{\infty} f_{n_i}^{*i} f_{n_i+1}^i \sqrt{n_i+1}. \tag{1.61}$$

Hence the expectation value of the BHM on with respect to $|\Psi_g\rangle$ is given by,

$$\begin{aligned} \langle H \rangle_g = & - t \sum_{\langle i,j \rangle} \left(\sum_{n_i=0}^{\infty} f_{n_i+1}^{*i} f_{n_i}^i \sqrt{n_i+1} \right) \left(\sum_{n_j=0}^{\infty} f_{n_j}^{*j} f_{n_j+1}^j \sqrt{n_j+1} \right) \\ & + \frac{U}{2} \sum_i \sum_{n_i=0}^{\infty} |f_{n_i}^i|^2 n_i(n_i-1) + \sum_i (\epsilon_i - \mu) \sum_{n_i=0}^{\infty} |f_{n_i}^i|^2 n_i. \end{aligned} \tag{1.62}$$

In the homogeneous case ($\epsilon_i = 0$), the coefficients f_n are independent of the site index. Therefore Eq. (1.62) reduces to

$$\frac{\langle H\rangle_g}{N_s} = \left[-zt\sum_{n=1}^{\infty}\sum_{m=1}^{\infty} f_n^* f_{n-1} f_{m-1}^* f_m \sqrt{nm} + \sum_{n=0}^{\infty} |f_n|^2 \left(\frac{U}{2}n(n-1) - \mu n\right)\right]. \quad (1.63)$$

To describe the ground state of the system, the values of the coefficients f_n are such that it minimizes the expectation value of the Hamiltonian in Eq. (1.63). Once the coefficients, f_n are known, various observables can be computed using Eq. (1.58)-(1.61).

1.3.6 Quantum Monte Carlo Techniques

Numerical simulations based on Monte Carlo techniques have been used extensively to study the BHM. A variational Monte Carlo, particularly in presence of disorder, which can interpolate between the superfluid, Bose glass and the Mott insulating phases by appropriately adjusting the variational state can conveniently be used[104,105]. The variational state uses a Gutzwiller wavefunction supplemented by a density-density Jastrow factor applied to a condensate state where all the bosons macroscopically occupy the lowest momentum state. The disorder is hence modeled by site dependent Jastrow factors that include some additional variational parameters.

In addition, a Greens functions Monte Carlo technique can be used at zero temperature which is capable of providing numerically exact results owing to the absence of the *'sign problem'* which impedes its usage in fermionic systems[106,107] The method starts with a trial wavefunction and decimates the larger energy modes by iterative applications of the imaginary time evolution operator. However still the reliability of the method largely depends on finding accurate variational states describing the true ground state.

We do not elaborate on these elegant numerical methods any further, mainly because we have not used them directly in the thesis, although have compared the results of these with our mean field results, and furthermore there are dedicated reviews on these techniques.

1.4 Outline of the Thesis

Since experimentally, a large number of optical lattice geometry are realizable, an enumeration of the different condensate properties in these geometries becomes necessary. We characterize a condensate of bosons in different lattice geometries. We also want to understand the location and nature of the BG phase in the phase diagram for 'dirty' bosons. As the results on bipartite lattices such as a square or a cubic lattice is well documented, we perform the corresponding study in non-bipartite environment. As an example, we have considered a kagome lattice and investigate the phases therein. Since trapping effects are inevitable in the study of cold bosons, we considered bosons in presence of a harmonic confinement. An inhomogeneous version of the mean field theory is found to be suitable to describe different phases and coexistence of them for a kagome lattice. Also as studies on single component bosons are abundant in literature, and that there are experimental evidences of two component fluids, we consider a three component bosonic mixture. Different possibilities of mixed SF and MI phases and MI phases with fractional occupancies are discussed.

In the following, we present a more elaborate plan of the thesis by including a description of the various problems that have been tackled in the form of chapters of the thesis.

In **Chapter 2**, motivated by the availability of optical lattices with tunable geometries in experiments, we compute different physical properties such as condensate fraction, fluctuations therein, depletion of the condensate density and quasiparticle velocity as a function of the interparticle interaction strength for bosons in various 2D optical potentials that correspond to square, triangular and honeycomb geometries. Our results demonstrate an interplay of these features with that of the coordination number of the lattice. A triangular lattice, which has a coordination number, $z = 6$ show large condensate fraction and fluctuation of the condensate density, along with a low depletion of the ground state occupancy. The other candidates, namely, the square lattice ($z = 4$) and honeycomb lattice ($z = 3$) occupy second and third places respectively with regard to these properties. The quasiparticle velocities for these geometries follow a similar pattern as that of the condensate fraction data. The observations are explained by the behaviour of the low energy quasiparticle density of states. Finally, to make the role of lattice geometry obvious, we have included a discussion on a kagome lattice, a classic example of a non-bipartite lattice, which in spite of having the same coordination number as

that of a square lattice, that is $z = 4$, yields a significantly low condensate fraction than that of the square lattice for all values of the interacting strengths, thereby underscoring the interplay of lattice geometry and condensate properties.

In **Chapter 3**, we consider a case of a bounded random onsite disorder potential in a BHM. Such a disorder is known to yield a glassy phase, called as the BG phase, that interrupts a direct transition from a SF to MI phases. Within a site decoupled mean field theory of the BHM, an SF (MI) phases are characterized by nonzero (zero) values of order parameter, and a BG phase by a zero order parameter, yet nonzero compressibility. The accurate distinction between various phases is done via computing a number of relevant physical quantities such as, a ratio of the sites containing integer density of the bosons to that of the total number of sites, compressibility, or a close variant of it and the entropy etc. Quite intriguingly, assuming the appearance of a spanning cluster of sites with integer occupancies to signal the onset of the BG phase, we find that the percolation threshold is very similar to that of random site percolation model in two dimensions. This similarity between two completely different systems is thought to be accidental, but may open up more studies in the future to critically examine the issue. Further with the data obtained from our analysis, we have been able to obtain a complete phase diagram defined by the local interparticle interaction parameter (U) and the chemical potential (μ) averaged over several random configurations at different disorder values.

Chapter 4 deals with the phase diagram of interacting bosons in a tripartite lattice in two dimensions with a long range density density interaction. An analytic computation of the phase diagram is done via a second order strong coupling perturbation theory on the extended Bose Hubbard model, which is hence supplemented by numerical mean field calculations. Interesting results emerge in the form of exotic density ordered phases with one-third, two-third and integer filling of bosons per trimer. These are often referred to as charge density wave of bosonic systems. Further a supersolid phase, characterized by finite and distinct order parameters and densities. The pattern repeats as the chemical potential is increased. Regions of supersolid and superfluid phases are noted in the numerical study of the mean field model where the phase diagram shows a transition from compressible to insulating phases.

In **Chapter 5**, expecting that studies of the phase diagram on non-bipartite lattices can yield exciting features, and motivated by the possibility of obtaining a trimerized optical lattice, such as a kagome lattice experimentally by employing counter propagating laser beams, we investigate the phase diagram of correlated

bosons in a kagome lattice. Then we also include a harmonic trap in the present context as a confining potential usually accompanies the discussion on the optical lattices. It is emphasized that such trapping effects (together with the density exchange term) lead to the necessity of considering the detailed geometry of the lattice, and thus the measured quantities appeal to a particular geometry, kagome lattice being the case here. The phase diagram thus obtained yields coexistence of different compressible and incompressible phases. There are distinct signatures of superfluid, insulating, density ordered and supersolid phases as one moves towards the edge of the lattice starting from the center of the confining potential. A comparison of the results obtained for the order parameters corresponding to other geometries, such as square and honeycomb lattices are presented. Relevant to the *"time of flight"* experiments, the order parameters have been computed in the momentum space, which corroborate the coexistence of different phases for a kagome lattice.

In **Chapter 6**, a three component bosonic mixture is considered as a representative of the multi-component mixtures that is capable of demonstrating a significantly rich phase diagram in comparison to a two component mixture or a single component fluid. With the experimental studies on the multi-component mixtures gaining momentum, and comparatively little theoretical efforts, we consider an interacting three component Bose gas on a lattice and, via a strong coupling expansion of the Bose Hubbard model, and study a variety of situations, such as the inter and intraspecies interactions being same and different, attractive and repulsive etc. Scenario of rich phase diagrams emerges where one specie of atoms can be in the MI phase, while the other two may be in SF phases. Such a mixed phase diagram with different species coexisting in different phases is an exciting one: a possibility that can be explored in selective *"time of flight"* experiments. Numerical solution of the mean field equations has further demonstrated the occurrence of insulating phases with fractional filling of each specie of atoms.

In **Chapter 7**, we conclude with a highlight of the results obtained in the thesis.

Chapter 2

Lattice Potential Effects on the Condensate Properties of Bosons: a Bogoliubov Approach

2.1 Introduction

Before we survey the phase transition scenario in a quantum fluid of interacting bosons, it is a good idea to look at the effects of the underlying periodic structure of the optical lattice on the condensate properties of the system. As emphasized earlier in the previous chapter, optical lattices with a variety of lattice geometries are experimentally realizable in different dimensions by manipulating the configuration of the assembly of laser beams that are used for this purpose. Motivated by the early works of Grynberg *et al.*[108] on interesting profiles of the optical potential with three coplanar laser beams, each of which makes an angle $2\pi/3$ with each other, and the recent realization of graphene in two dimension (2D)[109–111], there has been growing interest in studying interacting bosons on triangular[112–114] and honeycomb lattices in 2D[115–118]. While most of these studies have predominantly concentrated on understanding the quantum phase transitions in different optical lattice geometries, little effort is devoted so far to explore the interplay of the physical properties with the underlying symmetry of the optical lattices in details.

The present work will surely gain importance if experiments are designed to test the interplay of the condensate data and the parameter of the optical lattice. Usually information about the condensate density of a BEC is obtained via the time of flight measurements which estimate the fraction of atoms in different momentum components of the ground state[119,120]. The technique ascertains the phase coher-

ence of the condensate atoms across the optical lattice, where upon switching off all the trapping potentials, the atomic cloud is allowed to expand ballistically and hence "*imaged*". Phase coherence is implied by a sharp peak in the spectrum while a broad pattern denotes absence of long range order.

Of particular interest to us in the present context are two dimensional planar geometries such as square, triangular, honeycomb and kagome lattices[16,114,121–123]. We organize this chapter in the following way. The discussion is split into two parts. In the next section we include details on the optical potentials which yield different lattice geometries corresponding to different orientation of the counter-propagating laser beams. This material covered in this section should complement and serve as a motivation for the discussion carried out in section 2.3 that deals with computing the condensate fraction of the interacting bosons using a Bogoliubov approximation on a Bose Hubbard model. Our studies are further substantiated by calculating the relative fluctuations and depletion of the condensate density for different optical lattices geometries. The results are shown to have relevance with the coordination number and symmetry of the underlying lattice. Finally in section 2.4, to illustrate the importance of the underlying lattice geometry, we have presented the condensate fraction data for a kagome lattice and compared with the corresponding data for a square lattice. The comparison is meaningful as both this have the same coordination number. We end with a brief discussion of our results in section 2.5.

2.2 Optical Lattice Potentials

Here we illustrate how various lattice geometries can be achieved in 2D by using a three laser beam configuration[16,124]. It may be noted that a significant part of the thesis deals with different lattice geometries, and mostly non-bipartite lattices, making the following discussion very relevant for us. We start with this result and field configurations due to three linearly polarized beams in the $x-y$ plane making angle θ_j $(j = 1, 2, 3)$, with x- axis as shown in Fig. 2.1. The total electric field in this case can be written as,

$$\mathbf{E}(\mathbf{r}, t) = \sum_{j=1,2,3} \mathbf{E}_j(\mathbf{r}, t) \tag{2.1}$$

where $\mathbf{E}_j$ is the electric field vector due to the three intersecting linearly polarized beams (polarization being orthogonal to $x-y$ plane), all having same frequency, ω_0

and are given by,

$$\mathbf{E}_j = E_{0j}\ e^{i(\mathbf{k}_j.\mathbf{r})}e^{-i\omega_0 t}\ \hat{\mathbf{z}} \tag{2.2}$$

where $\mathbf{k}_j$'s are parameterized in terms of the wavevector, k_0 ($\omega_0 = ck_0$, c being the

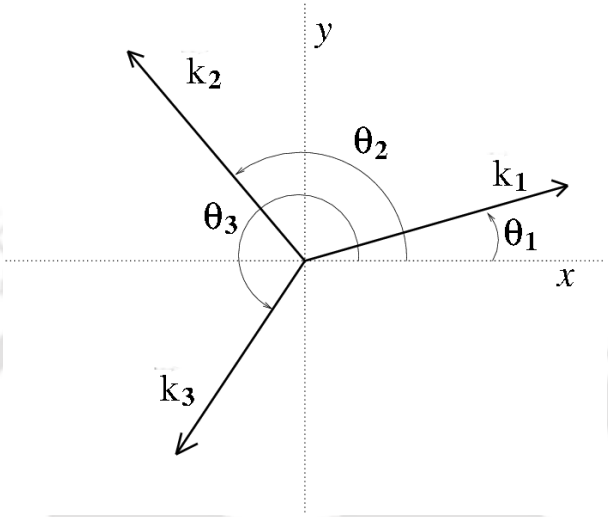

Figure 2.1: The three wavevectors corresponding to three laser beams configurations are shown. The wavevectors $\mathbf{k}_1, \mathbf{k}_2$ and $\mathbf{k}_3$ make angles θ_1, θ_2 and θ_3 with the x-axis. The θ values in table 2.1 are shown corresponding to square, triangular and honeycomb geometries.

speed of light) of the incoming beam. The optical potential, which is proportional to the resultant intensity is given by,

$$\begin{aligned} V_{opt}(\mathbf{r}) &= |\mathbf{E}(\mathbf{r},t)|^2 \\ &= V_0[3 + 2\cos(\mathbf{p}_1.\mathbf{r}) + 2\cos(\mathbf{p}_2.\mathbf{r}) + 2\cos[(\mathbf{p}_1+\mathbf{p}_2).\mathbf{r}]] \end{aligned} \tag{2.3}$$

where $\mathbf{p}_1 = \mathbf{k}_3 - \mathbf{k}_1$, $\mathbf{p}_2 = \mathbf{k}_1 - \mathbf{k}_2$ and V_0 is a coefficient that depends on the detuning parameter (see Eq. (1.7) and the subsequent discussion).

At this stage, let us demonstrate how the optical potential in Eq. (2.3) can be used to generate different kind of periodic structures by appropriately choosing the wavevectors, $\mathbf{k}_j$ of the incoming beams (see table 2.1). We shall consider square, triangular and honeycomb geometries. The 2D wavevectors are written as,

$$\mathbf{k}_j = k_0(\cos\theta_j\ \hat{\mathbf{x}} + \sin\theta_j\ \hat{\mathbf{y}}). \tag{2.4}$$

The vectors $\mathbf{p}_1$ and $\mathbf{p}_2$ calculated from the above choices for $\mathbf{k}_1$, $\mathbf{k}_2$ and $\mathbf{k}_3$ represent the reciprocal lattice vectors for the corresponding geometries. For example, for a 2D triangular lattice, the reciprocal lattice vectors are $\sqrt{3}k_0(\frac{\sqrt{3}}{2}\hat{\mathbf{x}} - \frac{1}{2}\hat{\mathbf{y}})$ and

Geometry	θ_1	θ_2	θ_3	sign of V_0	detuning
Square	0°	90°	180°	negative	red-detuning
Triangular	0°	120°	240°	negative	red-detuning
Honeycomb	0°	120°	240°	positive	blue-detuning

Table 2.1: The values of the parameters, θ_j and V_0 needed to create different lattice geometries are shown.

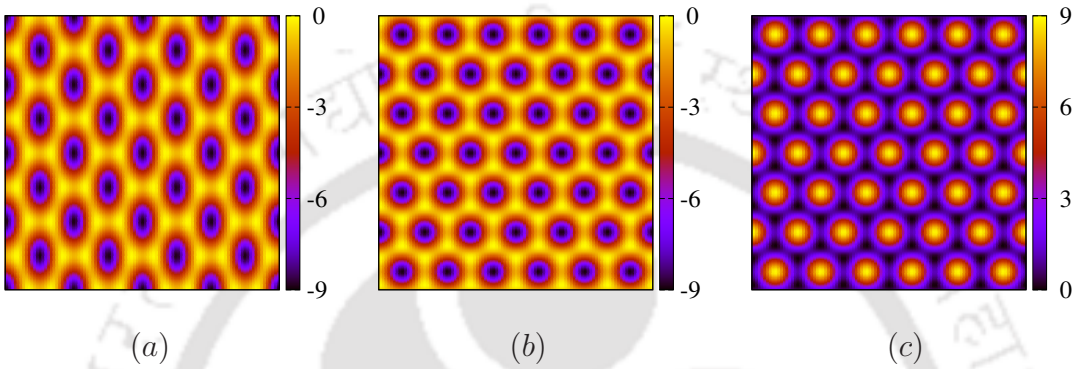

Figure 2.2: The surface plots of the optical lattice potentials given by Eq. (2.3) for the three beam laser configuration are shown. Three kind of geometries, (a) square lattice, (b) triangular lattice and (c) honeycomb lattice are achieved by choosing the parameters, θ_j and V_0 as presented in table 2.1. The horizontal and vertical axes are presented in units of $\frac{1}{\lambda}$, λ being the wavelength of the laser beam.

$\sqrt{3}k_0(-\frac{\sqrt{3}}{2}\hat{\mathbf{x}} - \frac{1}{2}\hat{\mathbf{y}})$, which are precisely $\mathbf{p}_1$ and $\mathbf{p}_2$ for the choices of $\mathbf{k}_1$, $\mathbf{k}_2$ and $\mathbf{k}_3$ as given in table 2.1. The surface plots of the optical lattice potentials for different θ values and signs of V_0 are presented in the table are shown in Fig. 2.2.

2.3 Model, Formalism and Calculation of the Physical Properties

To investigate the superfluid properties of interacting bosons on a 2D lattice, we consider a Bose Hubbard Hamiltonian given by Eq. (1.19). For convenience we rewrite the same here,

$$H = -t\sum_{\langle ij\rangle}(a_i^\dagger a_j + h.c.) + \frac{U}{2}\sum_i \hat{n}_i(\hat{n}_i - 1) - \mu\sum_i \hat{n}_i \tag{2.5}$$

with symbols having usual significance. Transforming Eq. (2.5) in the reciprocal space and hence applying Bogoliubov approximation, by following the approach of Ref.[71] that amounts to replacing the creation and annihilation operators in the

following fashion,

$$a_{\mathbf{k}} \rightarrow \sqrt{N_0}\ \delta_{\mathbf{k},\mathbf{0}} + a_{\mathbf{k}} \tag{2.6}$$

where N_0 is the number of atoms in the $\mathbf{k} = 0$ state, usually referred to as the condensate number. The above substitution up to second order in bosonic operators yields,

$$H = H^{(0)} + H^{(1)} + H^{(2)} \tag{2.7}$$

the superscripts denote the order of the bosonic operators retained in the terms. The zeroth order term is given by,

$$H^{(0)} = (\bar{\epsilon}_0 - \mu)N_0 + \frac{1}{2}\frac{U}{N_s}N_0^2 \tag{2.8}$$

where $\bar{\epsilon}_{\mathbf{k}} = -t\sum_{j=1}^{z}\cos(k_j a)$ is the single particle dispersion, z being the number of nearest neighbours. The second term in Eq. (2.7) containing the first order in bosonic operators is,

$$H^{(1)} = (\bar{\epsilon}_0 - \mu + \frac{U}{N_s}N_0)\sqrt{N_0}(a_0 + a_0^{\dagger}) \tag{2.9}$$

and the last term, second order in bosonic operators is,

$$H^{(2)} = \sum_{\mathbf{k}}(\bar{\epsilon}_{\mathbf{k}} - \mu)a_{\mathbf{k}}^{\dagger}a_{\mathbf{k}} + \frac{1}{2}\frac{U}{N_s}N_0\sum_{\mathbf{k}}(a_{\mathbf{k}}a_{-\mathbf{k}} + 4a_{\mathbf{k}}^{\dagger}a_{\mathbf{k}} + a_{-\mathbf{k}}^{\dagger}a_{\mathbf{k}}^{\dagger}) \tag{2.10}$$

here N_s denotes the number of lattice sites in the system. The Bogoliubov approximation implies putting the coefficient of the linear term (Eq. (2.9)) zero, which yields,

$$\mu = \bar{\epsilon}_0 + Un_0 \tag{2.11}$$

Thus including the zeroth and the second order term, the effective Hamiltonian is given by,

$$H^{eff} = -\frac{1}{2}Un_0N_0 + \sum_{\mathbf{k}}(\epsilon_{\mathbf{k}} + Un_0)a_{\mathbf{k}}^{\dagger}a_{\mathbf{k}} + \frac{1}{2}Un_0\sum_{\mathbf{k}}(a_{\mathbf{k}}a_{-\mathbf{k}} + a_{-\mathbf{k}}^{\dagger}a_{\mathbf{k}}^{\dagger}) \tag{2.12}$$

where $\epsilon_k = zt + \bar{\epsilon}_k$. To diagonalize the above effective Hamiltonian in Eq. (2.12), we consider a Bogoliubov transformation given by,

$$\begin{aligned} b_{\mathbf{k}} &= u_{\mathbf{k}}a_{\mathbf{k}} + v_{\mathbf{k}}a_{-\mathbf{k}}^{\dagger} \\ \text{with} \qquad & |u_{\mathbf{k}}|^2 - |v_{\mathbf{k}}|^2 = 1 \end{aligned} \tag{2.13}$$

Lattice	Coordination number, z	Nearest neighbor positions	Single particle dispersion, $\bar{\epsilon}_{\mathbf{k}}$
Square	4	$(\pm 1, 0)$ and $(0, \pm 1)$	$-2t[\cos(k_x) + \cos(k_y)]$
Triangular	6	$(\pm 1/2, \pm\sqrt{3}/2)$ and $(\pm 1, 0)$	$-2t[\cos(k_x) + 2\cos(k_x/2)\cos(\sqrt{3}k_y/2)]$
Honeycomb	3	$(0, 1/\sqrt{3})$, $(1/2, -1/2\sqrt{3})$ and $(-1/2, -1/2\sqrt{3})$	$\pm t[1 + 4\cos^2(k_x/2) + 4\cos(k_x/2)\cos(\sqrt{3}k_y/2)]^{\frac{1}{2}}$

Table 2.2: The table contains the coordination number z, position of the nearest neighbours and single particle dispersion $\bar{\epsilon}_{\mathbf{k}}$ for three type of lattices[125] which are obtained by diagonalizing the noninteracting Hamiltonian, that is the first term in Eq. (2.5).

where $b_{\mathbf{k}}$ and $b^{\dagger}_{\mathbf{k}}$ satisfy the usual bosonic commutation relations, $[b_{\mathbf{k}}, b^{\dagger}_{\mathbf{k}}] = \delta_{\mathbf{k}\mathbf{k}'}$. The diagonal Hamiltonian (same as Eq. (1.33)) takes the following form ($\hbar = 1$ is assumed),

$$H^{eff} = -\frac{1}{2}Un_0N_0 + \frac{1}{2}\sum_{\mathbf{k}}[\omega_{\mathbf{k}} - (\epsilon_{\mathbf{k}} + Un_0)] + \sum_{\mathbf{k}}\omega_{\mathbf{k}}b^{\dagger}_{\mathbf{k}}b_{\mathbf{k}} \tag{2.14}$$

with the values of the coefficients $u_{\mathbf{k}}$ and $v_{\mathbf{k}}$ given by,

$$|v_{\mathbf{k}}|^2 = |u_{\mathbf{k}}|^2 - 1 = \frac{1}{2}\left[\frac{\epsilon_{\mathbf{k}} + Un_0}{\omega_{\mathbf{k}}} - 1\right] \tag{2.15}$$

and

$$\omega_{\mathbf{k}} = \sqrt{\epsilon^2_{\mathbf{k}} + 2Un_0\epsilon_{\mathbf{k}}} \tag{2.16}$$

refers to the the quasiparticle dispersion (these are called as Bogoliubov quasiparticles).

To obtain the total density, n of bosonic atoms, we note that n consists of two parts– (i) the condensate density, n_0 and (ii) the excited state occupancy. At zero temperature, the condensate density is related to the total density in the following manner,

$$n = n_0 + \frac{1}{N_s}\sum_{\mathbf{k}\neq 0}\left(\frac{\epsilon_{\mathbf{k}} + Un_0}{2\ \omega_{\mathbf{k}}} - \frac{1}{2}\right). \tag{2.17}$$

We compute this equation numerically to solve for n_0 corresponding to a given n by using a bisection algorithm for different lattice geometries such as square, triangular and honeycomb by appropriately substituting for the single particle dispersions, $\bar{\epsilon}_{\mathbf{k}}$

as given in table 2.2. The **k**-sum is performed over a grid of 100×100 k-points.

The result for the condensate fraction, n_0/n for a given value of $n = 1$ is plotted in Fig. 2.3 for square, triangular and honeycomb lattices as a function of the interaction, U. The plots demonstrate that the condensate fraction decreases as U increases, albeit remaining finite at very large U (twice the band width is usually taken as a large value for U). The results can initially be understood as in the following. The second term in Eq. (2.17) increases with the increase in U, thereby implying an increase in the excited state occupancy. These results are elaborated later. The absence of onset of an insulating phase is an artifact of the approximation, that is the Bogoliubov approximation, which is known to have the deficiency of accessing the phase transition from a superfluid to a Mott insulating phase.

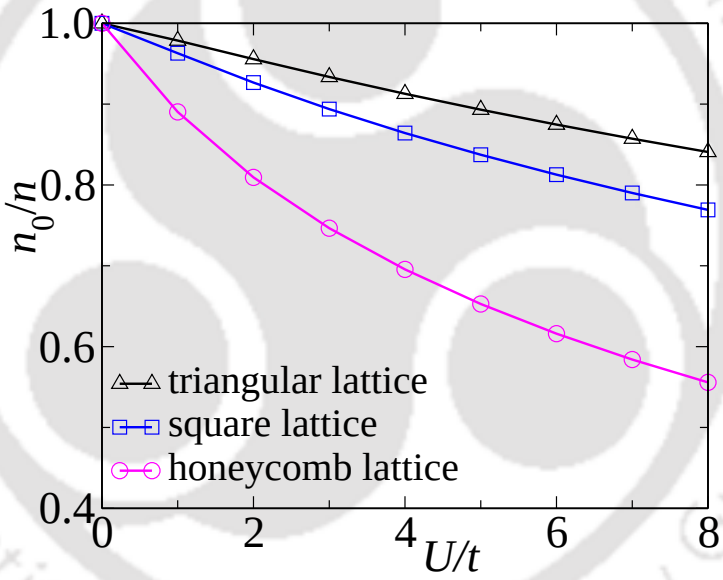

Figure 2.3: The condensate fraction n_0/n is plotted as a function of U for square, triangular and honeycomb lattices. At all values of U, n_0/n is the largest for the triangular lattice. The total density is $n = 1.0$ and remains same for all the plots.

The point which is worthy to note here is that the condensate fraction depends on the number of nearest neighbors, that is coordination number, z of the lattice. For a given U, n_0/n is largest for the triangular lattice ($z = 6$) and lowest for honeycomb lattice ($z = 3$), with it being intermediate between these two for the square lattice ($z = 4$). Same qualitative results are also obtained for other values of the total density, n as shown in Fig. 2.4, where $n = 2$ and $n = 4$ are used. Hence the rest of the results presented in this work correspond to $n = 1$.

The condensate density fluctuation[126], a measurable property for a condensate

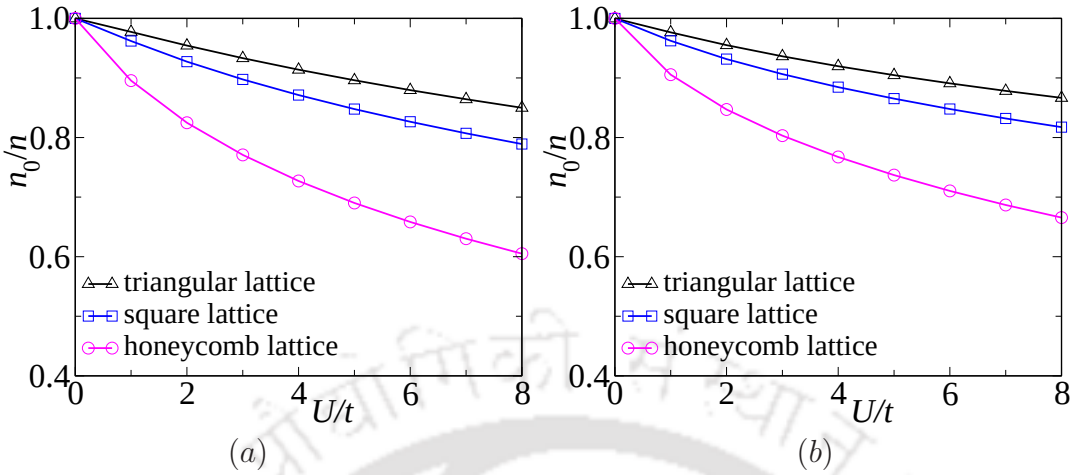

Figure 2.4: The condensate fraction n_0/n is plotted as a function of U for square, triangular and honeycomb lattices for $n = 2$ in (a) and $n = 4$ in (b). The behaviour of n_0/n as a function of U remains same as it is in Fig. 2.3 ($n = 1$). U is presented in units of hopping energy, t and is true for all subsequent plots.

can be obtained as,

$$\begin{aligned} \delta n_0 &= \sqrt{\langle \hat{n}_0^2 \rangle - \langle \hat{n}_0 \rangle^2} \\ &= \sqrt{\frac{n_0}{N} \sum_{\mathbf{k}} |u_{\mathbf{k}} - v_{\mathbf{k}}|^2} \end{aligned} \tag{2.18}$$

where $u_{\mathbf{k}}$ and $v_{\mathbf{k}}$ are defined in Eq. (2.13) and N denote the number of k-points. A sketch of derivation of the above formula is given in Appendix A.

The depletion of the condensate density that how the excited states get populated will yield a quantitative estimate of the loss of atoms in the ground states and is given by[126],

$$d = \frac{1}{N} \sum_{\mathbf{k}} v_{\mathbf{k}}^2 \tag{2.19}$$

δn_0 and d are calculated for the various lattice geometries as a function of U. The fluctuation in the condensate density tracks the condensate fraction data as a large density of the bosons in the $\mathbf{k} = 0$ state imply large fluctuations. At a given U, say $U = 4$ (in units of hopping, t) the normalized fluctuation in the number density of atoms, $\delta n_0/n$ for the triangular lattice is about 0.75, while it is only about 0.5 for the honeycomb lattice, with the square lattice acquiring an intermediate value. The nature of the condensate density depletion is just the opposite, that is the depletion is maximum for the honeycomb lattice followed by square and triangular lattices respectively. Since a smaller depletion of the number of atoms in the ground

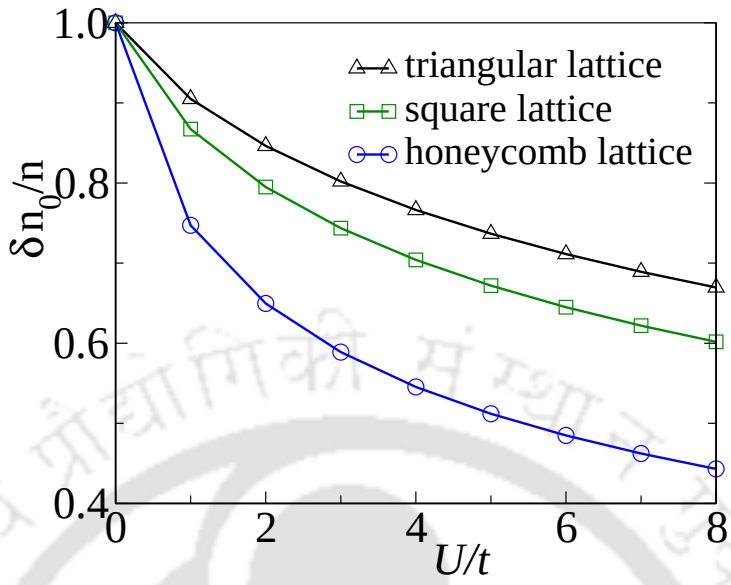

Figure 2.5: The condensate density fluctuations, $\delta n_0/n$ (defined in text) are shown as a function of U for square, triangular and honeycomb lattices. The fluctuation is largest for the triangular lattice. For all cases we have taken total density, $n = 1.0$.

state implies a robust condensate, Fig. 2.6 supports the condensate fraction data presented in Fig. 2.3.

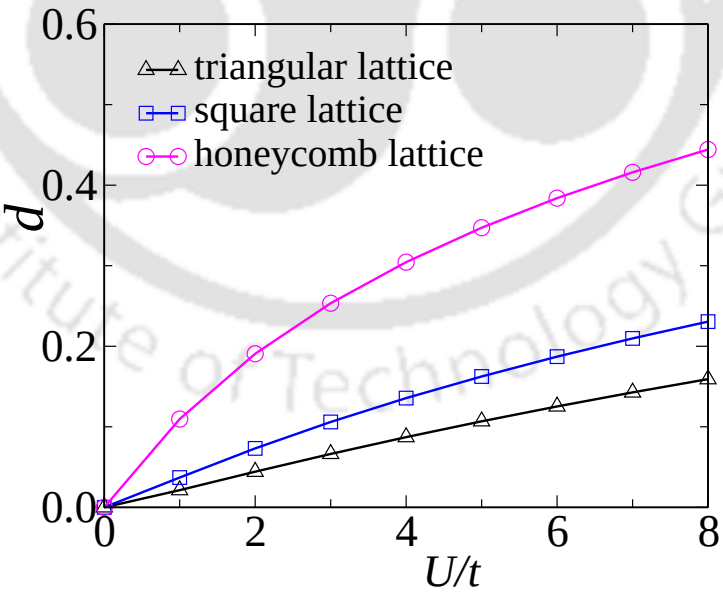

Figure 2.6: The depletion of the condensate densities, d (defined in text) as a function of interaction U are shown for different lattices. The triangular lattice registers a lowest depletion, while it is the highest for the honeycomb lattice.

We explain the results obtained above in the following discussion. In the long-

Lattice	v_{qp}
Square	$\sqrt{2Un_0t}$
Triangular	$\sqrt{3Un_0t}$
Honeycomb	$\sqrt{\frac{Un_0t}{2}}$

Table 2.3: The quasiparticle velocity, v_{qp} for different lattices. It can be seen that in units of $\sqrt{Un_0t}$, the ratio of the velocities is $\sqrt{3} : \sqrt{2} : \sqrt{1/2}$ for triangular, square and honeycomb lattices respectively.

wavelength limit ($k \to 0$), the quasiparticle velocity is given by,

$$v_{qp} = \omega_k/k \tag{2.20}$$

v_{qp} is hence obtained for three kind of geometries and are presented in table 2.3. As can be noted that v_{qp} is the largest for the triangular lattice and is greater than the corresponding value for the honeycomb lattice by a factor of 2.5. This has the following implication. The contribution from the second term in Eq. (2.17) is smaller (due to a larger denominator of the first term inside the bracket). Now for a given (total) density, n of atoms, this will lead to an enhanced n_0.

Further we present a plot of the quasiparticle density of states (DOS) defined by,

$$\rho(\omega) = \frac{1}{N}\sum_{\mathbf{k}} \delta(\omega - \omega_{\mathbf{k}}) \tag{2.21}$$

where N is the number of k-points and $\omega_{\mathbf{k}}$ is the quasiparticle dispersion given in Eq. (2.16). To compute Eq. (2.21), a Lorentzian form with an width of the order of level spacing (between successive entries in the energy spectrum) such as the following

$$\rho(\omega) = \lim_{\eta\to 0}\sum_{\mathbf{k}} \frac{\eta}{(\omega - \omega_{\mathbf{k}})^2 + \eta^2} \tag{2.22}$$

is used. Fig. 2.7 shows a large DOS at low energies for the honeycomb lattice, while for the square lattice it is small and even smaller for the triangular lattice. The implication of this data on our results can be explained as below. The chances that the low lying excited states get occupied easily is greatest for the honeycomb lattice and lowest for the triangular lattice. Now since occupancy of the low lying excited states affects the density of the condensate atoms, we get a support for the trend of the condensate fraction data presented in Fig. 2.3.

Here we make an attempt to put things in perspective by connecting the results

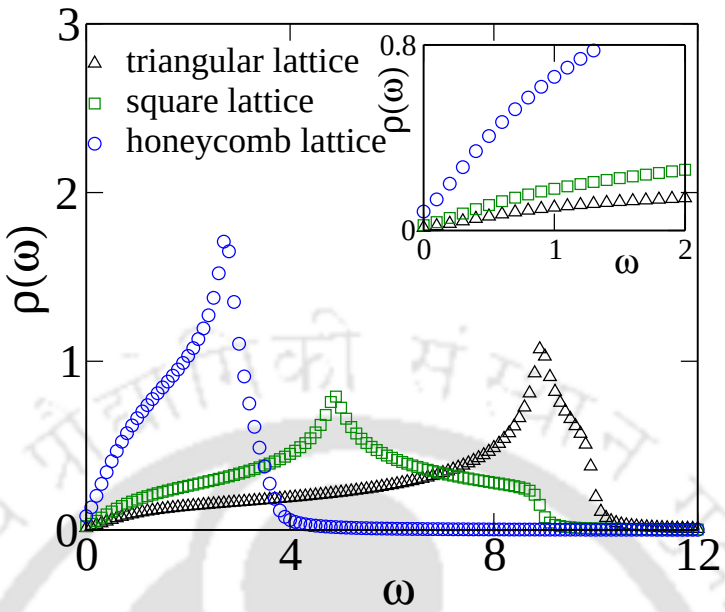

Figure 2.7: The quasiparticle density of states, $\rho(\omega)$, for square, triangular and honeycomb lattices for $U = 1$ (in units of t). The low energy DOS for the triangular lattice is much lesser compared to that of the honeycomb or square lattices.

on the physical properties obtained in section 2.3 to the discussion on optical potentials contained in section 2.2. Fig. 2.8 shows the form of the optical potential drawn along one particular direction in the lattice. The $x-$axes is plotted in terms of a dimensionless quantity, x ($x = \mathbf{k}.\mathbf{r}$), where $\mathbf{r}$ for the different lattice geometries are defined in the figure caption of Fig. 2.8 and the y- axes are plotted in units of V_0. Notice that the $y-$axis has negative values for triangular and square lattices (red detuned), while it is positive (blue detuned) for the honeycomb lattice. With $k = \frac{2\pi}{\lambda}$, λ being wavelength of the laser beam used, the distance between the nodes is the largest for the triangular lattice, followed respectively by square and honeycomb lattices. As the optical lattice is a result of the formation of a standing wave pattern due to counter propagating laser beams, we can take $\lambda \simeq 2a$, a being the lattice constant. It is obvious that the lattice constants for different lattice geometries will follow,

$$a_{honeycomb} > a_{square} > a_{triangular}. \tag{2.23}$$

The lattice constant, a being the distance between the wells in the optical lattice, will determine the tunneling rate t between the lattice sites[6], where a large lattice constant would imply a reduced tunneling. Since the condensate fraction depends on the effective interaction parameter $U^{'} = U/zt$, a lower tunneling rate, t (along with a low coordination number) implies a larger $U^{'}$, thereby yielding a low condensate

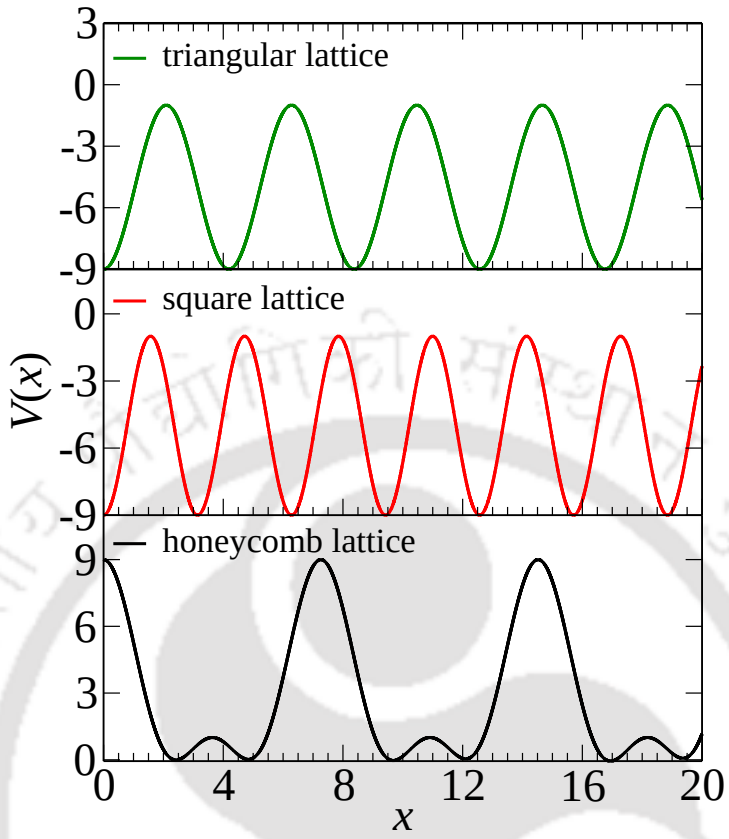

Figure 2.8: 1D cut of the 2D optical potential is plotted as a function of the dimensionless parameter $x = \mathbf{k}.\mathbf{r}$ for different lattice geometries. Here $\mathbf{r}$ is taken along the diagonal, $x-$axis and $y-$axis for square, triangular and honeycomb lattices respectively.

density for a honeycomb lattice than that of a triangular lattice.

To emphasize that the condensate data do not depend solely upon the coordination number and that the underlying lattice geometry plays an important role, we present a brief comparison between square and kagome lattices in the next section. Since both have four neighbours (though kagome has two neighbours each of two different kinds), any difference in the condensate fraction data is likely to highlight the role of lattice geometry in the present context.

2.4 Kagome Lattice

To resolve whether the condensate properties solely depend upon the number of neighbour present, or answer a more direct question, what effect does the underlying lattice geometry has on the condensate state, we consider a kagome lattice geometry which is a well known example for a non bipartite lattice and has the same coordination number as that of square lattice that is $z = 4$.

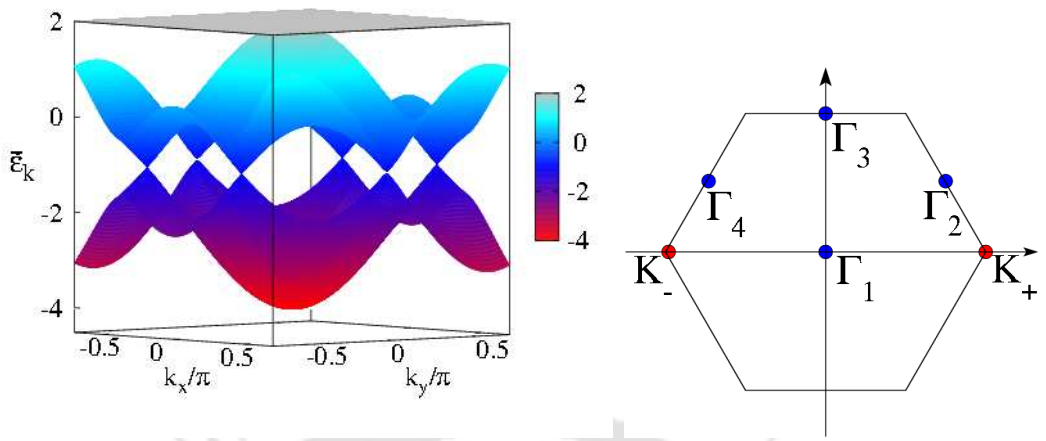

Figure 2.9: The plot shows the three bands of the tight binding dispersion in (a) of a kagome lattice in the first Brillouin zone as shown in (b). There is a flat band at 2 (in units of the hopping energy) with the other two being dispersive as given in Eq. (2.24) which touch each other at six points.

The tight binding dispersion, $\bar{\epsilon}_k$ for the kagome lattice can be obtained by solving the noninteracting ground state Hamiltonian H_0, in a three sublattice basis as given below[127],

$$H_0 = -2t \begin{bmatrix} 0 & \cos(\mathbf{k}.\mathbf{c}_1) & \cos(\mathbf{k}.\mathbf{c}_2) \\ \cos(\mathbf{k}.\mathbf{c}_1) & 0 & \cos(\mathbf{k}.\mathbf{c}_3) \\ \cos(\mathbf{k}.\mathbf{c}_2) & \cos(\mathbf{k}.\mathbf{c}_3) & 0 \end{bmatrix} = -2t \begin{bmatrix} 0 & A & B \\ A & 0 & C \\ B & C & 0 \end{bmatrix}$$

where $A = \cos(\mathbf{k}.\mathbf{c}_1)$, $B = \cos(\mathbf{k}.\mathbf{c}_2)$ and $C = \cos(\mathbf{k}.\mathbf{c}_3)$. Thus the three energy levels are given by, $\bar{\epsilon}^1_{\mathbf{k}} = 2t$, and

$$\bar{\epsilon}^{2,3}_{\mathbf{k}} = t\big[-1 \pm \sqrt{4(\cos^2(\mathbf{k}.\mathbf{c}_1) + \cos^2(\mathbf{k}.\mathbf{c}_2) + \cos^2(\mathbf{k}.\mathbf{c}_3)) - 3}\big]. \tag{2.24}$$

Here $\mathbf{c}_1 = (1, 0)$, $\mathbf{c}_2 = (\frac{1}{2}, -\frac{\sqrt{3}}{2})$, and $\mathbf{c}_3 = \mathbf{c}_2 - \mathbf{c}_1$. In Fig. 2.9, we plot the above three dispersions for the kagome lattice in the first Brillouin zone in absence of interaction.

To make our discussion complete we refer to the *'superlattice'* technique of using a three beam geometry that generates an optical kagome lattice[121,122]. The optical

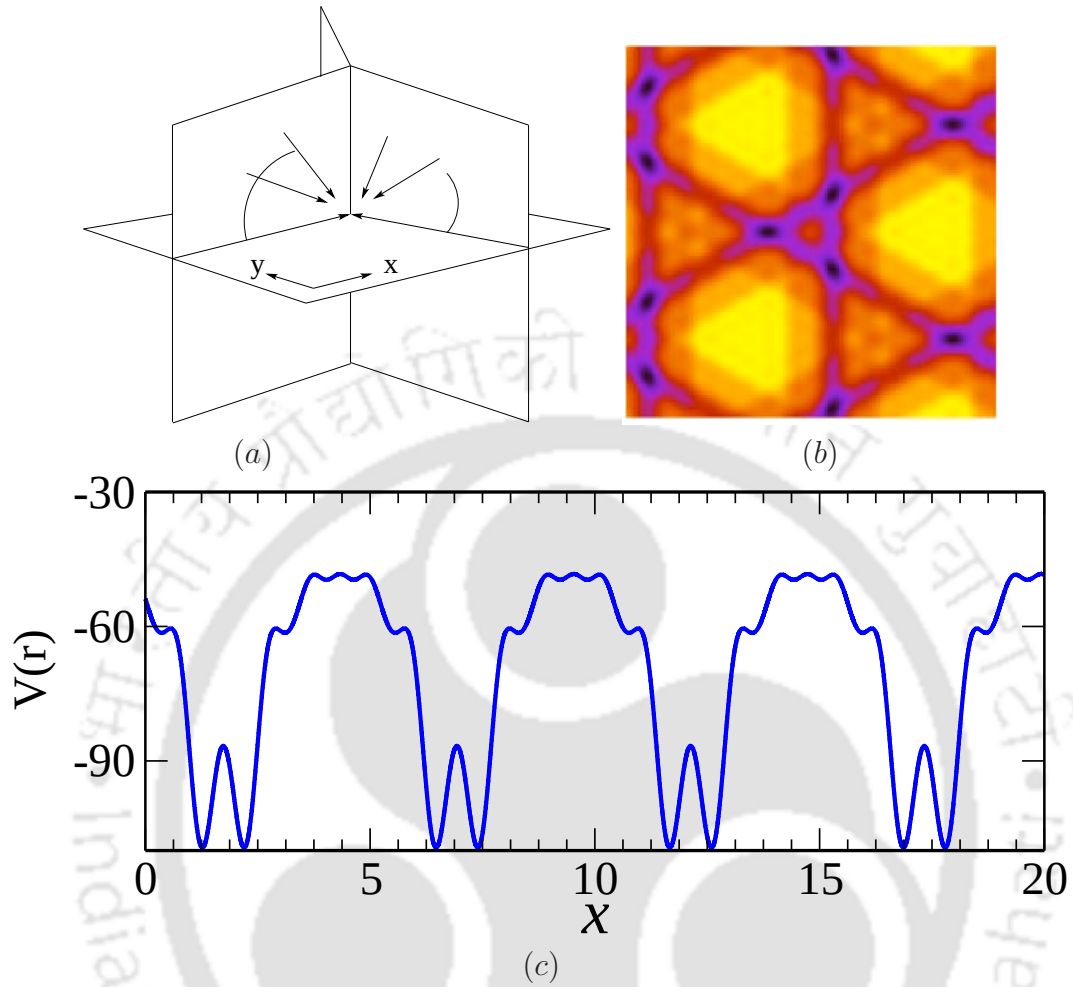

Figure 2.10: Figure from Ref.[121] of the proposed experimental setup for generating kagome lattice potential. (a) Each arrow indicates wavevector of a standing wave laser. (b) The surface plot of optical potential for the kagome lattice. The dark blue spots indicate lattice minima for a kagome lattice. (c) A one dimensional variation of optical potential along the lattice minima.

potential for a trimerized kagome lattice is given by,

$$V(\mathbf{r}) = V_0 \sum_{j=1}^{3} [\cos(\mathbf{k}_j.\mathbf{r} + 3\sigma_j\phi/2) + 2\cos(\mathbf{k}_j.\mathbf{r}/3 + \sigma_j\phi/2) + 4\cos(\mathbf{k}_j.\mathbf{r}/9 + \sigma_j\phi/6)] \tag{2.25}$$

where $\sigma_1 = -\sigma_2 = \sigma_3 = 1$ and $\mathbf{k}_{1,2} = k_0(\frac{1}{2}, \pm\frac{\sqrt{3}}{2})$ and $\mathbf{k}_3 = k_0(-1, 0)$ are the wavevectors of the laser beams. For $\phi = \pi$, the minima of the potential given by Eq. (2.25) form a uniform kagome lattice as shown in Fig. 2.10. A one dimensional representation of the optical potential is shown in Fig. 2.10(c).

To calculate the condensate fraction, n_0/n we consider the lowest band of the

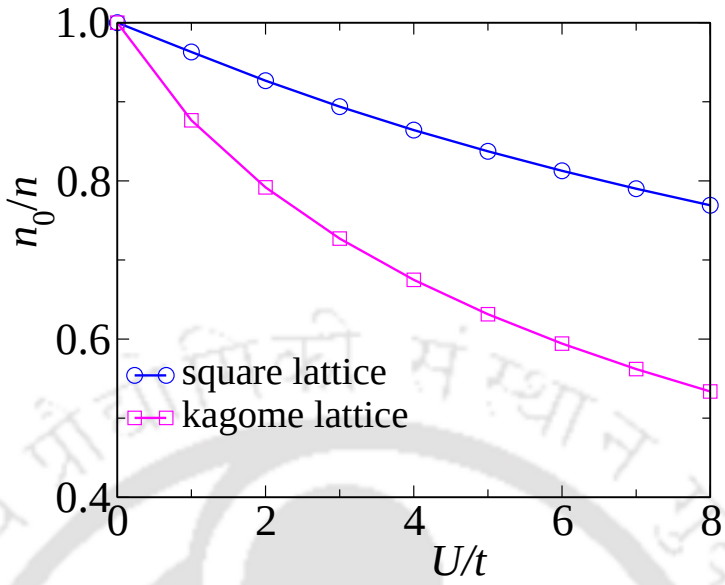

Figure 2.11: The plot shows the condensate density for square and kagome lattices with $n = 1$.

dispersions in Eq. (2.24) and solve Eq. (2.17) as a function of U. From Fig. 2.11 the condensate density for the kagome lattice is found to be significantly lower than that of the square lattice for all values of U. Since Both the geometries correspond to $z = 4$, the condensate properties can not solely depend upon the effective interaction parameter $U'(= \frac{U}{zt})$. The underlying lattice symmetry must be playing an important role.

The above result can be explained again by invoking the nature of the quasi-particle DOS presented in Fig. 2.12. The low energy DOS for the kagome lattice is considerably larger than that of the square lattice, thus allowing the condensate atoms to easily escape the ground state and occupy the higher energy levels, thereby depleting the condensate fraction.

2.5 Conclusions

Our work addresses the interplay of the coordination number and the underlying geometry with that of condensate properties of interacting bosons in 2D optical lattices. The work is likely to be interesting to experimentalists. We have started by demonstrating that a three laser beam configuration with definite polarizations can generate lattice potentials corresponding to square, triangular and honeycomb geometries. A comparison between them with regard to a number of condensate properties, shows an enhanced condensate density in the triangular lattice geometry,

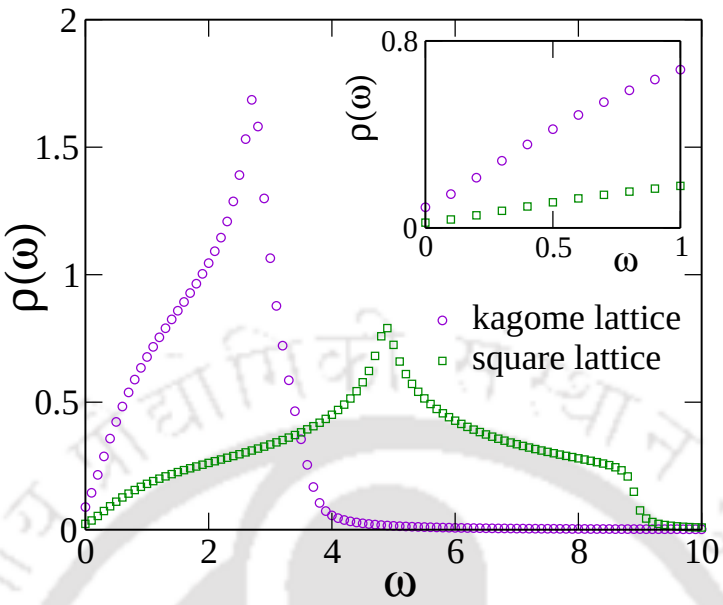

Figure 2.12: The quasiparticle density of states for square and kagome lattices. The plot of $\rho(\omega)$ is obtained at $U = 1$. The low energy quasiparticle DOS for kagome lattice is larger than that of the square lattice.

followed respectively by square and honeycomb lattices. Thus a large coordination number, a large quasiparticle velocity seem to assist condensate properties in these systems. The quasiparticle density of states data for these geometries corroborate the above scenario. To ascertain whether the condensate characteristics are solely functions of the coordination number, or equivalently, whether they depend only on the dimensionless effective interaction parameter, namely, U/zt, we compare the condensate fraction data for square and kagome lattices as both these have same coordination number. The result indeed shows a dependence on the lattice geometry.

Chapter 3

Effect of Random Disorder: Understanding the Bose Glass Phase via a Percolation Scenario

3.1 Introduction

The study of the interplay between disorder and interaction has kept the research on condensed matter physics alive and active for a long stretch of time. As studies involving disorder is a more widely ventured topic in fermionic systems, a brief comparison between the fermion and bosonic systems are indeed compelling. For fermions, the noninteracting ground state is usually the reference point about which the system is perturbed by the disorder potential, however for the bosons, that is not the case, as the noninteracting limit denotes a superfluid. The origin of superconductivity in Fermi systems is in the formation of cooper pairs induced by the attractive interaction that makes the Fermi liquid state unstable, while, as stressed earlier, the superfluidity in a bosonic system occurs due to the competition between the kinetic energy which tends to delocalize the particles, vis a vis the interaction potential which minimizes the density fluctuations by localizing them. Presence of a random disorder plays a very crucial role in either of the cases. Third, and a significant difference between the Bose and Fermi systems, is in their individual response to disorder. Disorder tends to destroy superconducting correlations by inducing localization of the fermion wavefunctions that leads to an insulating behaviour. Very differently, as we shall show in this chapter, random disorder extends the superfluid phase of the bosonic systems. We feel, for reasons elaborated in this work, that there are some unsettled issues in the case of disordered bosons, especially in relation to

the occurrence of a glassy phase, known as the Bose glass (BG), which need to be addressed and discussed in details.

The pioneering studies on bosonic systems, in the presence of disorder[30] were motivated by the experimental results on superfluidity in thin ^4He films on Vycor glass[72]. The scope of studying the interplay of disorder and interaction effects in Bose systems have been vastly expanded with the advent of cold atoms in optical lattices. By and large, optical lattices offer defect free systems and a situation in which the interatomic interaction can be conveniently modified using a Feshbach resonance. Technical advancement at a rapid pace is going on to incorporate disorder in optical lattices, such as laser speckle pattern[21,22,128,129], two colour superlattice[24,26] or using different atomic species that may mimic random disorder[27,43,130]. A short description of these have already been presented in the introduction.

An important dividend of the whole endeavour of studying disorder in bosonic systems is the emergence of a compressible glassy phase with no long range order, called the Bose glass phase[131]. Initially the question was whether a BG phase is always intercepted between a SF phase and a Mott insulating (MI) phase. The question was comprehensively answered in the form of a theorem, namely *"theorem of inclusions"*[73] (see introduction).

In our work, we take a clue from all these inputs and ask a basic question: what is the extent of the BG phase in the interaction-chemical potential $(U - \mu)$, $T = 0$ phase diagram? How does it intervene between the SF and MI phases? While attempting to answer some of these questions, we found that the BG phase appears as the sites with integer occupancy percolates through the two dimensional lattice. To our surprise, the percolation threshold is found to be nearly the same as that for a (noninteracting) random site percolation model[132]. The percolation threshold is critically examined by observing a spanning cluster of integer sites to appear for the first time. Such a site percolation scenario was proposed recently in the context of extended BHM to understand the disorder induced supersolid phase in a cubic lattice[133]. However in contrast to our work, the authors of Ref.[133] used the random site percolation threshold, namely 0.31 (in three dimensions), to estimate the critical disorder strength for the supersolid phase to appear. Nonetheless, percolation is believed to provide an intuitive picture for explaining the onset of the supersolid phase details of which will be taken up for discussion in subsequent chapters.

We organize this chapter as follows. In the next section, for the sake of completeness, a quick recapitulation of the mean-field formalism on the disordered BHM that we have used to study the BG phase is presented. Hence we have included a

discussion on the distribution of the superfluid order parameter and the occupation density (defined in the following section). Further, we define quantities such as the ratio of the sites with integer occupancies with no superfluid order to the total number of sites, relative fluctuation of boson density and information entropy etc. Such physical quantities will be instrumental in distinguishing the BG phase from that of the SF and MI phases. In section 3.3, we present our results on the percolation scenario that marks the onset of the BG phase by observing a spanning cluster to appear and hence compute the number of sites in the spanning cluster and the corresponding mean cluster size. The implications and importance of our results are presented thereafter.

3.2 Models and the Physical Properties

Our starting point is the disordered BHM, which is written as,

$$H_{BHM} = -t\sum_{\langle ij\rangle}(b_i^\dagger b_j + h.c.) + \frac{U}{2}\sum_i \hat{n}_i(\hat{n}_i - 1) + \sum_i(\epsilon_i - \mu)\hat{n}_i \qquad (3.1)$$

where $b_i^\dagger(b_i)$ creates (annihilates) a particle at site i, t represents the nearest neighbour hopping term, U is the interparticle repulsion, μ is the chemical potential, n_i is the number of bosons and ϵ_i is a random onsite energy picked from a uniform rectangular distribution (mentioned later). All the energy parameters, namely, U, μ and ϵ_i (or Δ as explained later) hereafter are scaled by the hopping zt (z: coordination number). Thus, henceforth all the parameter values will simply be quoted as numbers with the understanding that they are denoted in units of zt. Same is true for all the subsequent chapters.

The standard mean field approach involves a decoupling of the kinetic energy into the following form,

$$b_i^\dagger b_j \rightarrow \langle b_i^\dagger\rangle b_j + b_i^\dagger\langle b_j\rangle - \langle b_i^\dagger\rangle\langle b_j^\dagger\rangle. \qquad (3.2)$$

Here $\langle b^\dagger\rangle = \langle b\rangle = \psi$ (say) represents the superfluid order parameter, vanishing of which marks the onset of an insulating phase. This decoupling reduces the many particle Hamiltonian in Eq. (3.1) to a single particle one and leaving aside the site index and the nearest neighbour contribution on ψ is neglected (see Eq. (1.40)), which should be valid at low disorder strengths (where mean field theory is justifi-

able), the Hamiltonian can be written as,

$$H^{MF} = \frac{U}{2}\hat{n}(\hat{n}-1) - (\mu-\epsilon)\hat{n} - \psi(b+b^{\dagger}) + |\psi|^2. \tag{3.3}$$

We have solved Eq. (3.3) selfconsistently in the truncated occupation number basis $|n\rangle$ with $n_{max} = 8$[70]. We have checked that the ground state energy converges for this value of n_{max} (see Fig. 1.6 in chapter 1).

About incorporating the disorder contribution in our calculations, we have taken an energy ϵ_i at each site randomly from a uniform, normalized rectangular distribution (see Fig. 3.1), $P(\epsilon)$ given by,

$$\begin{aligned} P(\epsilon_i) &= \frac{1}{2\Delta};\ -\Delta \leq \epsilon_i \leq \Delta \\ &= 0; \quad \text{otherwise} \end{aligned} \tag{3.4}$$

where Δ represents the strength of disorder. The disorder introduces a Bose glass

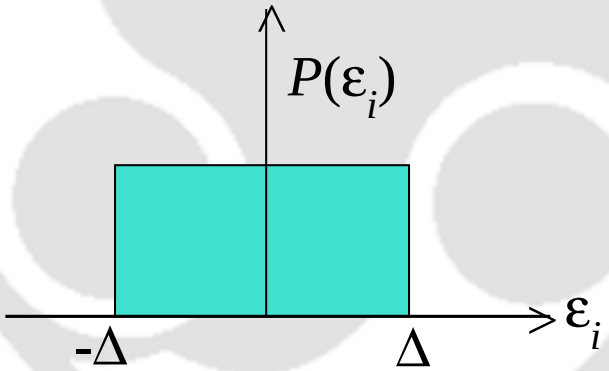

Figure 3.1: The schematic diagram of the distribution probability $P(\epsilon_i)$ of the local onsite random potential energy ϵ_i.

phase, which otherwise is absent. The Bose glass phase is characterized by a zero (bulk) superfluid order parameter ($\psi = 0$) and nonzero compressibility. Based on this information, we wish to locate the region spanned by the BG phase in the phase diagram defined by the U and μ.

It will be helpful at this stage to define a few quantities that are of importance for our subsequent discussion. They are ratio of the sites with integer occupancies with vanishing order parameter, ψ to that of the total number of sites, denoted by γ; the compressibility, κ or equivalently the density fluctuation, δn_{rel} and the information entropy, S. We shall provide a quick enumeration of these quantities and a discussion to demonstrate how these quantities are of relevance in identifying

the extent of the BG phase or even more generally, distinguishing between the SF, BG, and MI phases.

Based on the criterion provided in Ref.[70], the appearance of a percolating cluster of sites with integer occupancy is linked with the onset of the BG phase. Hence γ can be calculated corresponding to such a situation and can thus be used to distinguish between the MI, SF and BG phases. For small values of U, $\gamma = 0$ indicates absence of sites with integer occupancy, or equivalently the presence of a SF phase. The pure case registers a sudden jump of γ from 0 to 1 at $U = U_c$ which marks a direct transition from a SF to a MI phase. However in the presence of disorder, the increase of γ with increase in U is more gradual, hinting at the appearance of a significant region (in the $\mu - U$ phase diagram) occupied by the BG phase that intervenes between the SF and MI phase.

There is a subtle point that deserves a special mention. As mentioned earlier, we also demand the order parameter ψ to be zero, while defining γ. This is so, since in the SF region of the phase diagram (*i.e.* for $U < U_c$), there is a unique line along which all the sites acquire integer occupancies ($n = 1$, $n = 2$ etc.) and hence γ will assume a value unity. However this line does not belong to the MI phase as the order parameter is non-vanishing along the line and thus denotes a SF phase. Since this issue does not have an impact on the central theme of the calculations, we shall ignore it in the subsequent discussion.

We illustrate the percolation scenario by observing the formation of a spanning cluster of sites with integer occupancies. The way to do this is to calculate a γ_∞ defined by the ratio of sites in the spanning cluster to the number of sites with integer occupancies. Before a spanning cluster is formed, γ_∞ remains at zero, while it becomes finite as soon as a spanning cluster appears.

One has to be careful in distinguishing this with the random site percolation problem. In the latter case, the tuning parameter is the random occupation probability, whereas for our case, the percolation threshold is reached by tuning the parameters of the Hamiltonian, namely, U and μ, thereby signaling an impending transition to a BG phase. Further, the size dependence of γ_∞, which is a generic feature of the percolation problem, seems to be absent here. These issues have been elaborate in section 3.3.

To gain further insights into the ongoing discussion, we compute the probability that a site with integer occupancy (and $\psi = 0$) chosen at random is a part of a

's'-site cluster and the mean cluster size which is defined by,

$$C_s = \frac{\sum_s s^2 n_s(\gamma)}{\sum_s s n_s(\gamma)} \tag{3.5}$$

where $n_s(\gamma)$ is the mean cluster size distribution written as,[134]

$$n_s(\gamma) = \frac{\text{average number of clusters of size } 's'}{\text{Total number of lattice sites}}. \tag{3.6}$$

Incidentally the correlation (or connectivity) length, ξ that diverges at the percolation threshold is also proportional to the mean cluster size[135]. C_s and ξ have counterparts in the thermally driven phase transition. For example, C_s plays the role of compressibility in fluids and ξ diverges near the critical point.

To supplement our results on obtaining the phase diagram, we compute the compressibility, κ which is defined as $\kappa = -\frac{\partial^2 F}{\partial \mu^2}$, F being the free energy. A measure of it is provided by the relative number fluctuations of the bosonic density[136],

$$\delta n^2{}_{rel} = \frac{\langle \hat{n}^2 \rangle - \langle \hat{n} \rangle^2}{\langle \hat{n} \rangle^2} \tag{3.7}$$

where $\langle n \rangle = \langle b^\dagger b \rangle$. A plot of δn_{rel} as a function of the interparticle repulsion, U in presence of a random disorder potential yields a gradual decrease of δn_{rel} as U is increased. It complements the information obtained from γ in the following way. At large U, δn_{rel} should vanish, thereby implying an insulating phase. At lower values of U, δn_{rel} is finite. What may distinguish between a direct SF to MI transition to that of one that is intervened by a BG phase is the sharpness with which δn_{rel} vanishes. In the pure system, the vanishing of δn_{rel} is sharp, indicating the presence of a sharp MI-SF boundary. However the presence of disorder yields a gradual fall off, delaying a complete disappearance of the number fluctuations. The delay is due to the emergence of the BG phase which is characterized by a finite compressibility and hence a finite fluctuation of the boson density. A comparison with the pure case yields an estimate of the extent of the BG phase in the phase diagram.

A third useful quantity in this regard can be the configurational entropy (or simply referred to as entropy hereafter) of the system which is defined by[137],

$$S = \frac{1}{N} \sum_{i=1}^{N} n_i \ln n_i \tag{3.8}$$

where $n_i = \langle {b_i}^\dagger b_i \rangle$. As earlier, for a given value of the random disorder and at smaller values of U, S should be independent of disorder, thereby implying the robustness of the superfluid phase. However at larger U, or corresponding to the boundary of MI-SF phases, presence of disorder distinguishes the behaviour of the entropy and the distinction becomes clear at larger values of disorder, as will be shown in the next section.

3.3 Results

In this section we present our results that distinguish and ascertain various phases for the system of bosons in the presence of disorder. The first step in this direction is taken by solving Eq. (3.3) numerically, as mentioned earlier, on a two dimensional square lattice of size $L \times L$ ($L = 32$ taken everywhere) in the occupation number basis, $|n\rangle$, for a maximum occupation number $n_{max} = 8$. It may be noted that we have considered even larger values of L, however the main results of this thesis remain qualitatively unaltered. Hence selfconsistent determination of the superfluid order parameter, ψ ($= \langle b \rangle$) is done. $\psi \neq 0$ defines a SF phase and vanishing of ψ defines the MI phase.

Another subtle issue at this point is worth mentioning. We calibrate the value of the order parameter that defines the MI phase as in the following. In other words, we answer the question that what should be the value of ψ in numerics so as to term it as 'zero' and thereby define the MI phase. The critical value of the interparticle repulsion, namely U_c at which the MI phase is realized for the first time (corresponds to the boson density $n = 1$) is a known value, namely 5.83[70]. Calibrating against this known value of U_c yields ψ to be approximately $\mathcal{O}(10^{-3})$. Thus values for ψ equal or smaller than 10^{-3} taken as $\psi \simeq 0$ and thus will define the MI phase, while the value of ψ in the SF phase is of the order of unity. This discussion will also be relevant later. For the pure case ($\Delta = 0$), there is a sharp boundary that separates the MI ($\psi \simeq 0$) and SF ($\psi \neq 0$) phases. At $\Delta \neq 0$, BG phase should intervene.

In Fig. 3.2(a) and (b), we show the distribution of the superfluid order, ψ and also the occupation density, n in (c) and (d) for a given disorder configuration (we have seen a number of different random configurations with no noticeable change). For the SF phase, Fig. 3.2(a) and (c), $P(\psi)$ attains a significant value only for $\psi \simeq 1$ and the density, n remains a non-integer respectively. However in the BG phase, $P(\psi)$ stays vanishingly small for all finite ψ, while $P(n)$ peaks at $n = 1$ (Fig. 3.2(b) and (d)), as we are in the vicinity of the $n = 1$ MI lobe. To us, this is the simplest

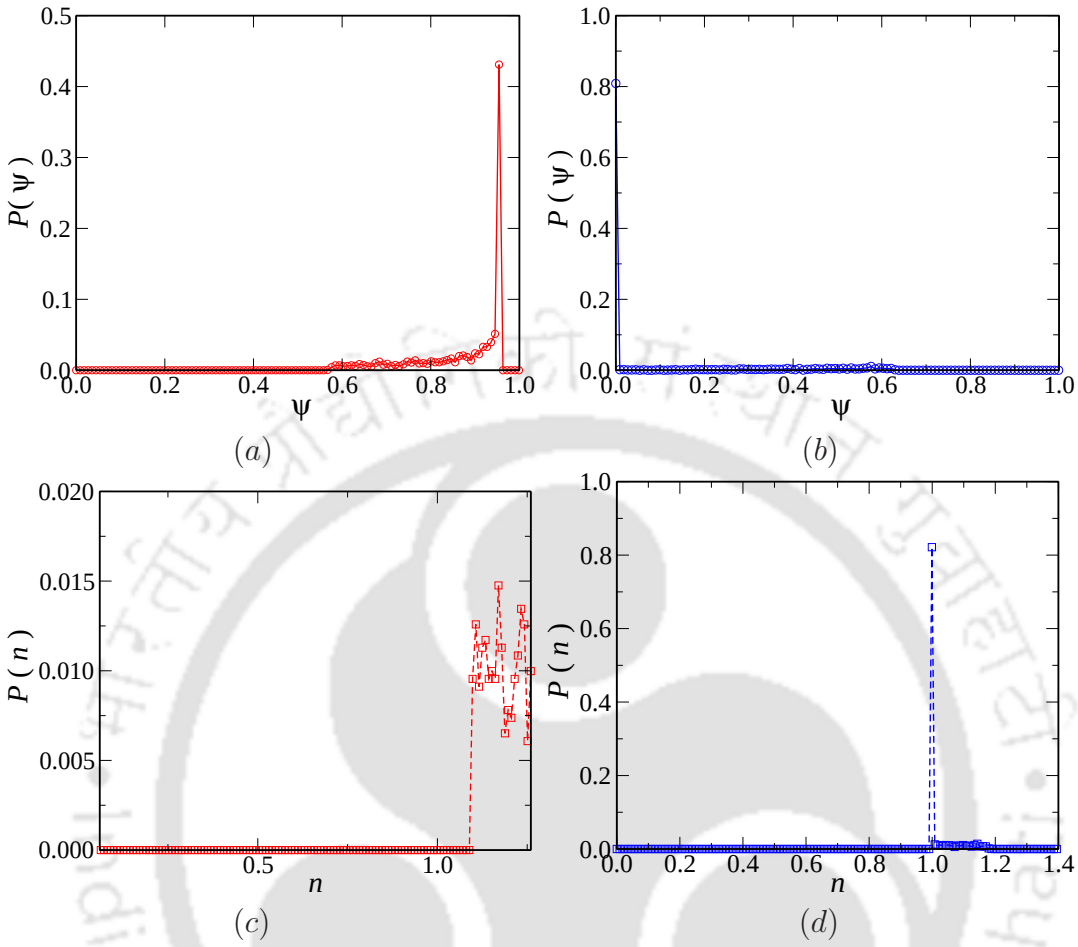

Figure 3.2: The distribution of the order parameter, ψ and the occupation density, n are shown. (a) and (c) correspond to superfluid phases and (b) and (d) denote the BG phases.

demonstration of the existence of the BG phase. It may be noted that for the MI phase, $P(\psi)$ and $P(n)$ will be nonzero only for $\psi = 0$ and $n = 1$ respectively.

Now we reiterate some of the questions that we raised earlier. They are, what is the extent and location of the BG phase? Does the BG phase encroach into the SF phase or the MI lobes? Given a set of μ, U and a disorder strength Δ, can we determine the phase with confidence?

To answer these questions satisfactorily we need to rely upon some quantities that should support each other in terms of determining the location, shape and extension of the BG phase. Our idea is to take an intersection of the information thus obtained and generate the phase diagram.

As said earlier, we predominantly depend upon the concept of appearance of a percolating cluster of sites with integer occupancies and vanishing order parameter as the onset of the Bose glass phase[96], where the system effectively splits into two

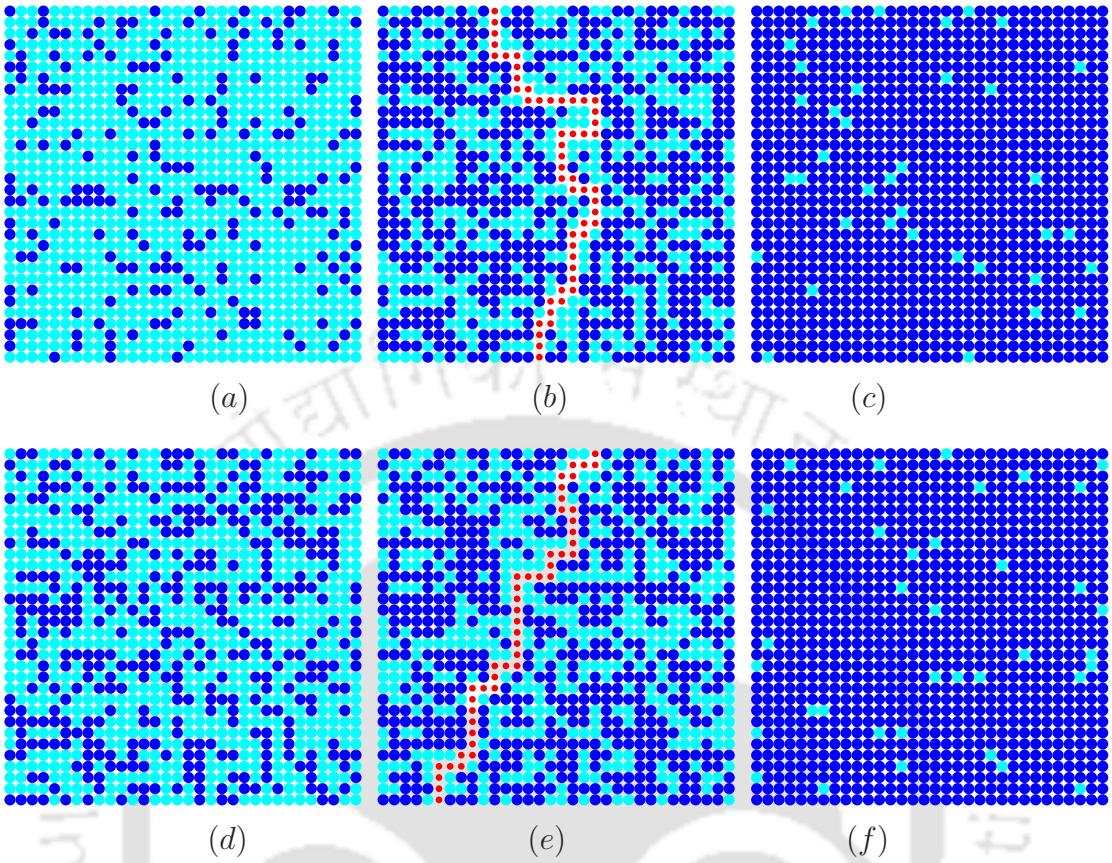

Figure 3.3: The real space plots of boson densities having integer (dark blue) and non-integer (light blue) occupancies for a 32×32 lattice at disorder strength $\Delta = 2$ are shown. (a)-(c) correspond to fixed $\mu = 6$ and at U values 7.5, 8.75 and 10.15 respectively. (d)-(f) are for $U = 10$ and μ values 1, 1.7 and 3.2 respectively. $\gamma \sim 0.6$ in (b) and (e), integer sites percolate for the first time. (a) and (d) are corresponding to $\gamma < 0.6$ whereas (c) and (f) are for $\gamma > 0.95$. In both the cases (b) and (e), the percolating paths are shown by small red circles. U, Δ and μ are denoted in units of zt (z: coordination number) and is true for all subsequent plots.

large superfluid islands separated by an insulating strip. In our work, the appearance of the percolating cluster is confirmed by carefully examining the presence of a percolating path of sites with integer occupancies (with $\psi = 0$) at all U, μ values for a given value of disorder. We see that the percolating cluster scenario occurs at a γ value of 0.598 (the computation of this precise value and its reliability is mentioned in subsequent discussion) and this value remains same for both the disorder strengths $\Delta = 1$ and $\Delta = 2$ that are considered in this work. In Fig. 3.3 we show the real space plot for the bosonic density. The sites with integer filling are marked by dark blue colour and non-integer ones are marked by light blue colour for different sets of (U, μ). Fig. 3.3(a)-(c) probes the system at a given value of μ $(= 6)$ [138] for three different U values (7.5, 8.75 and 10.15) such that we are able to scan phase diagram

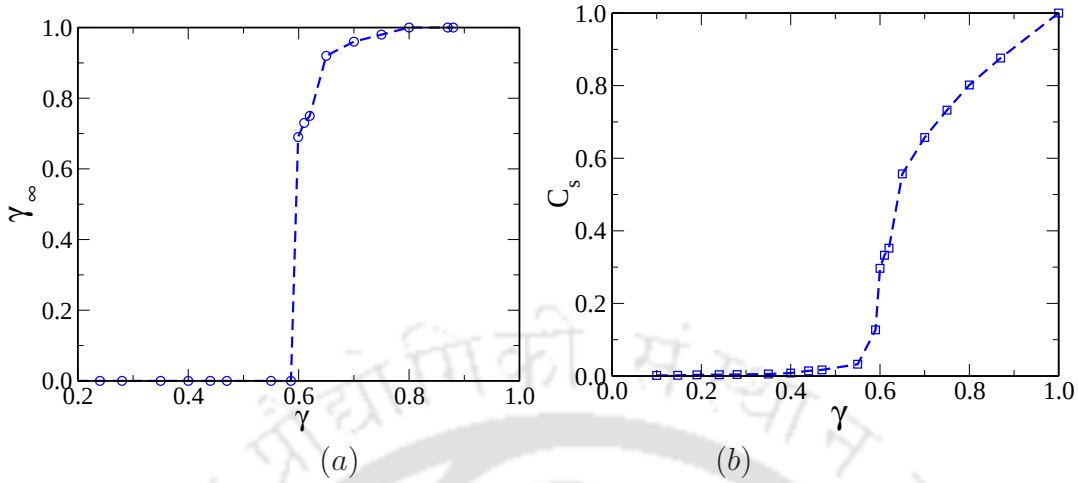

Figure 3.4: The variation of γ_∞ (in (a)) and the mean cluster size, C_s (in (b)) (defined in text) are shown as a function of γ. γ_∞ becomes nonzero for the first time at $\simeq 0.598$, a value well known as a percolation threshold of a random site percolation model.

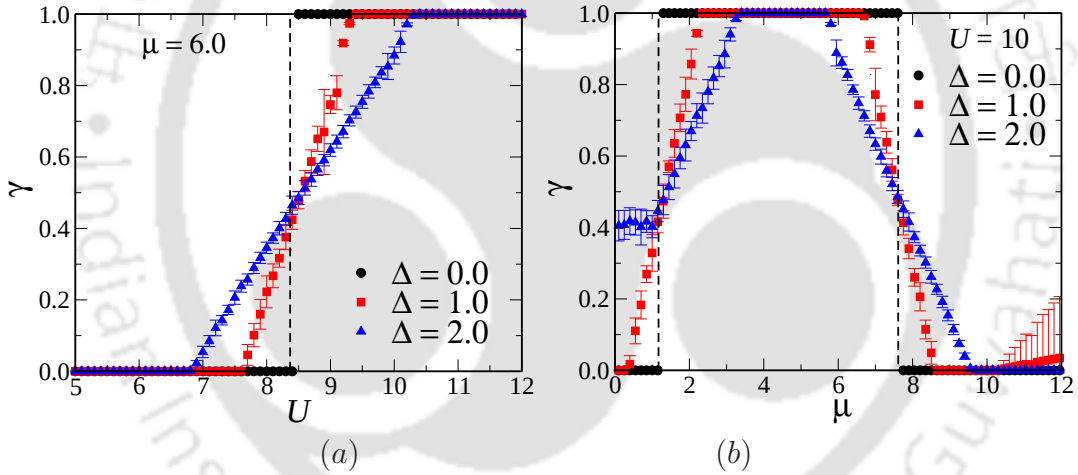

Figure 3.5: The variation of γ defined in text is presented in (a) as a function of U at $\mu = 6$ and in (b) as a function of μ at $U = 10$ for different disorder strengths Δ of value 1 (in red squares) and 2 (in blue triangles). The pure case (in black circles) is included for comparison. The sharp change in the values of γ between 0 and 1 in absence of disorder indicates direct SF-MI transition. Gradual change of γ indicates the transition occurs between SF and MI phase via a BG phase in presence of disorder. The results shown are averaged over 25 distinct realizations. The error bars are computed using Eq. (3.10).

(formed by $U - \mu$) horizontally.

To access a vertical scan, we consider three different μ values (1, 1.7 and 3.2) for a given $U(= 10)$ and are shown in Fig.3.3 (d)-(f). The reason behind choosing the (U, μ) values are such that we are able to address all of SF, BG and MI phases. The percolating paths of the integer sites are shown in Figs. 3.3(b) and (e) corresponding to the onset of the BG phase. In both cases, γ is found to be 0.598, a value close

to that known for a square lattice in the random site percolation problem. Thus the formation of the BG phase starts at the corresponding U, μ values at which the percolating cluster appears for the first time.

However finding the "*appearance of the percolating cluster for the first time*" is a considerable job, although crucial for us, as the appearance of the BG phase is linked with this issue. To shed light on this, we compute the ratio γ_∞, defined as,

$$\gamma_\infty = \frac{\text{Number of sites in the spanning cluster}}{\text{Total number of sites with integer occupancy and } \psi = 0} \tag{3.9}$$

γ_∞ is zero for $\gamma < \gamma_c$, where γ_c denotes the percolation threshold. Thus we look for the value of γ for which γ_∞ becomes nonzero for the first time for a given value of disorder by tuning U and μ values, so as to access the onset of BG phase. Close to γ_c, U and μ values are carefully monitored and we get γ_∞ to become nonzero for the first time at $\gamma = 0.598$ (see Fig. 3.4(a)). We further investigate the percolation scenario by computing the cluster size distribution and hence mean cluster size, C_s (defined by Eq. (3.5)), which as a function of γ, is shown in Fig. 3.4(b). It can be seen that C_s becomes significant only at $\gamma \simeq \gamma_c$.

We consider Fig. 3.4 to be an important component of the ongoing analysis as it is able to track the onset of the BG phase in a satisfactory manner. It is a dividend that the value at which it occurs is very nearly the same with that of a random site percolation model. We wish to reiterate that such a similarity in the value of the percolation threshold between a noninteracting random model to that of a model interacting boson is truly an accidental one in which the random occupation probability is replaced by γ. The latter constitutes an important machinery of our analysis.

The next task is, how to find till what (U, μ) values does the BG phase extend to. To find out that, we refer to Fig. 3.5(a) and look for γ as a function of U for a given μ[138] to reach about 0.95, such that the order parameter ψ becomes of the order of 10^{-3} which can be taken as zero (as discussed earlier), beyond that value of U.

For the pure case, γ is seen to have a very sharp jump from a value 0 (SF) to 1 (MI) at a particular U ($= 8.4$) indicating a sharp boundary between the MI and SF phases. However the sharpness of the jump goes away in presence of disorder, where the rise in γ becomes more gradual. The higher disorder value ($\Delta = 2$) registers an even slower increase, thereby implying a large region in the $U - \mu$ phase diagram for the BG phase at this value of disorder. Further the positive slope of γ indicates

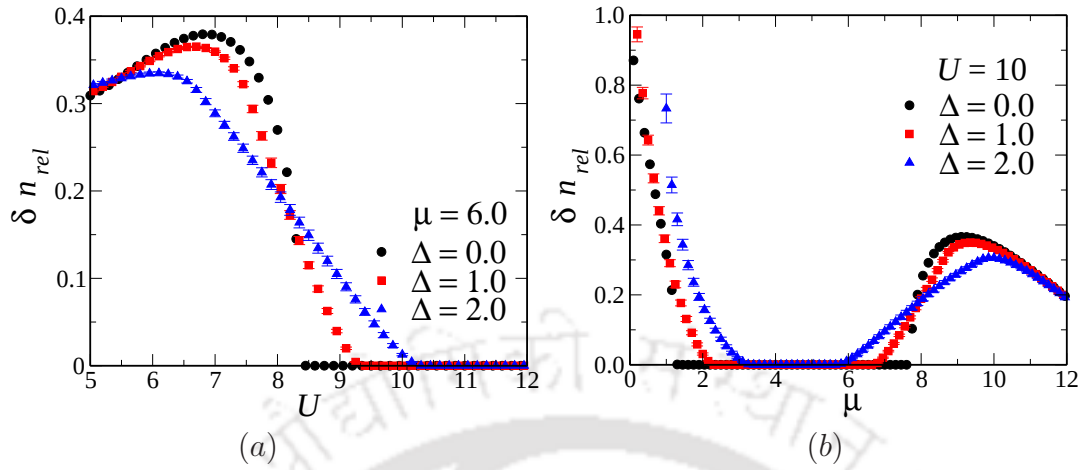

Figure 3.6: The relative fluctuations, δn_{rel} (defined in text) as a function of U in (a) and μ in (b) for same disorder strengths as in Fig. 3.5. δn_{rel} vanishes sharply for the pure case, while the fall off is slow for disordered cases. A vanishing δn_{rel} indicates the MI phase.

that the BG phase encroaches into the MI phase (the right portion of the dashed vertical line in Fig. 3.5(a) is the MI phase for the pure case) and also yields bigger room for the SF phase ($\gamma < 0.6$).

The error bar shown in the figures are computed using the following formula[139],

$$\sigma = \sqrt{\frac{1}{(N_c - 1)} \sum_{i}^{N_c} (x_i - \bar{x})^2} \tag{3.10}$$

where the average $\bar{x}$ is defined by $\bar{x} = \frac{1}{N_c} \sum_i^{N_c} x_i$, N_c being the number of disorder realization considered here and x_i is the data corresponding to i^{th} realization. In most of the cases we have taken $N_c = 25$.

It is also useful to scrutinize the situation corresponding to a constant U and as a function of μ, which suggests taking a vertical scan of the phase diagram. In Fig. 3.5(b), corresponding to $U = 10$, again a sharp rise in the γ value from 0 to 1 is noted for the pure case at some threshold value of U, while one sees a more gradual increase in γ for the disordered cases. For higher μ values, we realize again an emergence of a SF phase via a BG phase (a direct MI-SF transition for the pure case).

To seek further support of the above scenario, we compute the relative fluctuations of the boson density (which as discussed is proportional to the compressibility) and again notice a sharp fall off as a function of U for a given μ $(= 6)$ at U $(= 8.4)$, while the fall off is delayed for the disordered cases as seen in Fig. 3.6(a). The slow

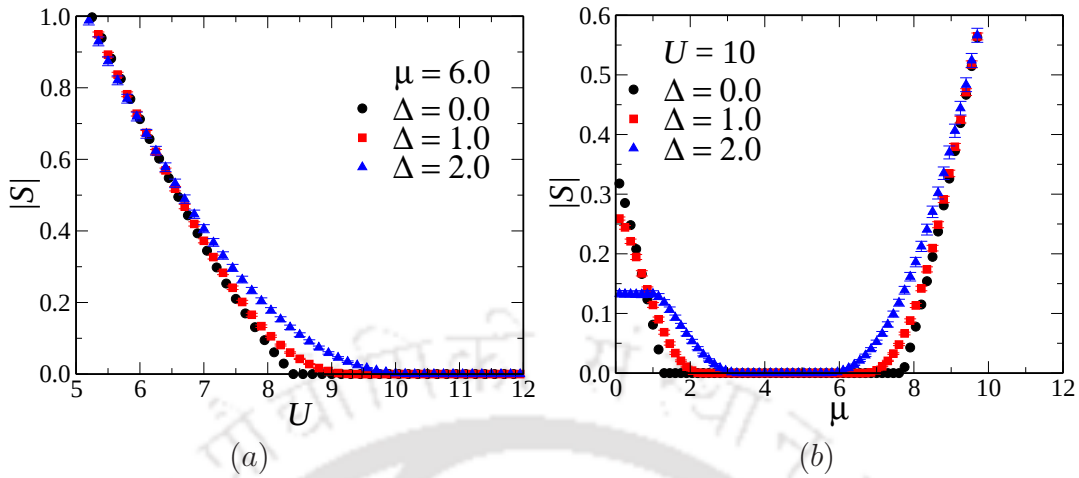

Figure 3.7: The entropy S (defined in text) is presented for (a) $\mu = 6$ as a function of U and (b) $U = 10$ as a function of μ for disorder strengths as in Fig. 3.5.

fall off beyond $U = 8.4$ is taken as proof for the presence of the BG phase and the region to the right of that value of U yields a measure of the extent of the BG phase. It is easily noticeable that there are enhanced fluctuations as one moves closer to the SF-BG boundary (SF-MI boundary for the pure case) before the fluctuations vanish (onset of MI phase). However, enhanced fluctuations are damped in the disordered case. A similar notion emerges from Fig. 3.6(b) which shows the relative fluctuation of the particle density of bosons as a function of the chemical potential, μ for a given $U = 10$.

We substantiate our claim further on the above findings by computing the entropy, S as defined in Eq. (3.8) which for a particular μ and a function of U (Fig. 3.7(a)) repeats a quick fall off for the pure case ($\Delta = 0$) and a gradual vanishing for the disordered cases ($\Delta \neq 0$). When we move vertically in the phase diagram, new features emerge (see Fig. 3.7(b)). At lower values of μ, S has noticeably different values for the disordered and pure cases, indicating the existence of a BG phase in the vicinity of the boundary separating the SF and MI phases. The above is followed by a large region of μ where S vanishes (since the occupancy is unity) and there is no distinction between the pure and disordered cases, thereby signaling a large region within the $(n = 1)$ MI lobe, which is hence subtended by another BG region at larger values of μ.

The results are summarized in table 3.1, which shows the finite entropy change for three disorder strengths. A closer inspection of the values corresponding to different phases reveals that the change in entropy $\delta S = |S_{SF} - S_{BG}|$ decreases with increase in disorder strengths, that is $\delta S_{\Delta=2} < \delta S_{\Delta=1}$. Since the non-integer site occupancies

Phase	S_0	S_1	S_2
SF	0.498	0.493	0.495
BG	$---$	0.004	0.047
MI	0.0	0.0	0.0

Table 3.1: The table shows the value of entropy, S defined in the text, at (U, μ) values (10, 6), (10, 7) and (10, 9.5). The (U, μ) values that correspond to deep inside the MI, BG and SF phases respectively. The subscript of S denotes the disorder strength. In the SF and MI phases, S is independent of Δ, whereas its value depends on Δ in the BG phase.

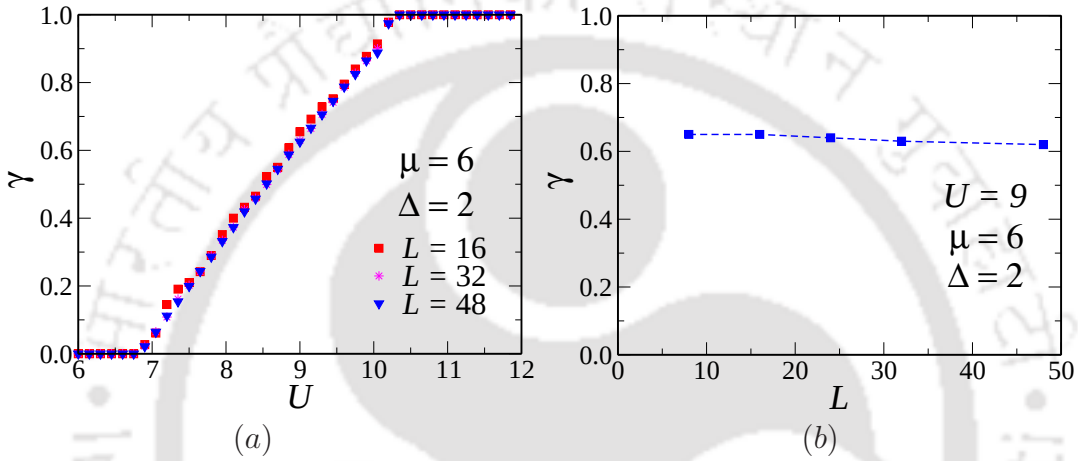

Figure 3.8: The variation of γ as a function of U for different system sizes, L in (a) and in (b) dependence of one data point for γ as a function of system size L are shown. Both the plots show γ to be independent of L.

contribute to the finiteness in S (and integer occupancies contribute zero), a decrease in δS as a function of disorder indicates a prolonged SF phase and hence the notion of the BG phase consuming the Mott lobes in the phase diagram is appropriately justified.

Further, we have not noted any noticeable system size effects for the quantities that are calculated in our work. A representative study of the size dependence on γ as a function of interaction parameter, U is shown in Fig. 3.8(a). Here we have chosen a particular value of chemical potential, μ and disorder, Δ. The reason for choosing such parameter values will be clear in the next section. Fig. 3.8(b) shows the dependence of one particular data point for γ at a given U as a function of system size L. The system size effect, if any, is vanishingly small.

Based on all the information presented above, we present the phase diagram in Fig. 3.9(a) $-$ (c). In each of the figures, the inner lobe denotes the MI phase characterized by $\gamma \simeq 1$ (and $\psi = 0$), the region that envelopes the MI lobe is the BG phase for $0.6 \leq \gamma < 0.95$), and finally the outer region at low U values denotes

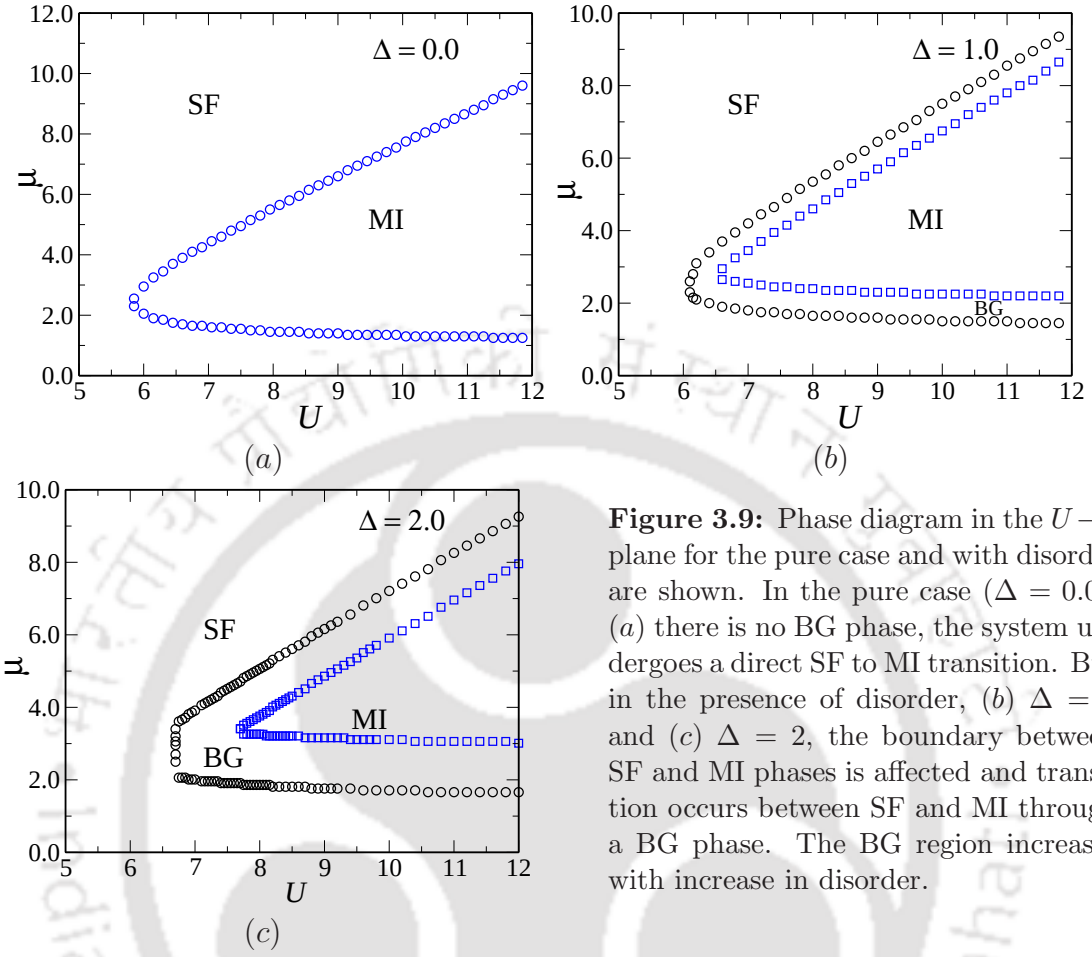

Figure 3.9: Phase diagram in the $U-\mu$ plane for the pure case and with disorder are shown. In the pure case ($\Delta = 0.0$), (a) there is no BG phase, the system undergoes a direct SF to MI transition. But in the presence of disorder, (b) $\Delta = 1$ and (c) $\Delta = 2$, the boundary between SF and MI phases is affected and transition occurs between SF and MI through a BG phase. The BG region increases with increase in disorder.

the SF phase with $\gamma < 0.6$ (γ vanishes deep inside the SF phase).

We show our results for two values of disorder, *viz.* $\Delta = 1$ and $\Delta = 2$. The pure case ($\Delta = 0$) is included for comparison. The BG phase is shown to appear only for the disordered cases and it grows in size as the disorder is increased.

An alternate method to obtain the phase diagram via minimization of the free energy for the uniform disorder case is demonstrated in the Appendix B. The method described there can trivially be extended to other kinds of (non-uniform) disorder models.

3.4 Conclusion

Using the physical quantities such as the ratio of the sites with integer occupancies to that of the total number of sites, relative fluctuation of the particle number for bosons and information entropy, we have been able to precisely obtain the phase diagram for the Bose Hubbard Model in the presence of random onsite disorder.

These results were thoroughly tested by taking horizontal (μ fixed and as a function of U) and vertical (U fixed and as a function of μ) scans of the phase diagram. Thus to be able to unambiguously determine the phase of the system at arbitrary values of U, μ and Δ is the central theme of this work. Further, the BG phase is seen to encroach and consume the area otherwise spanned by Mott lobes without disorder, thereby creating a larger regime for the SF phase. This precisely differentiates between the Bose and Fermi cases, where in the latter, long range is destroyed by the disorder, while it is stabilized in the former. Hence the SF phase persists till large value of U. The BG phase itself increases in size with disorder. The emergence of the BG phase is marked by the formation of percolating cluster of integer sites with zero superfluid order with the percolation threshold to be same as the value obtained for a random site percolation model in two dimensions.

It may be noted that the continuous percolation induced transition to the BG phase, where γ smoothly evolves from a value below ~ 0.6(SF), to above that (BG), can be looked upon as an artifact of the mean field theory where all the sites of a lattice are decoupled. The argument can be substantiated in the following sense. As one goes beyond the mean field picture, and say resort to a random phase approximation (RPA) study[96], localization is seen to be enhanced by the percolation scenario as evident from the behaviour of the participation ratio (or its inverse) which is a measure of the extent of the region over which the eigenstates of the system extend as a function of the disorder strength, Δ (see Fig. 3 of Ref.[96]). A steady increase in the participation ratio as a function of Δ signals a percolation enhanced localization tendency, a feature missed out in the mean field picture.

Chapter 4

Phase Diagram of Bosons in a Tripartite Lattice: Case Study for Non Bipartite Lattices

4.1 Introduction

We have amply stressed that the physics of the cold atoms in optical lattices has developed into an intense research area due to its possible relevance to quite a few interesting quantum many body phenomena that are abundant in condensed matter physics. The research interest is intensified due to the unprecedented control on various parameters of the Hamiltonian[6,7]. Further possibility of achieving different kind of lattice geometries by employing counter propagating laser beams have increased the research interest in the study of interacting bosons on optical lattices with exotic geometries[112,114,115,117,140–147]. We have discussed in chapter 2 that how the trimerized optical kagome lattices have been created experimentally by using three standing waves with a $\pi/3$ angle between them, where each standing wave results from three sets of counter propagating laser beams as shown in Figs. 2.10 of chapter 2.

While the stage appears set for experimentally realizing different polymerized lattices, need for a theoretical prediction of the phase diagram seems necessary. In this work we present a phase diagram of bosons on a tripartite lattice.

At the outset we make it clear that by a tripartite lattice, we mean that the lattice sites can be divided into three types, where sites of each type has neighbours of the other two types, and discuss various density ordered phases that bear signatures of such a three sublattice structure. Let the three types of sites are denoted by A,

B and C. So A will have two neighbours each of types B and C and so on. The diagram in Fig. 4.1 show this schematically.

We organize this chapter as follows. Mean field decoupling scheme[30,70] is revisited for an extended Bose Hubbard model (EBHM) which reduces the Hamiltonian for the entire lattice to a three site problem. A strong coupling expansion is hence done to obtain the ground state energy of the system in terms of the order parameters, which is hence minimized to obtain a phase diagram. Further support and additional input in terms of realizing supersolid phases is achieved by numerically solving the mean field Hamiltonian as described later in the chapter.

4.2 Formalism and Results

The utility of an extended model that includes a longer range (nearest neighbour) interaction term to mimic the dipolar interaction found in certain atomic species as discussed in chapter 1. A longer range interaction on a lattice is modeled by a nearest density interaction and thus we have started with an extended Bose Hubbard Hamiltonian, denoted by,

$$H = -t\sum_{\langle ij\rangle}(b_i^\dagger b_j + h.c.) + V\sum_{\langle ij\rangle}\hat{n}_i\hat{n}_j + \frac{U}{2}\sum_i \hat{n}_i(\hat{n}_i - 1) - \sum_i \mu_i\hat{n}_i \tag{4.1}$$

while all other symbols carry the same meaning as earlier, V represents the nearest neighbour exchange interaction of occupation densities. In presence of the nearest neighbour term (*i.e.* $V > 0$) the ground state of the model in Eq. (4.1) exhibits density ordered (DW) phase (see table 4.2 and the discussion thereof). Unlike a bipartite lattice, where the insulating ground state alternates between a superfluid (SF) to a Mott insulating (MI) or DW and MI phases[67,94,148], we consider three different sublattices and obtained additional phases such as DW ($\frac{1}{3}$), DW ($\frac{2}{3}$) and MI (1) insulating phases which repeat in that order with increased occupancies as the chemical potential is increased.

To solve the Hamiltonian in Eq. (4.1) in the truncated on-site occupation number basis $|n\rangle$, we use standard mean field decoupling scheme for the hopping and extended terms as[94],

$$\begin{aligned} b_i^\dagger b_j &\rightarrow \langle b_i^\dagger\rangle b_j + b_i^\dagger\langle b_j\rangle - \langle b_i^\dagger\rangle\langle b_j\rangle \\ \hat{n}_i\hat{n}_j &\rightarrow \langle\hat{n}_i\rangle\hat{n}_j + \hat{n}_i\langle\hat{n}_j\rangle - \langle\hat{n}_i\rangle\langle\hat{n}_j\rangle. \end{aligned} \tag{4.2}$$

The above decoupling reduces Hamiltonian in Eq. (4.1) again to a sum over single site Hamiltonians and can be written as,

$$H^{MF} = \sum_{i \in A,B,C} H_i^{MF}$$

where,

$$H_i^{MF} = \frac{U}{2}\hat{n}_i(\hat{n}_i - 1) - \mu_i \hat{n}_i - \phi_i(b_i + b_i^\dagger) + \psi_i \phi_i + V(\hat{n}_i \bar{\rho}_i - \rho_i \bar{\rho}_i) \qquad (4.3)$$

where $\psi_i = \langle b_i^\dagger \rangle = \langle b_i \rangle$ represents the superfluid order parameter, vanishing of which, as usual, marks the onset of an insulating phase. Also $\rho_i = \langle \hat{n}_i \rangle$ is the local density and the order parameter averaged over z neighbours, $\phi_i = \frac{1}{z}\sum_{j=1}^{z} \psi_j$, $\bar{\rho}_i = \frac{1}{z}\sum_{j=1}^{z} \rho_j$, z being the coordination number. Here as the boson numbers are conserved, ψ_i and ϕ_i are real. It may be mentioned here that U and μ are in units of zt, while V is in unit of t which, as all preceding discussions, is set as unity.

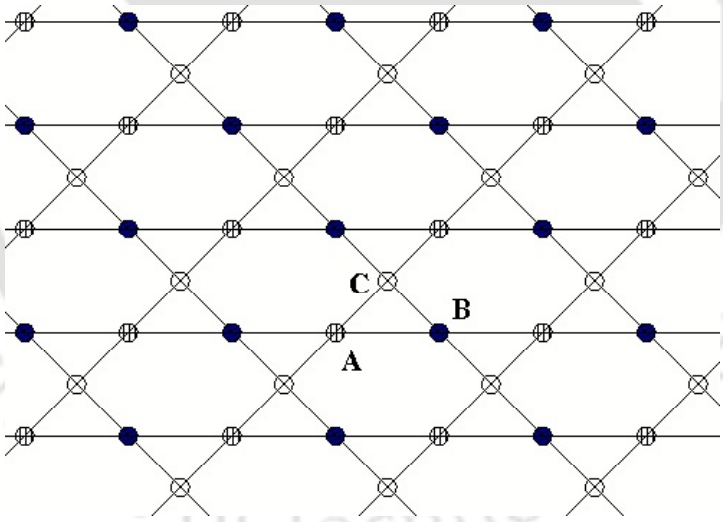

Figure 4.1: The figure shows the schematic diagram of three sublattice structure where the three different sublattices indicated by a striped circle (A sublattice), filled circle (B sublattice) and an unfilled circle (C sublattice). It may be noted that the nearest neighbours of each of these points belong to the other two.

In case of a tripartite lattice, the entire system can be divided into three sublattices, say, A, B and C as shown in Fig. 4.1. Each site of the three sublattice structure has four nearest neighbours consisting of two sites each of the other two types. To make our notations clear, we present table 4.1 containing definitions of various ψ's and ρ's for three different sublattices. Now the Hamiltonian in Eq. (4.3)

i belongs to sublattice	ψ_i	ϕ_i	ρ_i	$\bar{\rho}_i$
A	ψ_A	$\frac{1}{2}(\psi_B+\psi_C)$	ρ_A	$\frac{1}{2}(\rho_B+\rho_C)$
B	ψ_B	$\frac{1}{2}(\psi_C+\psi_A)$	ρ_B	$\frac{1}{2}(\rho_C+\rho_A)$
C	ψ_C	$\frac{1}{2}(\psi_A+\psi_B)$	ρ_B	$\frac{1}{2}(\rho_A+\rho_B)$

Table 4.1: The table represents the definition of various order parameters, ψ_i, ϕ_i, ρ_i, $\bar{\rho}_i$ for three sublattices. See text for details.

can be written as a sum of three terms as in the following,

$$H_i^{MF} \equiv \sum_{j\in A,\ B,\ C} H_j^{MF} \tag{4.4}$$

where each of the H_j^{MF} corresponding to the three sublattices can be written as,

$$\begin{aligned} H_A^{MF} &= \frac{U}{2}\hat{n}_A(\hat{n}_A-1)-\mu_A\hat{n}_A-\frac{1}{2}(\psi_B+\psi_C)(b_A+b_A^\dagger)+\frac{1}{2}\psi_A(\psi_B+\psi_C) \\ &+ \frac{1}{2}V(\rho_B+\rho_C)(\hat{n}_A-\rho_A) \qquad (4.5) \\ H_B^{MF} &= \frac{U}{2}\hat{n}_B(\hat{n}_B-1)-\mu_B\hat{n}_B-\frac{1}{2}(\psi_C+\psi_A)(b_B+b_B^\dagger)+\frac{1}{2}\psi_B(\psi_C+\psi_A) \\ &+ \frac{1}{2}V(\rho_C+\rho_A)(\hat{n}_B-\rho_B) \qquad (4.6) \\ H_C^{MF} &= \frac{U}{2}\hat{n}_C(\hat{n}_C-1)-\mu_C\hat{n}_C-\frac{1}{2}(\psi_A+\psi_B)(b_C+b_C^\dagger)+\frac{1}{2}\psi_C(\psi_A+\psi_B) \\ &+ \frac{1}{2}V(\rho_A+\rho_B)(\hat{n}_C-\rho_C). \qquad (4.7) \end{aligned}$$

In a compact notation, they are represented by,

$$\begin{aligned} H_j^{MF} \equiv \tfrac{U}{2}\hat{n}_j(\hat{n}_j-1)-\mu_j\hat{n}_j-\tfrac{1}{2}(\psi_k+\psi_l)(b_j+b_j^\dagger)+\tfrac{1}{2}\psi_j(\psi_k+\psi_l) \\ +\tfrac{1}{2}V(\rho_k+\rho_l)(\hat{n}_j-\rho_j) \qquad (4.8) \end{aligned}$$

where k and l are neighbours of j. That is, if $j \in A$ sublattice, k and l will belong to B and C sublattices (see Fig. 4.1) and so on. To obtain the mean field phase diagram, we solve Eq. (4.4) for ψ_i and ρ_i selfconsistently in the onsite occupation number basis $|n\rangle$, truncated at some number n_{max}. The number n_{max} is chosen such that the ground state energy saturates for this value[70,94]. The different phases of the system can be distinguished based upon the values of the order parameters, namely ψ_A, ψ_B and ψ_C and the occupancies, ρ_A, ρ_B and ρ_C as discussed later.

Ground state of the system	$(\rho_A,\rho_B,\rho_C,)$	Range of μ
Vacuum	$(0,0,0)$	$\mu \leq 0$
DW $(\frac{1}{3})$	$(0,0,1)$	$0 \leq \mu \leq \frac{1}{2}V$
DW $(\frac{2}{3})$	$(0,1,1)$	$\frac{1}{2}V \leq \mu \leq V$
MI (1)	$(1,1,1)$	$V \leq \mu \leq U+V$
DW $(\frac{4}{3})$	$(1,1,2)$	$U+V \leq \mu \leq U+\frac{3}{2}V$
DW $(\frac{5}{3})$	$(1,2,2)$	$U+\frac{3}{2}V \leq \mu \leq U+2V$
MI (2)	$(2,2,2)$	$U+2V \leq \mu \leq 2U+2V$

Table 4.2: The table contains the range of μ in terms of on-site interaction, U and nearest neighbour exchange V for different incompressible phases. The *'chemical-potential width'* (for definition see text)of the DW and MI phases are $\frac{1}{2}V$ and U respectively.

To get an idea about the position of the different insulating phase boundaries in the $U-\mu$ plane, we analyze the extended Bose Hubbard Hamiltonian in the atomic limit ($\frac{U}{t} \to \infty$). Following the analysis for a bipartite lattice[67,148], we deduce the limiting values of μ that correspond to various insulating phases (*i.e.* $\psi = 0$) as presented in Table 4.2. Thus in the atomic limit, the *'chemical-potential width'*, that is the width along the μ-axis of various DW phases, scales as $\frac{1}{2}V$, while that for the MI phases, it scales as U. The detailed calculations for arriving at the limiting values of μ are presented in Appendix C. The energies corresponding to different ground states are computed in the atomic limit to map out the phase diagram. For example, the energy of the state $n_A = 0$, $n_B = 0$ and $n_C = 1$ (DW($\frac{1}{3}$)) is degenerate with that of the state $n_A = 0$, $n_B = 1$ and $n_C = 1$ (DW($\frac{2}{3}$)), which happens for μ values in the range $[0, \frac{V}{2}]$ and $[\frac{V}{2}, V]$ and corresponding to energies at which $\mu = Un_0 + \frac{1}{2}V(n_0+1)$ and $\mu = Un_0 + V(n_0+1)$ as illustrated in Appendix C. The other ranges for μ and energy can be obtained in a similar manner.

4.2.1 Strong Coupling Perturbation Theory

Now we shall discuss the phase boundary between the superfluid and insulating phases using a second order strong coupling ($\frac{U}{t} \to \infty$) perturbation theory. The effective Hamiltonian can be written as sum of unperturbed Hamiltonian, H^0 and a perturbation term, $H^{'}$ as,

$$H^{eff} = H^0 + \phi H^{'}$$

where

$$H^0 = \frac{U}{2}\hat{n}(\hat{n}-1) - \mu\hat{n} + \psi\phi + V(\hat{n}\bar{\rho} - \rho\bar{\rho})$$
$$H^{'} = -(b + b^{\dagger}). \tag{4.9}$$

Here the site index is skipped for brevity. In Eq. (4.9), the perturbation term is first order in creation and annihilation operators. So in the occupation number basis, the first order correction will vanish, that is $\langle n^{'}|H^{'}|n\rangle = 0$ for all n and $n^{'}$. Thus computing the second order correction in energy, in powers of ϕ around the insulating phase, the (total) ground state energy is obtained as[71] (for derivation, see Appendix D),

$$E_g(\phi) = \frac{U}{2}\rho(\rho-1) - \mu\rho + \psi\phi + \phi^2\left[\frac{\rho}{U(\rho-1)-\mu+V\bar{\rho}} + \frac{\rho+1}{\mu-U\rho-V\bar{\rho}}\right]. \tag{4.10}$$

Following Landau's theory of second order phase transitions, minimizing Eq. (4.10) with respect to ϕ, we obtained the order parameter equation as[148],

$$\psi = 2\phi\left[\frac{\rho+1}{U\rho+V\bar{\rho}-\mu} - \frac{\rho}{U(\rho-1)-\mu+V\bar{\rho}}\right]. \tag{4.11}$$

To obtain the phase boundary between the insulating ($\psi_i \to 0$, $i \in A$, B and C) and compressible phases ($\psi_i \neq 0$) for the tripartite lattice, one can solve Eq. (4.11), which gives three coupled equations for the order parameters ψ_A, ψ_B and ψ_C. The condition that those equations have a unique solution is,

$$\left[\frac{\rho_A+1}{U\rho_A+\frac{1}{2}V(\rho_B+\rho_C)-\mu} - \frac{\rho_A}{U(\rho_A-1)-\mu+\frac{1}{2}V(\rho_B+\rho_C)}\right]$$
$$\times\left[\frac{\rho_B+1}{U\rho_B+\frac{1}{2}V(\rho_C+\rho_A)-\mu} - \frac{\rho_B}{U(\rho_B-1)-\mu+\frac{1}{2}V(\rho_C+\rho_A)}\right]$$
$$\times\left[\frac{\rho_C+1}{U\rho_C+\frac{1}{2}V(\rho_A+\rho_B)-\mu} - \frac{\rho_C}{U(\rho_C-1)-\mu+\frac{1}{2}V(\rho_A+\rho_B)}\right] = 1. \tag{4.12}$$

We solve Eq. (4.12) to obtain the boundary between the insulating ($\psi_i = 0$) and compressible ($\psi_i \neq 0$) phases as shown in Fig. 4.2, for various choices of the occupation densities, ρ_A, ρ_B and ρ_C corresponding to the three sites of the tripartite lattice. For the DW ($\frac{1}{3}$) phase, where the density in any one of the sites per trimer is unity, while the other two being zero, e.g. $\rho_A = 0$, $\rho_B = 0$, $\rho_C = 1$; for the DW ($\frac{2}{3}$) phase where the density in two of the sites are unity, while the other one being zero, e.g. $\rho_A = 0, \rho_B = 1, \rho_C = 1$; and for the MI (1) phase $\rho_A = 1, \rho_B = 1, \rho_C = 1$.

The results are checked against a critical value for the onsite bosonic interaction

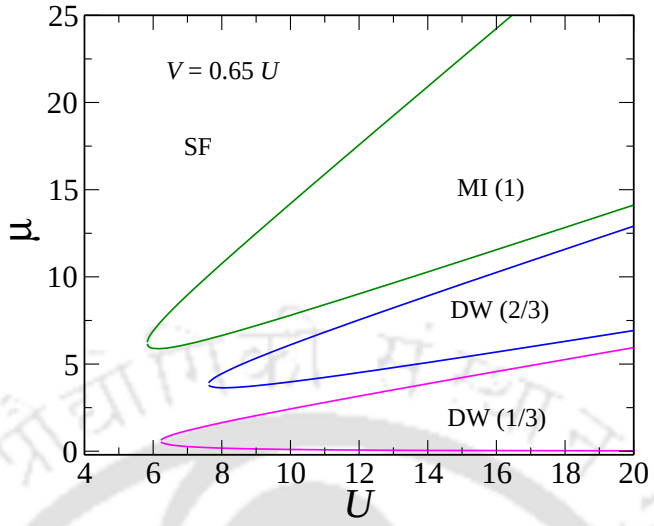

Figure 4.2: The figure shows mean-field phase diagram using second order perturbation theory in the $U-\mu$ plane. The value of nearest neighbour exchange is taken to be $0.65U$.

parameter corresponding to the MI-SF mean field transition which is noted as 5.83, a value well established in literature[70,71]. Here we follow the convention that the number appearing in brackets denotes the occupancy per trimer. Thus we analytically get the insulating lobes corresponding to DW ($\frac{1}{3}$), DW ($\frac{2}{3}$) and MI (1). At low U (basically $U < 5.83$) for all values of μ, superfluid phase prevails.

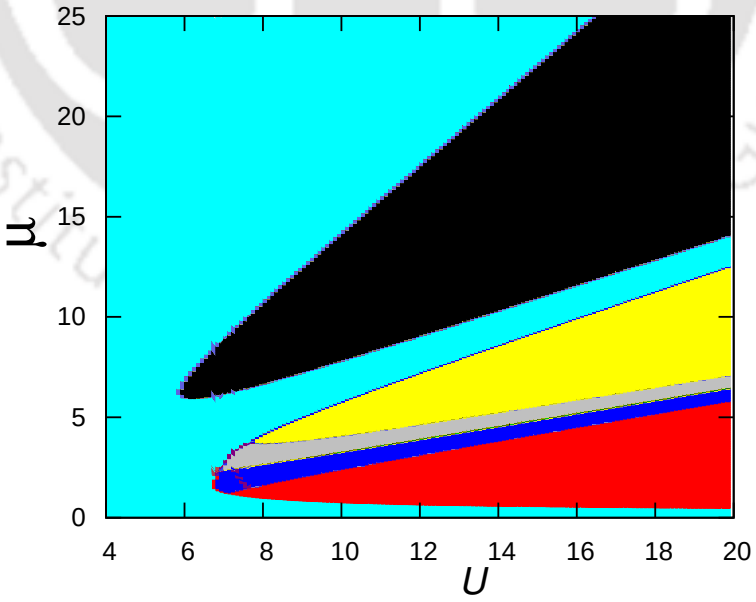

Figure 4.3: The figure shows phase diagram of an extended BHM for a tripartite lattice in the $U-\mu$ plane and for $V = 0.65U$. The colours light blue, red, yellow, blue, gray and black indicate SF, DW ($\frac{1}{3}$), DW ($\frac{2}{3}$), SS type-I, SS type-II and MI respectively.

4.2.2 Numerical Results

To provide support to the above phase diagram, we have solved the equations in Eq. (4.4) selfconsistently for the order parameters, namely of ψ's and ρ's corresponding to the three sublattices. To distinguish between the different phases, we use the condition on the values of the order parameters ψ_A, ψ_B and ψ_C and onsite occupation densities ρ_A, ρ_B and ρ_C as discussed in table 4.3.

Phase	Order parameter	Occupation density
SF	$\psi_A = \psi_B = \psi_C > 0$	$\rho_A = \rho_B = \rho_C > 0$
SS-I	$\psi_A = \psi_B \neq \psi_C > 0$	$\rho_A = \rho_B \neq \rho_C > 0$
SS-II	$\psi_A \neq \psi_B = \psi_C > 0$	$\rho_A \neq \rho_B = \rho_C > 0$
MI	$\psi_A = \psi_B = \psi_C = 0$	$\rho_A = \rho_B = \rho_C = m$ (integer)
DW	$\psi_A = \psi_B = \psi_C = 0$	$\rho_A,\ \rho_B,\ \rho_C$ are integer and two of them differ from the other one

Table 4.3: The table represents the condition on the order parameters ψ_A, ψ_B and ψ_C and occupation densities ρ_A, ρ_B and ρ_C that characterize the different compressible and insulating phases.

However there is a new phase, which is a supersolid (SS) phase that was missed out in our analytic approach. The reason is that we can only address transition from compressible ($\psi_i \neq 0$) to incompressible ($\psi_i = 0$) phases. A transition from a SF ($\psi \neq 0$) to an SS ($\psi \neq 0$) thus remains inaccessible. The SS phase is defined by a nonzero order parameter and unequal densities, at least for one of the three sites in a trimer (see table 4.3).

Fig. 4.3 represents the phase diagram obtained numerically in the $U - \mu$ plane where different phases such as, SF (light blue), DW ($\frac{1}{3}$) (red), DW ($\frac{2}{3}$) (yellow), SS type-I (blue), SS type-II (gray) and MI (black) are shown for a specific value of the nearest neighbour repulsion, V, for example, $V = 0.65U$. We get very good agreement between Figs. 4.2 and 4.3 with regard to the boundaries separating the compressible and incompressible (DW and MI) phases.

In Fig. 4.4 (a) we plot the superfluid order parameters, ψ_A, ψ_B and ψ_C for A, B and C sublattices as a function of μ, keeping $U = 20$ and $V = 0.65U$ fixed. Fig. 4.4(b) shows the variation of occupation densities for the three sublattices again as a function of μ and at same values of U and V as that of in Fig. 4.4 (a). With increasing μ, the variation of the occupation densities, namely, ρ_A, ρ_B and ρ_C yields different phases. The corresponding plots in (a) and (b) are magnified, that is taken

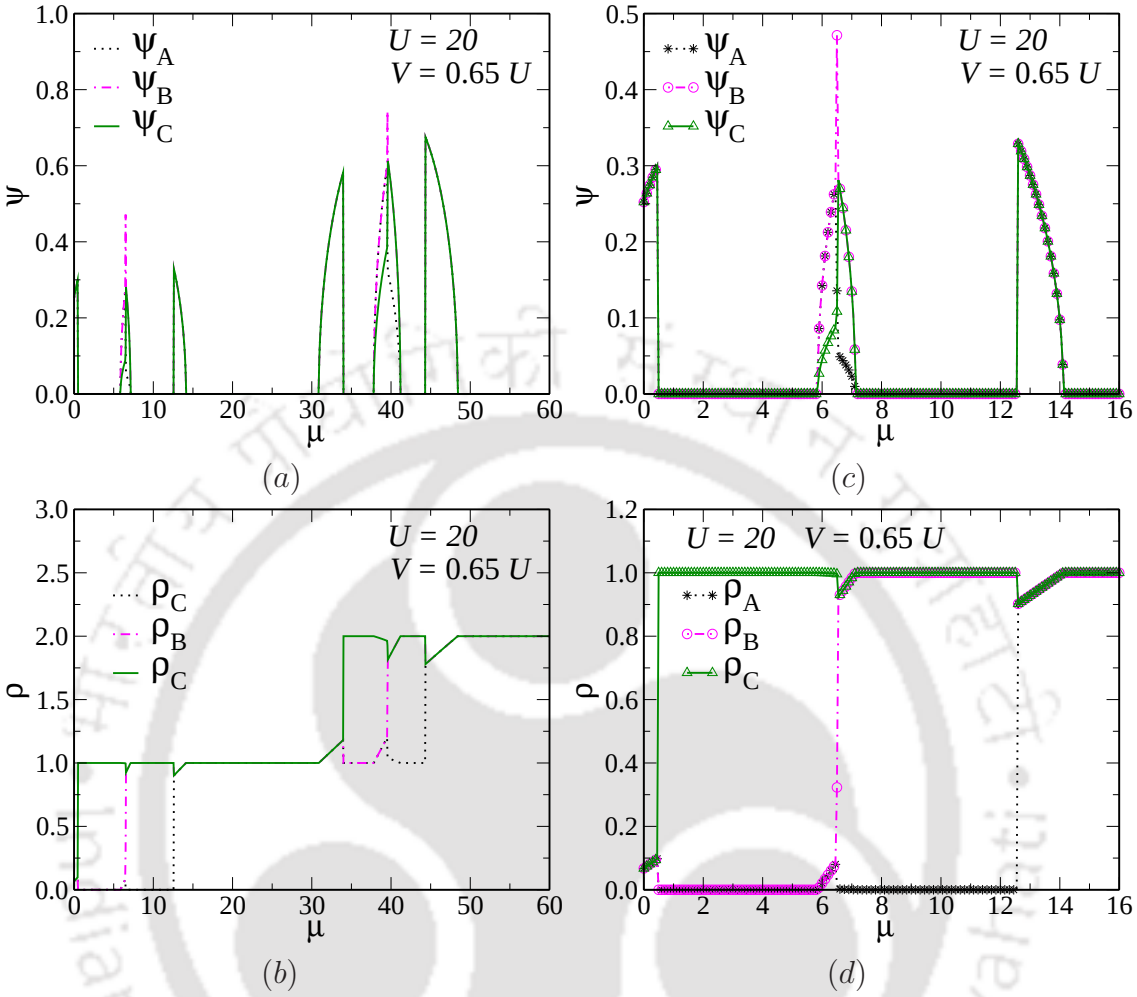

Figure 4.4: The plots show the variation of order parameter ψ_A, ψ_B and ψ_C in (a) and particle densities order ρ_A, ρ_B and ρ_C in (b) as a function of chemical potential μ for $U = 20$ and $V = 0.65U$ respectively. In (c) and (d), we again present magnified plots of ψ and ρ respectively, that is over a small range of μ.

over a smaller range of μ in Fig. 4.4 (c) and (d). In Fig. 4.4 (c) and (d), for $\mu \simeq 0$, all of ψ_A, ψ_B and ψ_c and the densities ρ_A, ρ_B and ρ_C respectively are equal and finite, thus indicating the occurrence of a SF phase. This is followed by a vanishing of all the order parameters and two of the sites having zero occupancy with the rest with unit filling, indicating a DW $(\frac{1}{3})$ phase, which is hence followed by SS type-I with finite with $\psi_A = \psi_B \neq \psi_C$ and similar for the occupation densities. A type-II SS phase follows immediately afterwards with $\psi_A \neq \psi_B = \psi_C$, complemented by a similar behaviour for ρ. A DW $(\frac{2}{3})$ and an MI phase with a thin intervening superfluid region are found to occur afterwards.

We have noted that the widths of the DW lobes at a given value of U (here $U = 20$), denoted by w (for both one-third and two-third fillings) increase as V

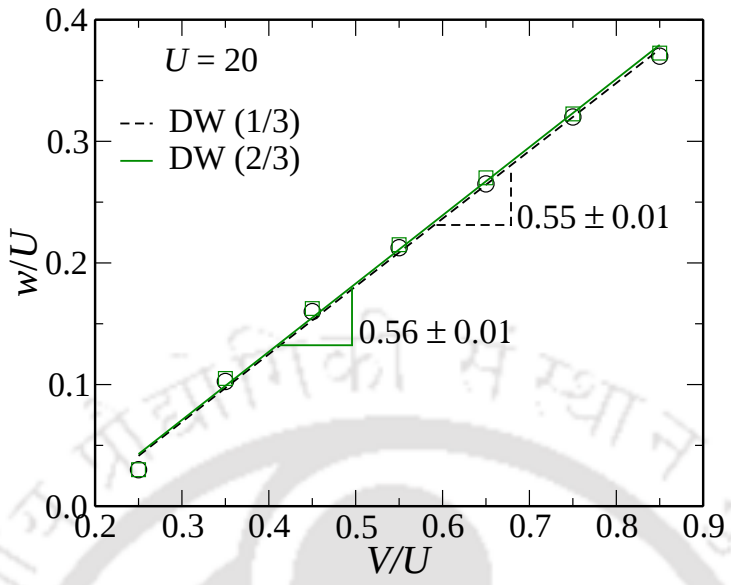

Figure 4.5: The plots show the widths of the DW lobes corresponding to one-third and two-third fillings per trimer as a function of nearest neighbour exchange interaction, V at $U = 20$.

is increased, as shown in Fig. 4.5 which is further accompanied by a change in the position of the MI lobes. It may be noted that the difference in the plots for w corresponding to DW $(\frac{1}{3})$ and DW $(\frac{2}{3})$ phases as a function of V/U is small albeit finite. While it easy to understand that the interaction between the nearest neighbour occupation densities is the origin of density orderings, the effect of V on the extent of the DW lobes in the phase diagram was, to the best of our knowledge, yet to be ascertained. The scaled plot in Fig. 4.5 between w/U and V/U shows nearly a linear relationship with a slope of 0.55. Of course for $V = 0$, the system possesses only SF-MI transition.

4.2.3 Physical Quantities: Compressibility, Structure Factor and Superfluid Stiffness

The compressibility data, with $\kappa = \frac{\partial \bar{\rho}}{\partial \mu}$ where $\bar{\rho}$ is the average density per trimer, that is, $\bar{\rho} = (\rho_A + \rho_B + \rho_C)/3$, as shown in Fig. 4.6, yields interesting behaviour as a function of chemical potential, μ for a given U and V. Instead of periodic humps as in Fig. 5 of Ref.[149], the plots show a series of high and sharp peaks at transitions between different compressible to incompressible (such as SF to DW) phases and also at the transition between SS type-I and SS type-II phases. At small μ ($\mu \simeq 0$) the finite compressibility denotes the presence of the SF phase. The immediate

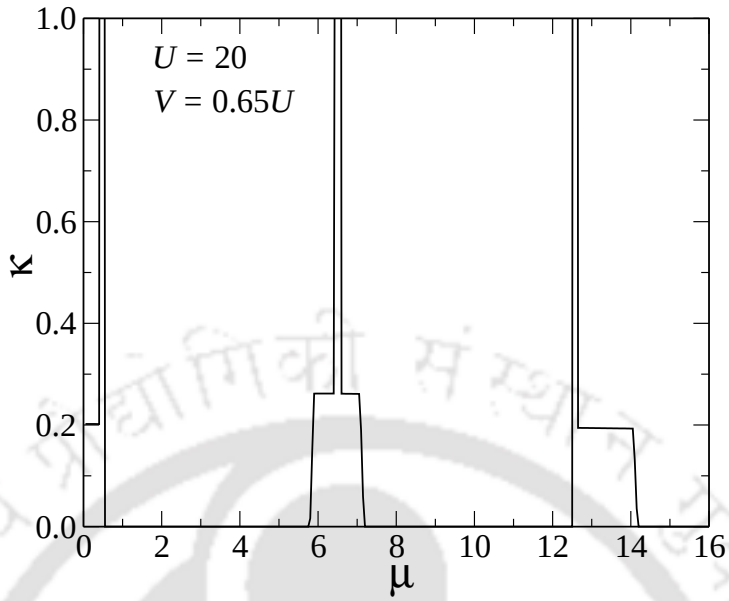

Figure 4.6: The compressibility $\kappa = \frac{\partial \bar{\rho}}{\partial \mu}$ for three sublattices are plotted as a function of chemical potential, μ. The value interaction parameter, U and boson-boson repulsion V is chosen same as that of Fig. 4.4.

jump in κ represents the transition from SF to DW $(\frac{1}{3})$ (see Fig. 4.3). Which is hence followed by a zero κ, signifying the presence of DW $(\frac{1}{3})$ lobe. The SS type-I registers a nonzero value around $\mu = 5.9$, with again a sharp peak signaling a SS type-I to SS type-II transition. The adjoining step like nonzero value of κ denotes SS type-II lobe which is followed by an incompressible DW $(\frac{2}{3})$ phase, and further a sharp peak corresponding to DW $(\frac{2}{3})$-SF transition with a compressible SF phase to follow and so on. It is further interesting to note that the SS phase is marginally more compressible than the SF phase.

To make the distinction between various phases of the system more lucid, we calculate the static structure factor, $S_{\mathbf{q}}$ and superfluid stiffness α_s. The static structure factor at wave vector $\mathbf{q}$ is defined as[24,133],

$$S_{\mathbf{q}} = \frac{1}{N_s} \sum_{j,k} e^{i\mathbf{q}.(\mathbf{r}_j - \mathbf{r}_k)} \langle n_j n_k \rangle \tag{4.13}$$

where N_s is the number of terms in the sum. For a three sublattice structure, in the mean field limit, $S_{\mathbf{q}}$ is given by[133],

$$S_\pi = \frac{1}{12} \left[(\rho_A - \rho_B)^2 + (\rho_B - \rho_C)^2 + (\rho_C - \rho_A)^2 \right] \quad \text{for} \quad \mathbf{q} = (\pi, \pi). \tag{4.14}$$

The superfluid stiffness is defined by[133],

$$\alpha_s = \frac{1}{N_s}\sum_{j,k}\langle b_j^\dagger b_k + h.c.\rangle. \tag{4.15}$$

Again in the mean field limit, for three sublattice basis, α_s reduces to

$$\alpha_s = \frac{1}{6}\left[(\psi_A+\psi_B)^2 + (\psi_B+\psi_C)^2 + (\psi_C+\psi_A)^2\right]. \tag{4.16}$$

S_π is finite in the DW phase and the two types of SS phases, while it should vanish in the SF and MI phases. On the other hand the α_s is nonzero in the compressible phases, such as the SS and SF phases and vanishes in the incompressible phases, such as DW and MI phases. The results for κ, S_π and α_s for different phases are summarized in table 4.4.

Phase	κ	S_π	α_s
SF	$\neq 0$	$= 0$	$\neq 0$
SS-I	$\neq 0$	$\neq 0$	$\neq 0$
SS-II	$\neq 0$	$\neq 0$	$\neq 0$
MI	$= 0$	$= 0$	$= 0$
DW	$= 0$	$\neq 0$	$= 0$

Table 4.4: The table contains the list of phases and the values of various physical quantities such as compressibility, κ, static structure factor, S_π and the superfluid stiffness, α_s for different phases.

A brief comment on the order of the phase transition between various phases can be made as follows. We would like to recall the density profile as given in Fig. 4.4 (d) and the compressibility plot of Fig. 4.6, where the transitions between SF to DW and SS-I to SS-II seem to suggest of a first order transition, as seen form the discontinuity of the density variation as a function of μ and also by a sharp jump in the compressibility. However the transition between SF to MI continues to be second order transition which is evident from the continuous variation of the particle density across the phase boundary (see Fig. 4.4 (d)).

4.3 Conclusions

Thus to conclude, using an analytic strong coupling expansion followed by a numerical solution of the mean field equations for an extended Bose Hubbard model,

we obtained a rich phase diagram for bosons in a tripartite lattice. The different insulating phases (zero superfluid order) are density ordered, DW ($\frac{1}{3}$), DW ($\frac{2}{3}$) and Mott insulating MI (1) phases with the lobes repeating in that order with increased occupancies as the chemical potential is increased. It may be mentioned that such exotic fractional filling (per trimer) phases can very difficult to achieve for crystal lattices, while the creation of optical lattices with tripartite structure (such as a kagome lattice) may be able to capture them. The results are complimented with the behaviour of the order parameters, occupation densities and the compressibility data. Further support to our results have been provided by computing the static structure factor and the superfluid stiffness for various phases.

Chapter 5

Effect of Harmonic Confinement via Inhomogeneous Mean Field Theory

5.1 Introduction

It is useful to remember at this stage of our ongoing discussions that in experiments involving cold atoms, a harmonic trapping potential is usually unavoidable. The trapping potential creates spatial inhomogeneities, thereby compelling the coexistence of the superfluid (SF), Mott insulating (MI) and other kinds of ordered phases, such as density wave (DW) and supersolid (SS) phases. The chemical potential for the inhomogeneous case is renormalized by the trapping potential and varies from one site to another across the lattice, thereby controlling the number of bosons at those sites.

As it is evident from the preceding discussions that we have employed the single site mean field theory in this thesis. A few points in this regard are in order. Despite enjoying success of yielding the correct phase diagram in the parameter space that describes the Hamiltonian, the MFT still remains a one site theory (the environment is replaced by its average) and thus cannot distinguish the symmetry of the lattice potentials that the bosons are subjected to. To state it more lucidly, the phase diagram of the correlated bosons in a two dimensional square lattice will be indistinguishable from that of, say for example, triangular, honeycomb and kagome lattices. The question is especially relevant as optical lattices with a variety of lattice geometries are experimentally realizable[150] that are pristine and simulate the paradigmatic Hamiltonian such as a BHM.

In this chapter we exploit this inhomogeneity in the following way. We write down the EBHM introduced in chapter 4 on a square or a honeycomb (bipartite) and

a kagome (tripartite) lattice in presence of a trapping potential. Hence we correctly identify the neighbours corresponding to a particular lattice site for these geometries. Subsequently a MFT is employed to compute the ground state eigensolutions for a given lattice site selfconsistently in terms of the order parameters. This helps us in identifying different phases and the procedure is repeated for all sites of the lattice. The selfconsistent solution of the order parameters are obtained simultaneously at all sites. It may be noted that in the absence of harmonic potential as was the case in preceding section, it would have sufficed to solve for two sites for a bipartite square or a honeycomb lattice and three sites for a tripartite kagome lattice[94]. The inhomogeneity caused by the trap, compels the necessity to identify the lattice sites distinctly, thereby explicitly invoking the effect of lattice symmetries in the study of the phase diagram.

We organize this chapter as follows. At the onset we sketch a way to build a kagome lattice by keeping track of the coordinates of the lattice points and further labeling them so as to efficiently identify the neighbours. The topological equivalents of the honeycomb and kagome lattices come handy in the context[151,152]. Hence we presents our results for the order parameters that distinguish between the various phases for different choices of the chemical potential, onsite interaction, density exchange interaction, trapping potential etc. We further demonstrate the coexistence of different phases as one navigates away from the center of the trapping potential. The location of the center of the trap may be deliberately chosen to be in either of the SF, MI, DW or SS phases. Hence we present the Fourier transformed superfluid order and density profiles either of which are relevant to the *'time of flight'* experiments[7]. Finally we attempt comparing and contrasting phase diagrams at various sites in the lattice in presence of the confining potential. This has yielded limited success owing to unavailability of selfconsistent solutions or other reasons that are elaborated in the text.

5.2 Extended Bose Hubbard Model with a Harmonic Trapping

The starting point is the writing down the extended Bose-Hubbard Hamiltonian, for the inhomogeneous case as,

$$H = -t\sum_{\langle ij\rangle}(b_i^\dagger b_j + h.c) + V\sum_{\langle ij\rangle}\hat{n}_i\hat{n}_j + \frac{U}{2}\sum_i \hat{n}_i(\hat{n}_i - 1) - \sum_i \mu_i\hat{n}_i \qquad (5.1)$$

where all the symbols have their usual meanings and μ_i is the potential which is now inhomogeneous due to the presence of trapping potential V_T. In the inhomogeneous case that is in presence of confining potential the the onsite chemical potential at site i is

$$\mu_i = \mu - V_T(r_i - r_0)^2 \tag{5.2}$$

where μ is the chemical potential, V_T is the strength of the harmonic confinement, r_i and r_0 are the positions of the lattice site i and that of the trap center respectively.

The conventional MFT was extended for the inhomogeneous case[96]. For a two sublattice system, Eq. (5.1) shows different kind of density ordered phases, such as the SS and DW ordering along with the usual SF and MI phases. The inhomogeneous mean field theory for EBHM with $V_T > 0$ was developed for a two sublattice system in Ref.[94], which shows nonuniform superfluid and density wave order parameters and the system splits into different insulating (DW and MI) and compressible (SF and SS) phases.

In the previous chapter, we have considered a three sublattice structure (a single plaquette of the kagome lattice consisting of three different lattice points belonging to different sublattices) and solved EBHM via mean field theory and obtained a rich phase diagram. When $V_T = 0$, the ground state of model in Eq. (5.1) exhibits SF, density ordered DW ($\frac{1}{3}$) (one site of the plaquette is occupied by one boson, while the other two are empty), SS, DW ($\frac{2}{3}$) (two of them are occupied and one empty), SF and MI (1) (all three sites belonging to different sublattices have unit occupancy for the MI(1) phase) phases, all of which repeat in that fashion with increased occupancies as the chemical potential is increased.

Now the task is to introduce a trapping potential (*i.e.* $V_T > 0$) in a kagome lattice (see Fig. 5.1). The claim is that the inhomogeneity, introduced by external harmonic trapping, is capable of capturing the underlying lattice geometry, details of which will be discussed later.

The decoupling of the kinetic energy and density exchange terms discussed in the previous chapter (Eq. (4.2)) reduces the Hamiltonian in Eq. (5.1) to a sum over single site Hamiltonians which can be solved in the truncated onsite occupation number basis, $|n\rangle$ and can be written as,

$$H^{MF} = \sum_i H_i^{MF}$$

where,

$$H_i^{MF} = \frac{U}{2}\hat{n}_i(\hat{n}_i - 1) - \mu_i\hat{n}_i - \phi_i(b_i + b_i^\dagger) + \psi_i\phi_i + V(\hat{n}_i\bar{\rho}_i - \rho_i\bar{\rho}_i) \qquad (5.3)$$

where $\psi_i = \langle b_i^\dagger \rangle = \langle b_i \rangle$ is the the superfluid order parameter, $\rho_i = \langle \hat{n}_i \rangle$ is the local density and the order parameter, $\phi_i = \frac{1}{z}\sum_{j=1}^{z}\psi_j$, and $\bar{\rho}_i = \frac{1}{z}\sum_{j=1}^{z}\rho_j$, z being the coordination number. The only additional feature of the Hamiltonian in Eq. (5.3) lies in its inhomogeneous chemical potential described by Eq. (5.2).

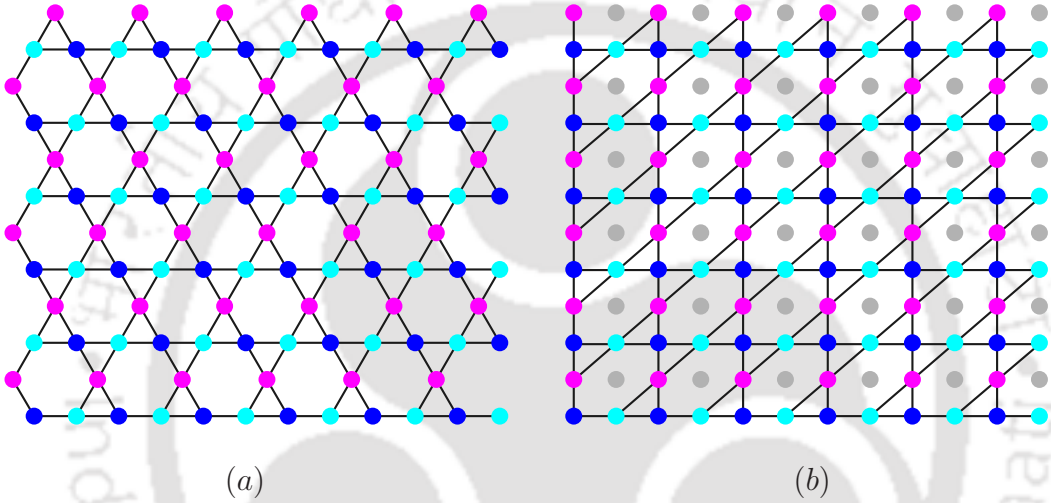

Figure 5.1: The schematic diagram of a kagome lattice (a) and its topological equivalent (b). The three different sublattices of the kagome lattice are indicated by a blue circle (A sublattice), cyan circle (B sublattice) and magenta circle (C sublattice). It may be noted that the nearest neighbours of each of these points belong to the other two sublattices.

5.3 Identifying the Neighbours of a Kagome Lattice

Now we shall discuss how the kagome lattice geometry can be captured in the inhomogeneous ($V_T > 0$) case. The kagome lattice can be considered as a square lattice with some additional adjustments which are emphasized in Fig. 5.1[151]. The equivalent of a kagome lattice can be constructed by connecting the lattice points of a square lattice as shown in Fig. 5.1(b). The points which are at the center of the tilted hexagon are skipped. Thus the lattice points connected by the line in the equivalent lattice correspond to the four neighbours of a kagome lattice, where each site belongs to different sublattices. Thus corresponding to a lattice point belonging to sublattice A (blue circles) in Fig. 5.1(b) has two neighbours belonging to sublattice B (cyan circles) while the other two belong to sublattice C (magenta

circles). The position of the lattice sites for such a kagome lattice can be obtained by translating the basis vectors from any lattice point centered at a chosen origin. Thus for this purpose we use (i, j) indices for each lattice site and identify all the neighbours corresponding to this site as presented in table 5.1.

Condition of i and j	Lattice point	Neighbours
i and j both odd	$\in A$ sublattice	$(i \pm 1, j),\ (i, j \pm 1)$
i odd, j even	$\in B$ sublattice	$(i, j \pm 1),\ (i-1, j-1),$ $(i+1, j+1)$
i even, j odd	$\in C$ sublattice	$(i \pm 1, j),\ (i-1, j-1),$ $(i+1, j+1)$
i and j both even	points do not belong to lattice	no neighbours

Table 5.1: The table represents all the neighbours of a particular site that belongs to different sublattices. For this purpose we choose (i, j) values starting with $(1, 1)$.

5.4 Numerical Results

To obtain the ground state energy and the corresponding wave function, we have computed the matrix elements of ${H_i}^{MF}$ in the occupation number basis $|n_i\rangle$ truncated at some value n_{max} ($= 8$ here) for a set of initial guess values of ψ_i and ρ_i. The ground state solutions are obtained by diagonalizing the Hamiltonian in Eq. (5.3) from the selfconsistent values of ψ_i and ρ_i. We use the conditions on the values of ψ_i and ρ_i so as to distinguish between various phases as present in table 5.2. To obtain the selfconsistent solutions for ψ_i and ρ_i, we exploit the circular symmetry of the trapping potential. This symmetry can be seen in Fig. 5.2 which denotes the surface plot of the onsite chemical potential, μ_i in the plane of the lattice for a particular value of V_T, namely $V_T = 0.0007$. The plot shows the constant energy contours as a function of distance from the center of the trapping potential that are responsible for the emergence of different phases in the form of concentric shells as will be shown later. Here the uniform part of the chemical potential, μ in Eq. (5.2) is chosen as $\mu = 8$. To present the results, we have mostly chosen two representative values of V_T. One of which is $V_T = 0.0007$, where the trapping effect is small and the onsite chemical potential varies slowly form one site to another such that the width of different phases are prominent. The other value is taken as $V_T = 0.0025$, for which μ_i changes over a larger range, thereby demonstrating a variety of phases

as a function of the distance from the trap center. Different other choices of V_T have also been taken into consideration. Apart from affecting the width of the different phases, such as SF, SS, DW etc., there is no other physical significance that has been found which is relevant to the present work and hence the issue is not elaborated further. At the edge of the lattice, with this value of V_T, μ_i becomes negative which yields an empty (zero occupation density) phase. We have explored other values for the strength of the confinement as well, however the discussion on them is not relevant to the present context.

Phase	Order parameter (ψ_i)	Occupation density (ρ_i)	Behaviour of ρ and ψ
SF	$\psi_i > 0$	$\rho_i > 0$	non-oscillatory
SS	$\psi_i > 0$	$\rho_i > 0$	oscillatory
MI	$\psi_i = 0$	$\rho_i = m$ (integer)	non-oscillatory
DW	$\psi_i = 0$	$\rho_i = m$	oscillatory

Table 5.2: The table represents the condition on the order parameters, ψ_i and occupation densities, ρ_i that characterize the different compressible and insulating phases.

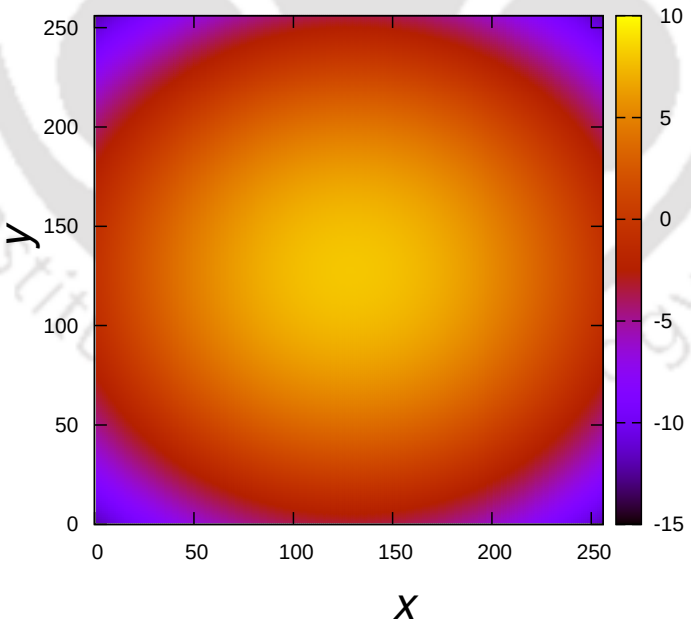

Figure 5.2: The surface plot of onsite chemical potential μ_i (see Eq. (5.2)) in $x-y$ plane for $V_T = 0.0007$ and $\mu = 8$ for a kagome lattice. The μ_i profile shows circular symmetry.

Now we focus on the results that are specific to a kagome lattice. Also we present a few results for square and honeycomb lattices for comparison. In all cases, we have

considered a $L \times L$ ($L = 256$) lattice and keep the trap center (where $\mu = \mu_i$) at the middle of the lattice, *i.e.* at (x, y)=$(L/2, L/2)$. To show the existence of different phases, we present the plots for the order parameter, ψ_i and occupation density, ρ_i as a function of distance from the trap center.

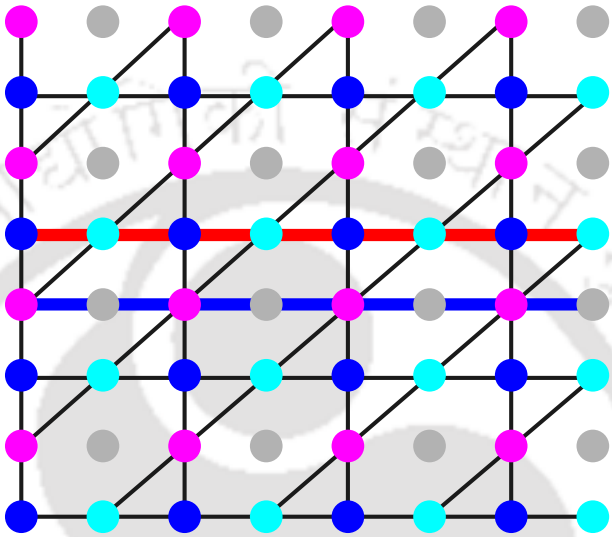

Figure 5.3: The figure shows a $L \times L$ ($L = 8$) lattice that is equivalent to a kagome lattice as illustrated in Fig. 5.1(b). Here the red line corresponds to $y = 1 + L/2$ which visits the lattice points belonging to A-B-A-B.... and blue line corresponds to $y = L/2$ which visits the lattice points belonging to C. It may be noted that it is not possible to visit sites belonging to all three sublattices via a single line.

The plots are presented for a square and a honeycomb lattice along a particular direction in Figs. 5.4(a)-(d). Specifically, we choose the distance along the x-direction (x-axis of our plots) for all our real space order parameter data, where we plot the results corresponding to $y = L/2$, which capture the two sublattices of a bipartite lattice alternately. It may be noted that an equivalent of a honeycomb lattice, known as brick-wall lattice, is used for this purpose[151]. For the convenience of readers, an elaborate discussion of several such lattice geometries and their topological equivalents are discussed in Ref.[151].

The situation is little more tricky in the case of a kagome lattice as in a unidirectional scan as done for the bipartite lattice, it is difficult to capture all the three different sublattices. To circumvent this difficulty, we choose the lines corresponding to $y = 1 + L/2$ (so as to capture the sites belonging to two of the sublattices, say A and B) and $y = L/2$ (belonging to the third sublattice that is C) (see Fig. 5.3). The one dimensional plots presented in Figs. 5.4-5.7.

5.4.1 Phase Diagram

To commence a discussion on the phase diagram, we present our results in the following way. To illustrate the appearance of different phases, we manipulate the values of the parameters (U, μ, V_T, V) such that the trap center falls in either of the SF, MI, DW or SS phase. This will enable a scrutiny of different sequence of phases that one shall encounter while moving away from the trap center and approaching towards the edge of the lattice.

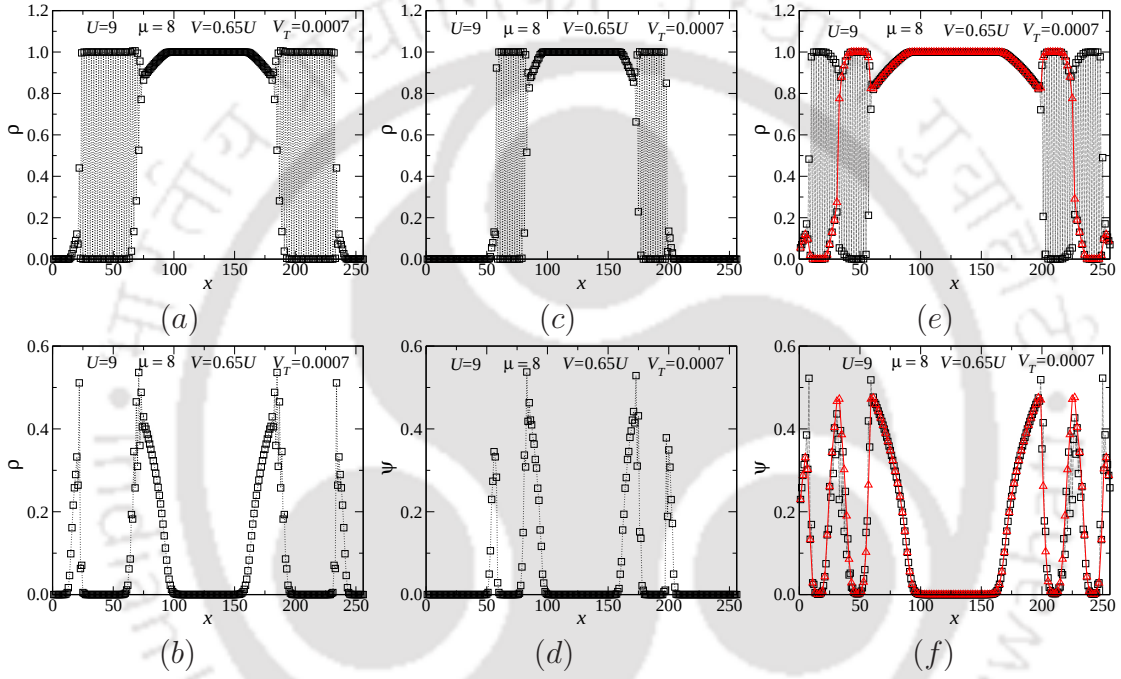

Figure 5.4: The variation of ρ_i in (a) and (c) and ψ_i in (b) and (d) (black dashed line and square symbols) along chosen direction as discussed in text correspond to bipartite lattices, of which (a) and (b) for a square lattice and (c) and (d) for a honeycomb lattice while, in (e) and (f) (black dashed line and square symbols for A and B sublattice and red solid line and triangle symbols for C sublattice) are that for a kagome lattice. In all the cases, we have taken $U = 9$, $\mu = 8$, $V = 0.65U$ and $V_T = 0.0007$ such that the trap center is in MI(1) phase, where the occupation density $\rho_i = 1$ and $\psi_i = 0$ for all sublattices. For the bipartite lattice ((a)-(d)), the sequence of phases are MI(1), SF, SS, DW($\frac{1}{2}$), thin SS, SF and an empty phase as a function of distance from trap center. For a kagome lattice, the sequence is MI(1), SF, thin SS, DW($\frac{2}{3}$), SS DW($\frac{1}{3}$) and SF phase. The lines, symbols and colours used are same as that for Figs. 5.5-5.7.

In Fig. 5.4 we present the ρ_i and ψ_i plots for a kagome lattice where the corresponding plots for a square and a honeycomb lattice are included for comparison. For all the order parameter plots, we use black dashed line and square symbols for bipartite lattices. For the kagome lattice, we use black dashed line and square symbols for A and B sublattice and red solid line and triangle symbols for the C

sublattice . The same colour and symbol convention have been used throughout. For all these cases in Fig. 5.4, the particular values of the parameters are chosen $U = 9$, $\mu = 8$, $V = 0.65U$ and $V_T = 0.0007$. At these parameter values, the trap center is in the MI(1) phase as seen from the plots (*i.e.* $\psi = 0$, $\rho = 1$). As one moves away

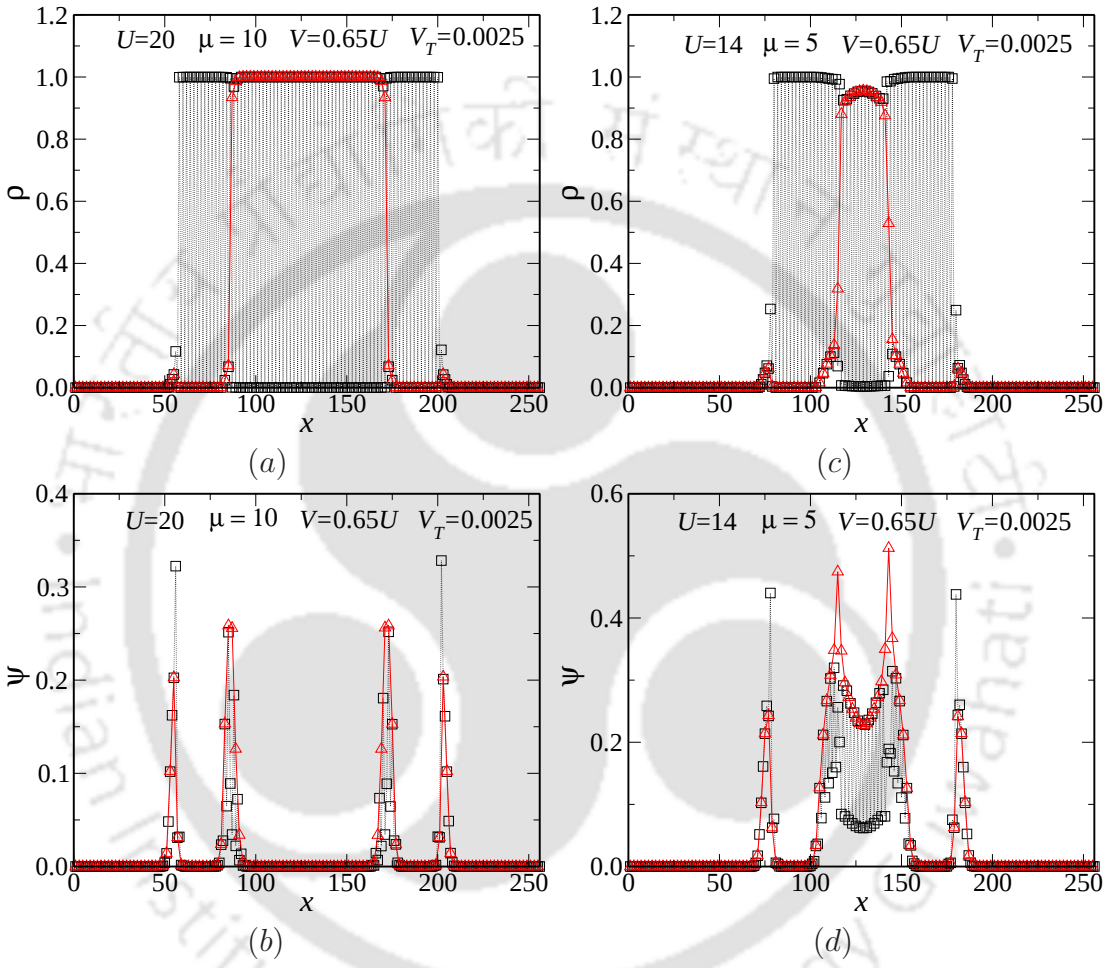

Figure 5.5: The plots show the variation of occupation density order, ρ_i and superfluid order parameter, ψ_i for a kagome lattice along chosen direction as discussed in text. In (a) and (b) the plots correspond to the parameter values, $U = 20$, $\mu = 10$, $V = 0.65U$ and $V_T = 0.0025$, such that the trap center is in the DW($\frac{2}{3}$) phase and the sequence of phases is as DW($\frac{2}{3}$), thin SS, DW($\frac{1}{3}$), thin SS, thin SF and vacuum. In (c) and (d), the plots correspond to the parameter values, $U = 14$, $\mu = 5$, $V = 0.65U$ and $V_T = 0.0025$, the trap center is in the SS phase and the corresponding sequence is SS, DW($\frac{1}{3}$), thin SS, SF and finally a vacuum.

from the trap center, different compressible and insulating phases emerge. In Figs. 5.4(a) and (b), for square lattice, we get MI(1), SF, SS, DW($\frac{1}{2}$), SS and SF phases respectively as a function of the distance from the center of the trap. The phase ordering is identical for a honeycomb lattice, as expected (see Figs. 5.4 (c) and

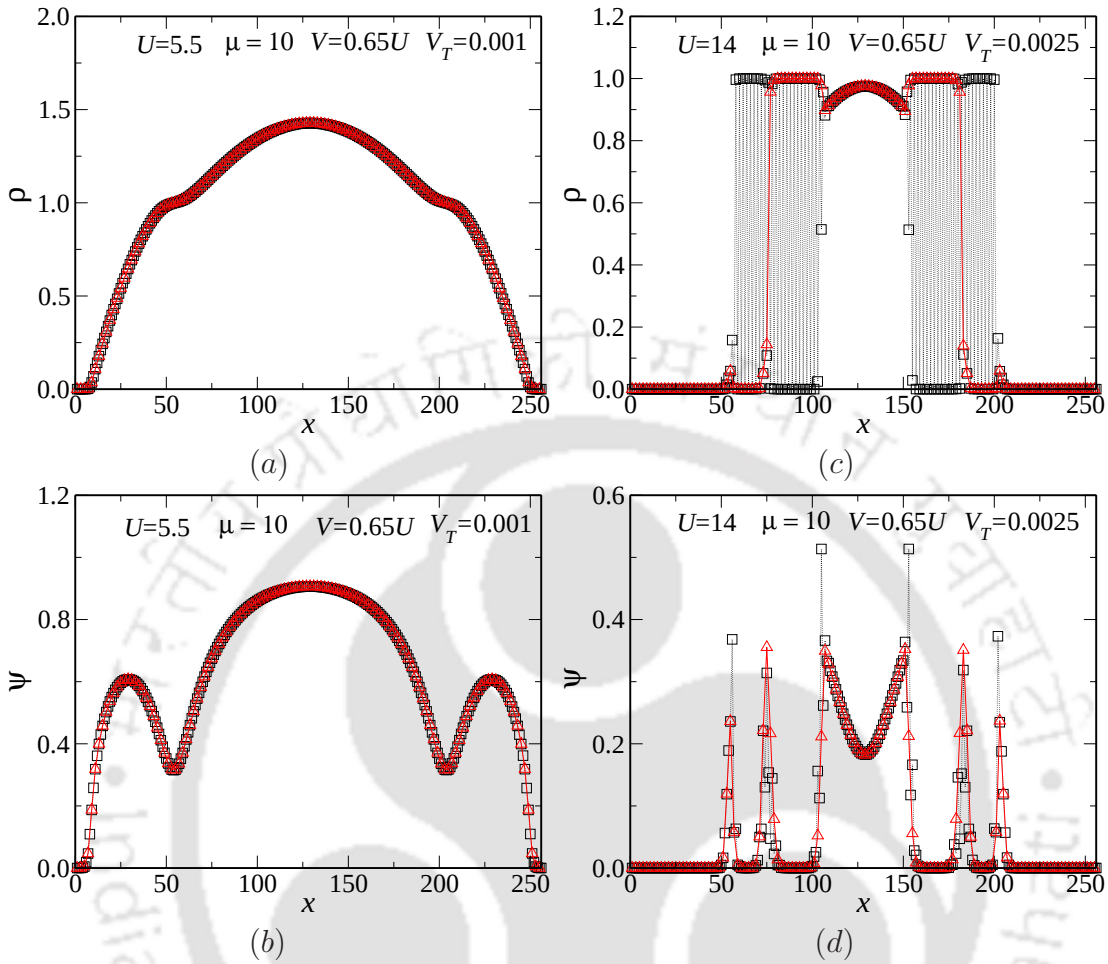

Figure 5.6: The variation of ρ_i and ψ_i for a kagome lattice along a chosen direction as discussed in text. In (a) and (b), the parameter values are chosen as, $U = 5.5$, $\mu = 10$, $V = 0.65U$ and $V_T = 0.001$ where the trap center lies in the SF phase for which almost the entire lattice in in SF phase with a thin vacuum phase at the edges. In (c) and (d) the plots correspond to the parameter values, $U = 14$, $\mu = 10$, $V = 0.65U$ and $V_T = 0.0025$. The trap center here is in the SF phase and the sequence of phases are SF, thin SS, DW($\frac{2}{3}$), SS and DW($\frac{1}{3}$), SS, SF and vacuum.

(d)). In case of the kagome lattice, the emergence of various phases as a function of distance from the trap center (see Figs. 5.4 (e) and (f)) is more interesting. As one move radially outward from trap center, immediately the system starts showing an SF character with uniform values of ψ_i (> 0) and ρ_i (> 0). After this SF phase, there is a very narrow SS region, where both the ρ_i and ψ_i are nonzero and oscillating (as one moves from one lattice point to another). If we move away further, one enters into a DW($\frac{2}{3}$) phase, where $\psi_i = 0$ but ρ_i oscillating between 0 and 1 between two of the sublattices, while the third sublattice stays at $\rho_i = 1$. This phase is hence followed by again an SS phase and hence a DW($\frac{1}{3}$) phase is noted for which $\psi_i = 0$

and ρ_i oscillate between 0 and 1 for two of the sublattices, but it remains at zero for the other sublattice. There is eventually another thin slice of an SS region, which is further followed by an SF phase as one reaches towards the edge of the lattice. Our results for the order parameter and density profiles for a planar bipartite lattice obtained via an inhomogeneous MFT agrees well to those for a cubic lattice[94].

Location of trap center	Parameter values (U, μ, V_T)	Sequence of phases (moving outward from trap center)
MI(1)	$(9, 8, 0.007)$	MI(1), SF, SS, DW($\frac{2}{3}$), SS, DW($\frac{1}{3}$), SS, SF
DW($\frac{2}{3}$)	$(20, 10, 0.0025)$	DW($\frac{2}{3}$), SS, DW($\frac{1}{3}$), SS, SF, Vacuum
SS	$(14, 5, 0.0025)$	SF, DW($\frac{1}{3}$), SS, SF, Vacuum
SF	$(14, 10, 0.0025)$	SF, SS, DW($\frac{2}{3}$), SS, DW($\frac{1}{3}$), SS, SF, Vacuum

Table 5.3: The sequence of phases are listed in the above table for a kagome lattice when the center of the trap is in MI, DW, SS, SF phases. For all the cases, the density exchange interaction is kept as $V = 0.65U$.

Next we discuss a similar scenario of having the trap center in different phases, such as SF, SS, DW etc. by appropriately choosing the system parameters. The aim is to investigate how the evolution of various phases across the lattice in presence of the harmonic trap is affected if the center of the trap is allowed to be in one of the phases. In Figs. 5.5 (a) and (b), the sequence of phases are DW($\frac{2}{3}$), thin SS, DW($\frac{1}{3}$), thin SS, thin SF and vacuum ($\psi_i = 0$ and $\rho_i = 0$) as one traverses away from the trap center (which is in the DW($\frac{2}{3}$) phase) for $U = 20$, $\mu = 10$, $V = 0.65U$ and $V_T = 0.0025$. For the other two plots, 5.5 (c) and (d), we have chosen $U = 14$, $\mu = 5$, $V = 0.65U$ and $V_T = 0.0025$ and the sequence of the phases found corresponding to this case is SS, DW($\frac{1}{3}$), again a thin SS, SF and finally a vacuum ($\rho_i = 0$). For other set of parameter values, we present the same where the sequence are SF and vacuum (in Figs. 5.6 (a) and (b)) for $U = 5.5$, $\mu = 10$, $V = 0.65U$ and $V_T = 0.001$ and SF, thin SS, DW($\frac{2}{3}$), SS, DW($\frac{1}{3}$) , thin SS, thin SF and vacuum (in Figs. 5.6 (c) and (d)) for $U = 14$, $\mu = 10$, $V = 0.65U$ and $V_T = 0.0025$. The above results illustrating different sequence of phases are nicely summarized in table 5.3.

In Fig. 5.7 we present the surface plot of the SF order parameter in the $x - y$ plane (bottom) and the occupation density, ρ as a function of distance from the trap center along the x-direction (top). The various phases are distinguished from the behaviour of ρ and ψ values as mentioned in table 5.2. The sequence of phases observed are MI (1), SF, thin SS, DW($\frac{2}{3}$), SS and DW($\frac{1}{3}$). The purpose of this plot is to correlate the appearance of different insulating and compressible shells with

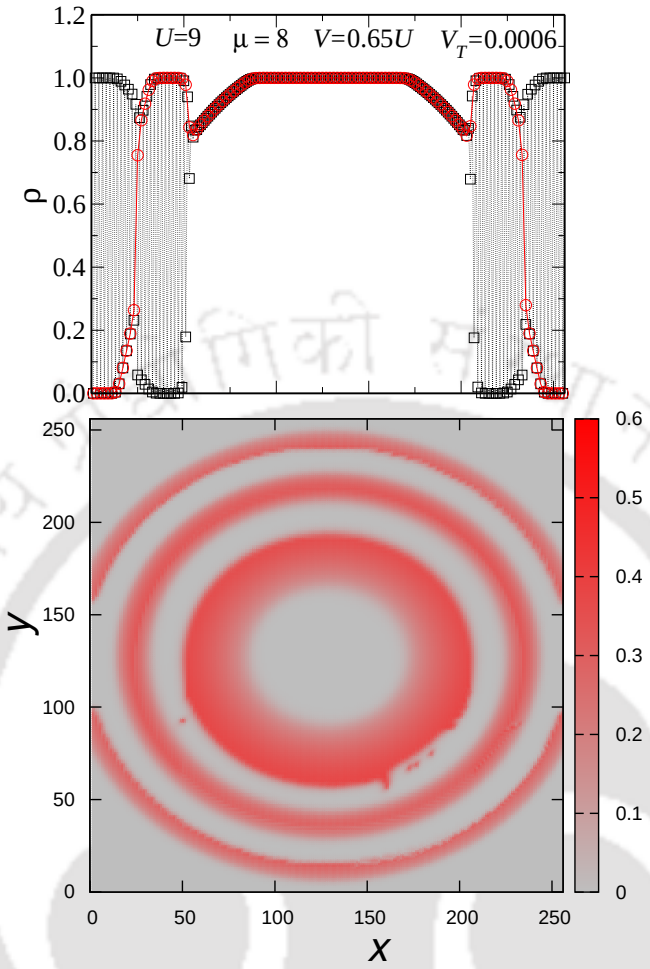

Figure 5.7: Top: The plot shows the real space variation of the occupation density, ρ_i. Bottom: The surface plot for order parameter, ψ in $x-y$ plane. The parameter values are $U = 9$, $\mu = 8$, $V = 0.65U$ and $V_T = 0.0006$. The shells of insulating and compressible phases denote MI (1), SF, thin SS, DW($\frac{2}{3}$), SS and DW($\frac{1}{3}$) etc. as a function of distance from the trap center.

the one dimensional scan of the density profile. The transitions from one phase to another that are seen via the change in occupation densities (see in the top plot) are seen to coincide well with the boundaries of the annular region in the ψ_i plot (bottom).

Having established a distinction between different lattice geometries with regard to the coexistence of various phases we move on to compute some physical quantities. It may be noted that computation of such physical quantities is not trivial owing to the inhomogeneity caused by the trapping potential. Thus the information about these quantities at several locations in the lattice may be a helpful input. Such efforts

by us have not yielded results to our satisfaction, as attainment of selfconsistency for the order parameters at all sites of the lattice poses a considerable difficulty, possibly because of the variation of the chemical potential, μ_i from one site to another. A compromise can be made in the form of computing these quantities at a few locations, wherever possible, still containing the information about the trapping potential and the lattice geometry.

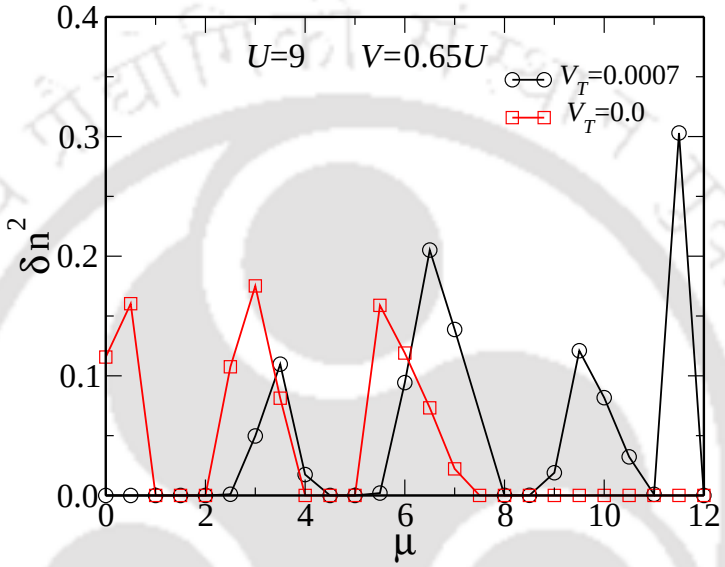

Figure 5.8: The plot shows the variation of square fluctuation, δn^2 (defined in text) as a function of chemical potential, μ for $V_T = 0.0007$ (black line and circle) and $V_T = 0.0$ (red line and square) for $U = 9$, $V = 0.65U$ at a particular location in the lattice given by (x, y)=$(200, 129)$.

5.4.2 Density Fluctuations

Away from the trap center, where the trapping effects are moderate, yet perceivable, we have computed the mean square fluctuation of the occupation density δn^2, a measure of the compressibility of the system[136] which is defined as,

$$\delta n^2 = \langle \hat{n}^2 \rangle - \langle \hat{n} \rangle^2 \tag{5.4}$$

as a function of the chemical potential, μ. In Fig. 5.8, we present δn^2 *vs* μ at the location $(200, 129)$ in the lattice ($(128, 128)$ being the coordinate for the trap center) for a particular V_T, namely $V_T = 0.0007$ (black line and circle). The plot shows that, at this point, as the chemical potential is varied, a series of compressible and insulating phases appear which can be understood by the nonzero values and

vanishing of δn^2 respectively. The effect of the trapping potential on the emergence of the various phases can be demonstrated by switching off the trap ($V_T = 0$) as shown here (red line and square). The phase boundaries are now shifted along the $\mu-$axis and no compressible phase is found for $\mu \geq 8$ which is clearly different than that for $V_T \neq 0$.

5.4.3 Momentum Space Plots

To further distinguish the signature of different phases that emerge in a kagome lattice to those corresponding to, for example, a square lattice, we present the surface plots of the Fourier transformed occupation density, ρ_k. The plots should be relevant to the *'time of flight'* experiments that are performed by releasing the cold gases from an optical lattice *suddenly* and hence after a certain time of flight note down the momentum distribution using standard absorption imaging methods[7,17,153] (see chapter 1). If a single Bloch state, or a particular k-value is macroscopically occupied, such as, the zero momentum state ($k = 0$) of a Bose Einstein condensate, then a series of interference maxima can be observed at each time of flight recording after a specific interval of time. We wish to demonstrate that such data will differentiate between different lattice geometries by demonstrating different phases for the same values of the system parameters. In Figs. 5.9(a)-(d) we present the surface plots of ρ_k and ψ_k in k_x-k_y plane for the kagome lattice and in Figs. 5.9 (e)-(f) for a square lattice for comparison. In Figs. 5.9 (a) and (b), the parameter values are chosen as $U = 5.5$, $\mu = 10$, $V = 0.65U$ and $V_T = 0.001$, such that the entire lattice is in the SF phase (see Figs. 5.6 (a) and (b)) and thus the peaks at $(0, 0)$, $(0, \frac{2\pi}{\sqrt{3}})$, $(\pi, \frac{\pi}{\sqrt{3}})$, $(2\pi, \frac{2\pi}{\sqrt{3}})$ etc. correspond to the SF phase. In Figs. 5.9 (c) and (d), additional peaks are observed at $(0, \pi)$ and $(\pi, \frac{2\pi}{\sqrt{3}})$ for the parameter values, $U = 9$, $\mu = 8$, $V = 0.65U$ and $V_T = 0.0007$. At these values, the system possesses all possible phases such as SF, MI, DW, and SS phase (see ρ and ψ plots in Figs. 5.4(e) and (f)). Hence these additional peaks arise due to the emergence of SS and DW phases. We have included the square lattice for comparison in Figs. 5.9 (e) and (f) where, the parameter values used are same as that of in Figs. 5.9 (c) and (d). The peaks observed for a square lattice at $(0, 0)$, $(0, 2\pi)$, $(2\pi, 0)$ and $(2\pi, 2\pi)$ correspond to SF and MI phases and that at (π, π) is due to SS or DW phases. Thus the positions of various peaks in the k-space are different for square and kagome lattices and thus the plots in Fig. 5.9 substantiate our claim of the ability to capture lattice geometry via an inhomogeneous mean field theory.

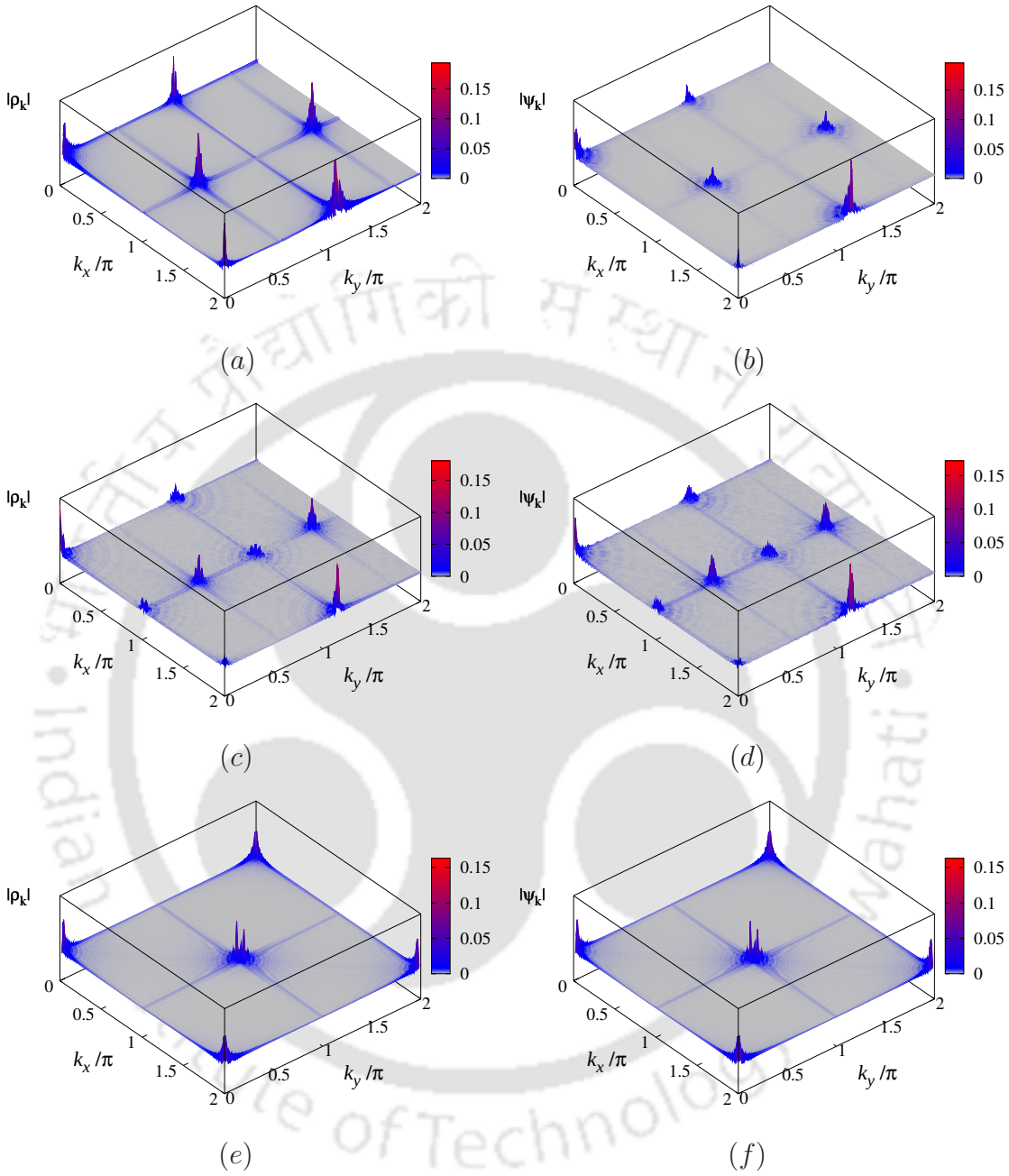

Figure 5.9: The plots show the Fourier transformed occupation density ρ_k and superfluid order ψ_k in $k_x - k_y$ plane. The peaks signify the occurrence of different phases. In Figs. $(a) - (d)$, the plots are presented for a kagome lattice and in Figs. (e) and (f) the plots correspond to a square lattice. In (a) and (b), the parameter values kept at $U = 5.5$, $\mu = 10$, $V = 0.65U$ and $V_T = 0.001$. In (c) and (f), the parameter values are $U = 9$, $\mu = 8$, $V = 0.65U$ and $V_T = 0.0007$. A comparison between (c) and (e) (or (d) and (f) which corresponding to same parameter values but represent kagome and square lattice respectively, shows peaks at different (k_x, k_y) values for the kagome lattice than that for the square lattice.

5.5 Conclusions

To conclude, the drawbacks of a mean field theory lies in the inability to capture the effect of underlying lattice geometry on the physical quantities. In this work, we show that, an extended range (nearest neighbour here) interaction, in conjunction with a harmonic confinement, can yield results that are specific to a particular lattice geometry. Kagome lattice is chosen as a candidate to provide support to our claims as it denotes a complex structure, a non-bipartite lattice and can be achieved by optical means. Detailed studies are carried out to establish a phase diagram that show a variety of compressible and incompressible phases via computing the mean field order parameters. A comparison of the results with familiar bipartite lattices such as square and honeycomb lattices are included. The order parameter computed in $k-$space and having possible relevance to 'time of flight' experiments are presented.

Chapter 6

Multi-Component Mixtures: Emergence of Exotic Phases

6.1 Introduction

Two component quantum fluids, consisting of bosonic atoms, fermionic atoms or Bose Fermi mixtures, exhibit a rich phase diagram that is inaccessible to single component fluids. Among other features, the phase separation observed in $^3He - ^4He$ mixtures[154,155] has initiated a large volume of studies to investigate the behaviour of one quantum fluid in presence of another. The wonderful platform that has evolved in terms of the technical advances in tuning the two body interaction potential via a Feshbach resonance, provides the possibility of arriving at a detailed phase diagram that can comment on the miscibility of the interacting fluids[156]. Several studies have followed since then to address various static and dynamical properties of these two component mixtures[41,157–161].

In the past, experimental studies on condensing different species of atoms focused on the different isotopes of the same atomic species such as ^{85}Rb and ^{87}Rb[162]. Later on different atomic species, such as ^{41}K and ^{87}Rb etc were considered together[156,163]. Photoassociation spectroscopy with different isotopes of Ytterbium atoms was done to determine the s-wave scattering lengths that characterize the two body interaction parameters[164]. A large number of isotopes (seven of them) have been used and a comprehensive database has been created for the scattering lengths which shows the possibilities of attractive interaction either between same species or among different species. Theoretical efforts have also been made to enumerate the stability criteria for both the attractive and repulsive condensates[165]. Importantly, presence of a second component and its role on the stability of the mixture are discussed[62],

which has essentially motivated us to add one more component and study a three component bosonic fluid.

Another reason for us to initiate studies on the phase diagram of three component systems is: two component mixtures have received some, although limited, attention from the theoretical community. Mean field (MF) studies of two component Bose Hubbard model reveals the existence of mixed phases where one specie of atoms can be in a superfluid (SF) phase while the other kind represents a Mott insulating (MI) lobe[166]. Support for the occurrence of such mixed phases are obtained via quantum Monte Carlo simulations where renormalization of the phase boundary of one component is explored in presence of another[62]. A three component mixture thus holds the promise of offering more exotic phases and a versatile phase diagram.

Within the mean field scheme, the atomic interaction strengths are given by, $g_{ij} = 2\pi\hbar^2 a_{ij}/m$[156], where the subscripts i and j denotes different components, a and m being the relevant s-wave scattering lengths and the mass of the atoms respectively. In a two component fluid, the stability of the system is enumerated in terms of a reduced interaction parameter namely $\Delta = g_{12}/\sqrt{g_{11}g_{22}}$[158,161]. Taking a clue from this, we model the existence of different participating species by allowing for different intra and interspecies interaction potentials in the Bose Hubbard model (BHM).

In the present work, we perform MF calculations on a three component BHM and analytically compute the ground state energy using a standard strong coupling perturbation theory with the intersite hopping term as the perturbation[166]. Phase boundaries are evaluated by minimizing the ground state energy fluctuation with regard to the order parameter for each of the species of bosons. A number of cases relevant to the experimental scenario for multi-component systems, such as different interspecies and intraspecies, attractive and repulsive parameters have been considered and explored situations which advocate the existence of mixed phases, for example, one specie in the superfluid phase and the other two may denote insulating phases. Finally we have computed the phase diagram numerically via a selfconsistent solution of the mean field equations.

We organize this chapter as follows. The next section introduces the mean field Hamiltonian for three species of bosons. The third section deals with the strong coupling perturbation theory on a three component BHM and an analytic evaluation of the MF phase diagram for a three component bosonic mixture. In section 6.4 we study the fully selfconsistent numerical solutions of the mean field equations to obtain the phase diagram and compare those with the phase diagram obtained using

analytic technique that are obtained in section 6.3. The corresponding results are presented in section 6.5. Some of the insulating Mott lobes consisting fractional densities for each of the components, while the total density for all the components put together summed up to an integer, are seen to emerge that are missed in our analytic work. We conclude the chapter with a mention of the relevance of the present work with the experimental scenario and the highlights of our work.

6.2 BHM for a Three Component Mixture

For a system of three component bosons, we start with the Bose Hubbard Hamiltonian explicitly written for three components namely A, B and C as in the following,

$$\begin{aligned} H = & - \sum_{\langle ij \rangle} \left[t_A (b_{iA}^\dagger b_{jA} + h.c.) + t_B (b_{iB}^\dagger b_{jB} + h.c.) + t_C (b_{iC}^\dagger b_{jC} + h.c.) \right] \\ & + \sum_i \left[\frac{U_A}{2} \sum_i \hat{n}_{iA}(\hat{n}_{iA} - 1) + \frac{U_B}{2} \hat{n}_{iB}(\hat{n}_{iB} - 1) + \frac{U_C}{2} \hat{n}_{iC}(\hat{n}_{iC} - 1) \right] \\ & + \sum_i (U_{AB} \hat{n}_{iA} \hat{n}_{iB} + U_{BC} \hat{n}_{iB} \hat{n}_{iC} + U_{AC} \hat{n}_{iA} \hat{n}_{iC}) \\ & - \sum_i (\mu_{iA} \hat{n}_{iA} + \mu_{iB} \hat{n}_{iB} + \mu_{iC} \hat{n}_{iC}) \end{aligned} \tag{6.1}$$

where $b_{i\alpha}^\dagger (b_{i\alpha})$ creates (annihilates) a particle at site i for α-specie ($\alpha \in A, B, C$) of bosons and $\hat{n}_{i\alpha} = b_{i\alpha}^\dagger b_{i\alpha}$ is the boson number operator for the bosons of type α. t_α being the nearest neighbour hopping amplitude, and U_α, denote the onsite interspecies repulsion for A, B and C species respectively. The mutual interaction, $U_{\alpha\beta}$ between the different species are taken as U_{AB}, U_{BC} and U_{AC} and respective the onsite chemical potentials are μ_A, μ_B and μ_C, that control the bosons density for the three species. For simplicity, we set the hopping amplitudes for different species as same that is $t_A = t_B = t_C = t$.

To solve Eq. (6.1), we use the standard mean field theory to arrive at

$$H^{MF} = \sum_i H_i^{MF}$$

where H_i^{MF} is the single site, mean field Hamiltonian scaled by an energy zt, (z

being the coordination number) and is given by

$$\begin{aligned} H_i^{MF} &= \frac{1}{zt}\sum_i \left[\frac{U_A}{2}\hat{n}_{iA}(\hat{n}_{iA}-1)+\frac{U_B}{2}\hat{n}_{iB}(\hat{n}_{iB}-1)+\frac{U_C}{2}\hat{n}_{iC}(\hat{n}_{iC}-1)\right] \\ &+ \frac{1}{zt}\sum_i (U_{AB}\hat{n}_{iA}\hat{n}_{iB}+U_{BC}\hat{n}_{iB}\hat{n}_{iC}+U_{AC}\hat{n}_{iA}\hat{n}_{iC}) \\ &- \frac{1}{zt}\sum_i (\mu_{iA}\hat{n}_{iA}+\mu_{iB}\hat{n}_{iB}+\mu_{iC}\hat{n}_{iC}) - (\phi_{iA}b_{iA}^\dagger+\phi_{iB}b_{iB}^\dagger+\phi_{iC}b_{iC}^\dagger+h.c.) \\ &+ \psi_{iA}^*\phi_{iA}+\psi_{iB}^*\phi_{iB}+\psi_{iC}^*\phi_{iC}. \end{aligned} \tag{6.2}$$

Here $\psi_{i\alpha}=\langle b_{i\alpha}\rangle=\langle b_{i\alpha}^\dagger\rangle$ and $\phi_{i\alpha}=\frac{1}{z}\sum_j \psi_{j\alpha}$, j stand for neighbours of site i for the α component. In the case of a homogeneous lattice we can set, $\mu_{iA}=\mu_A$, $\mu_{iB}=\mu_B$ and $\mu_{iC}=\mu_C$. Also $\phi_{iA}=\psi_{iA}=\psi_A$, $\phi_{iB}=\psi_{iB}=\psi_B$ and $\phi_{iC}=\psi_{iC}=\psi_C$ are independent of the site index, i. Incorporating such simplifications, the resulting mean field Hamiltonian for the three species of bosons can be written as,

$$\begin{aligned} H^{MF} &= \left[\frac{U_A}{2}\hat{n}_A(\hat{n}_A-1)+\frac{U_B}{2}\hat{n}_B(\hat{n}_B-1)+\frac{U_C}{2}\hat{n}_C(\hat{n}_C-1)\right] \\ &+ (U_{AB}\hat{n}_A\hat{n}_B+U_{BC}\hat{n}_B\hat{n}_C+U_{AC}\hat{n}_A\hat{n}_C)-(\mu_A\hat{n}_A+\mu_B\hat{n}_B+\mu_C\hat{n}_C) \\ &- (\psi_A b_A^\dagger+\psi_B b_B^\dagger+\psi_C b_C^\dagger+h.c.)+(\psi_A^2+\psi_B^2+\psi_C^2). \end{aligned} \tag{6.3}$$

Here all the interaction parameters and chemical potentials of the system are scaled by the energy zt. This implies that, for example $\frac{U_\alpha}{zt}$ ($\frac{\mu_\alpha}{zt}$) has been set as U_α (μ_α) in the above equation and so on.

6.3 Strong Coupling Expansion

In the strong coupling limit ($\frac{U}{t}\to\infty$), the hopping term can be taken as perturbation and the Hamiltonian in Eq. (6.3) can be written as a sum of unperturbed Hamiltonian and a perturbation term as,

$$H^{MF}=H^0+H'$$

where H^0 and H' are given by,

$$\begin{aligned} H^0 &= \frac{U_A}{2}\hat{n}_A(\hat{n}_A-1)+\frac{U_B}{2}\hat{n}_B(\hat{n}_B-1)+\frac{U_C}{2}\hat{n}_C(\hat{n}_C-1) \\ &+ (U_{AB}\hat{n}_A\hat{n}_B+U_{BC}\hat{n}_B\hat{n}_C+U_{AC}\hat{n}_A\hat{n}_C)-(\mu_A\hat{n}_A+\mu_B\hat{n}_B+\mu_C\hat{n}_C) \end{aligned} \tag{6.4}$$

and

$$\begin{aligned} H' &= -\big[\psi_A(b_A^\dagger + b_A) + \psi_B(b_B^\dagger + b_B) + \psi_C(b_C^\dagger + b_C)\big] \\ &+ (\psi_A^2 + \psi_B^2 + \psi_C^2). \end{aligned} \tag{6.5}$$

To find the ground state, we calculate the energy of the unperturbed Hamiltonian in Eq. (6.4) by choosing the basis formed by the occupation numbers corresponding to the three species, namely $|n\rangle = |n_A\rangle \otimes |n_B\rangle \otimes |n_c\rangle = |n_A, n_B, n_C\rangle$. The MF ground state wave function in the above basis can be written as[166],

$$|\Psi_0\rangle = \prod_n (b_A^\dagger)^{n_A} (b_B^\dagger)^{n_B} (b_C^\dagger)^{n_C} |0\rangle. \tag{6.6}$$

The ground state energy of the system can be calculated by minimizing the energy function $E_n^{(0)}(n_A, n_B, n_C)$, the latter of which is computed from Eq. (6.4) as,

$$\begin{aligned} E_n^{(0)}(n_A, n_B, n_C) &= \frac{1}{2}\big[U_A n_A(n_A - 1) + U_B n_B(n_B - 1) + U_C n_C(n_C - 1) \\ &+ 2(U_{AB} n_A n_B + U_{BC} n_B n_C + U_{AC} n_A n_C)\big] \\ &- (\mu_A n_A + \mu_B n_B + \mu_C n_C). \end{aligned} \tag{6.7}$$

First we consider the fact that the occupation numbers n_A, n_B and n_C all are integers, then the minimization conditions for the above energy functional are given by,

$$\begin{aligned} U_A n_A + U_{AB} n_B + U_{AC} n_C &= \mu_A + \tfrac{U_A}{2} \\ U_B n_B + U_{AB} n_A + U_{BC} n_C &= \mu_B + \tfrac{U_B}{2} \\ U_C n_C + U_{AC} n_A + U_{BC} n_B &= \mu_C + \tfrac{U_C}{2}. \end{aligned} \tag{6.8}$$

The solutions for n_A, n_B and n_C can be obtained by solving the three coupled linear equations in Eq. (6.8) and is given by

$$n_A = \frac{\tilde{\mathrm{n}}_A}{D}, \;\; n_B = \frac{\tilde{\mathrm{n}}_B}{D} \;\; \text{and} \;\; n_C = \frac{\tilde{\mathrm{n}}_C}{D} \tag{6.9}$$

where,

$$\tilde{\mathrm{n}}_A = 2U_{AB}U_C\mu_B + U_{BC}^2(U_A + 2\mu_A) + U_B(U_{AB}U_C - U_AU_C + U_{AC}U_C - 2\mu_AU_C + 2U_{AC}\mu_C) - U_{BC}(U_BU_{AC} + 2U_{AC}\mu_B + U_{AB}(U_C + 2\mu_C)),$$

$$\tilde{\mathrm{n}}_B = 2U_{BC}U_A\mu_C + U_{AC}^2(U_B + 2\mu_B) + U_C(U_{BC}U_A - U_AU_B + U_{AB}U_A - 2\mu_BU_A + 2U_{AB}\mu_A) - U_{AC}(U_CU_{AB} + 2U_{AB}\mu_C + U_{BC}(U_A + 2\mu_A)),$$

$$\tilde{\mathrm{n}}_C = 2U_{AC}U_B\mu_A + U_{AB}^2(U_C + 2\mu_C) + U_A(U_{AC}U_B - U_BU_C + U_{BC}U_B - 2\mu_CU_B + 2U_{BC}\mu_B) - U_{AB}(U_AU_{BC} + 2U_{BC}\mu_A + U_{AC}(U_B + 2\mu_B))$$

and

$$D = 2(U_{AB}^2U_C + U_{BC}^2U_A + U_{AC}^2U_B - 2U_{AB}U_{BC}U_{AC} - U_AU_BU_C)$$

Owing to the fact that the occupation numbers may not be only integers (for example, as in the superfluid phase for all the three components the occupation numbers are fractions), we choose three closest integers n_A^0, n_B^0 and n_C^0 corresponding to the values of n_A, n_B and n_C respectively in Eq. 6.9. Thus we can write the occupation number for three species in terms of closest integers as,

$$n_A = n_A^0 + \beta, \;\; n_B = n_B^0 + \gamma \;\; \text{and} \;\; n_C = n_C^0 + \delta \tag{6.10}$$

where the fractional parts β, γ and δ satisfy the relations are given by,

$$\begin{aligned} -\frac{1}{2} < \beta = n_A - n_A^0 < \frac{1}{2} \\ -\frac{1}{2} < \gamma = n_B - n_B^0 < \frac{1}{2} \\ -\frac{1}{2} < \delta = n_C - n_C^0 < \frac{1}{2}. \end{aligned} \tag{6.11}$$

Thus for the actual minimization of the ground state energy $E_n^{(0)}(n_A, n_B, n_C)$ corresponding to the occupation numbers n_A^0, n_B^0 and n_C^0, the Hamiltonian parameters satisfy the following conditions:

$$n_A^0 - 1 < \frac{\tilde{\mathrm{n}}_A}{D} - \frac{1}{2} < n_A^0 \tag{6.12}$$

$$n_B^0 - 1 < \frac{\tilde{\mathrm{n}}_B}{D} - \frac{1}{2} < n_B^0 \tag{6.13}$$

$$n_C^0 - 1 < \frac{\tilde{\mathrm{n}}_C}{D} - \frac{1}{2} < n_C^0. \tag{6.14}$$

Let us go back to the discussion of the perturbation technique. The first order correction to the energy due to the first term in the perturbation Hamiltonian, $H^{'}$ (see Eq. (6.5)) is zero, since it contain linear terms in the bosonic operator and the ground state is the product of states in the occupation number basis. Thus the first order correction only gives the constant energy shift by an amount $E_g^{(1)} = \psi_A^2 + \psi_B^2 + \psi_C^2$ (see Eq. (6.5)). Hence the second order correction to the free energy can be calculated using,

$$E_g^{(2)} = \sum_{n \neq g} \frac{|\langle g|H^{'}|n\rangle|^2}{E_g^{(0)} - E_n^{(0)}}$$

where $E_g^{(0)}(n_A^0, n_B^0, n_C^0)$ is the ground state energy of the unperturbed Hamiltonian and n_A^0, n_B^0 and n_C^0 are the occupation numbers corresponding to the ground state, $|g\rangle = |n_A^0, n_B^0, n_C^0\rangle$. Thus the total ground state energy including this correction is given by,

$$\begin{aligned} E_g^{(0)} + E_g^{(1)} + E_g^{(2)} &= E_g^{(0)} + \psi_A^2 + \psi_B^2 + \psi_C^2 \\ &+ \psi_A^2 \left[\frac{n_A^0}{-\mu_A + U_A(n_A^0 - 1) + U_{AB} n_B^0 + U_{AC} n_C^0} + \frac{n_A^0 + 1}{\mu_A - U_A n_A^0 - U_{AB} n_B^0 - U_{AC} n_C^0} \right] \\ &+ \psi_B^2 \left[\frac{n_B^0}{-\mu_B + U_B(n_B^0 - 1) + U_{AB} n_A^0 + U_{BC} n_C^0} + \frac{n_B^0 + 1}{\mu_B - U_B n_A^0 - U_{AB} n_A^0 - U_{BC} n_C^0} \right] \\ &+ \psi_C^2 \left[\frac{n_C^0}{-\mu_C + U_C(n_C^0 - 1) + U_{AC} n_A^0 + U_{BC} n_B^0} + \frac{n_C^0 + 1}{\mu_C - U_C n_C^0 - U_{BC} n_B^0 - U_{AC} n_A^0} \right]. \end{aligned} \tag{6.15}$$

To obtain the phase boundary between the SF and MI phases, we minimize the total ground state energy, $E_g^{(0)} + E_g^{(1)} + E_g^{(2)}$ with respect to the three order parameters ψ_A, ψ_B, and ψ_C corresponding to the three bosonic species respectively[71,148,166]. The minimization condition yields three coupled equations that are given by,

$$1 + \left[\frac{n_A^0}{-\mu_A + U_A(n_A^0 - 1) + U_{AB} n_B^0 + U_{AC} n_C^0} + \frac{n_A^0 + 1}{\mu_A - U_A n_A^0 - U_{AB} n_B^0 - U_{AC} n_C^0} \right] = 0,$$

$$1 + \left[\frac{n_B^0}{-\mu_B + U_B(n_B^0 - 1) + U_{AB} n_A^0 + U_{BC} n_C^0} + \frac{n_B^0 + 1}{\mu_B - U_B n_B^0 - U_{AB} n_A^0 - U_{BC} n_C^0} \right] = 0,$$

$$1+\left[\frac{n_C^0}{-\mu_C+U_C(n_C^0-1)+U_{AC}n_A^0+U_{BC}n_B^0}+\frac{n_C^0+1}{\mu_C-U_Cn_C^0-U_{AC}n_A^0-U_{BC}n_B^0}\right]=0. \tag{6.16}$$

The solution of these equations yield the phase boundaries between the SF and MI phases through the following equations

$$\begin{aligned}
\mu_A^{\pm} &= \frac{1}{2}[2(U_{AB}n_B^0+U_{AC}n_C^0)+U_A(2n_A^0-1)-1] \\
&\pm \sqrt{U_A^2-2U_A(2n_A^0+1)} \\
\mu_B^{\pm} &= \frac{1}{2}[2(U_{AB}n_A^0+U_{BC}n_C^0)+U_B(2n_B^0-1)-1] \\
&\pm \sqrt{U_B^2-2U_B(2n_B^0+1)} \\
\mu_C^{\pm} &= \frac{1}{2}[2(U_{AC}n_A^0+U_{BC}n_B^0)+U_C(2n_C^0-1)-1] \\
&\pm \sqrt{U_C^2-2U_C(2n_C^0+1)}.
\end{aligned} \tag{6.17}$$

The results obtained by solving Eq. (6.17) are presented and discussed in section 6.5.

6.4 Numerical Solution

A fully selfconsistent numerical solution of Eq. (6.3) is an additional option to obtain and hence compare and contrast with the analytic phase diagram obtained as discussed above. To capture the possible phases first we obtain the matrix elements of the Hamiltonian in the onsite occupation number basis $|n_A, n_B, n_C\rangle$, in Eq. (6.3) for a set of initial choices for the values of ψ_A, ψ_B and ψ_C. The occupation numbers are truncated at some maximum value $|n_{max}\rangle$ ($n_{max} = 8$ here) for each species. Hence we diagonalize the matrix to find lowest energy and corresponding wave function that may be denoted by $E_g(\psi_A, \psi_B, \psi_C)$ and $\Psi_g(\psi_A, \psi_B, \psi_C)$ respectively. Then we obtain the new SF order parameters ψ_α as given by,

$$\psi_\alpha = \langle\Psi_g(\psi_A, \psi_B, \psi_C)|b_\alpha|\Psi_g(\psi_A, \psi_B, \psi_C)\rangle \tag{6.18}$$

for all the three species respectively. Now the initial choices are replaced by updated values and again repeat this process until we get the selfconsistent solutions, that is the solutions that correspond to a global minima. This procedure is equiv-

alent to a minimization of total energy, $E_g(\psi_A, \psi_B, \psi_C)$ with respect to ψ_A, ψ_B and ψ_C [70,88,94,96]. Once we found the equilibrium solutions, the occupation densities for the three species can be computed from,

$$\rho_\alpha = \langle \Psi_g(\psi_A, \psi_B, \psi_C) | n_\alpha | \Psi_g(\psi_A, \psi_B, \psi_C) \rangle. \tag{6.19}$$

The SF and MI phases are identified by nonzero order parameters (and noninteger densities) and vanishing order parameters (and integer densities) respectively.

6.5 Results

6.5.1 The Strong Coupling Phase Diagram

In Fig. 6.1, we present the results on the phase diagram that are obtained form the strong coupling expansion technique. The boundaries between the superfluid and Mott insulator phase in the $U - \mu$ parameter space are computed from Eq. (6.17) for different choices of the parameters of the BHM in Eq. (6.1). Here the black solid line, green dashed line and magenta dot-dashed line are used for indicating the phase boundaries for A, B and C species respectively. In Fig. 6.1(a), we have shown the phase boundaries of MI(1)$_A$-MI(1)$_B$-MI(1)$_C$ as Mott insulating phases for $n_A = n_B = n_C = 1$ and MI(2)$_A$-MI(2)$_B$-MI(2)$_C$ for Mott insulating phases corresponding to $n_A = n_B = n_C = 2$ which are the two lowest Mott lobes when all the intraspecies interactions are same, that is, $U_A = U_B = U_C = U$ and no interspecies interaction, that is $U_{AB} = U_{BC} = U_{AC} = 0$. We choose to call these phases as MMM phase (M: Mott insulating). These results exactly map on to the results for a single-component BHM as found in earlier studies [71]. This is obvious because when the intraspecies interactions are same and mutual interactions between the interspecies are turned off, three component mixture becomes identical with and behave like a single component fluid.

To investigate the scenario that will emerge as the intra and interspecies interactions are tuned (that are experimentally possible), we have chosen a few typical cases. In Figs. 6.1(b) and (c), we have shown the phase diagram corresponding to $U_A = U_B = U_C = U$ and $U_A = U \neq U_B \neq U_C$ respectively for $U_{AB} = U_{BC} = U_{AC} = 0.6U$ where only the first Mott lobe corresponding to $n_A = n_B = n_C = 1$ are shown. In Fig. 6.1(b), for non-zero interspecies interactions, the horizontal position of the tip of the Mott lobe (critical values of the U_A, U_B and U_C for three species respectively) as well as the shape of the phase boundary

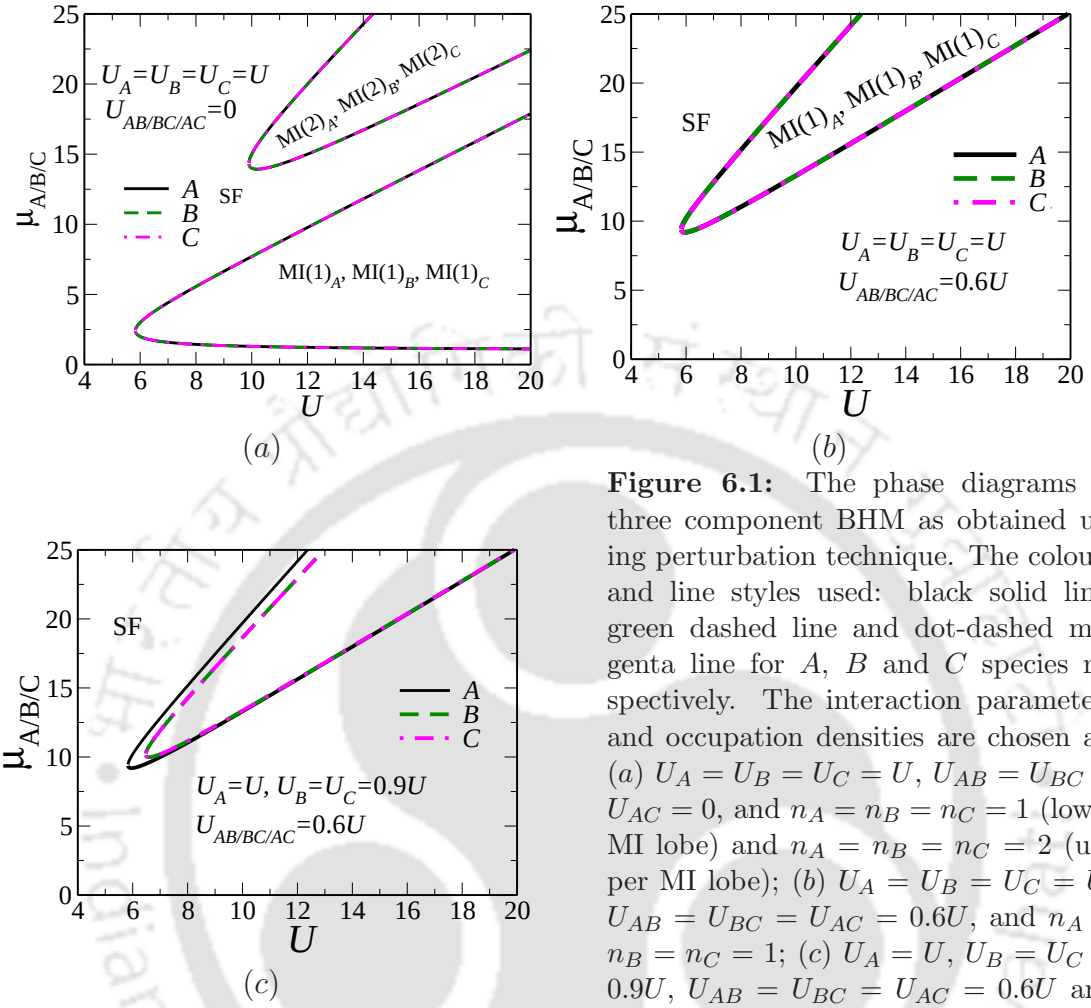

Figure 6.1: The phase diagrams of three component BHM as obtained using perturbation technique. The colours and line styles used: black solid line, green dashed line and dot-dashed magenta line for A, B and C species respectively. The interaction parameters and occupation densities are chosen as: (a) $U_A = U_B = U_C = U$, $U_{AB} = U_{BC} = U_{AC} = 0$, and $n_A = n_B = n_C = 1$ (lower MI lobe) and $n_A = n_B = n_C = 2$ (upper MI lobe); (b) $U_A = U_B = U_C = U$, $U_{AB} = U_{BC} = U_{AC} = 0.6U$, and $n_A = n_B = n_C = 1$; (c) $U_A = U$, $U_B = U_C = 0.9U$, $U_{AB} = U_{BC} = U_{AC} = 0.6U$ and $n_A = n_B = n_C = 1$.

that separate the Mott insulating from the superfluid phase remain unaltered, however its position gets shifted vertically, that is shift towards larger μ values. Thus from Figs. 6.1(a) and (b), it is seen that the system possesses only the SF and MI phases corresponding to three species with boundary for each one of them coinciding with each other, a feature that is linked to the interspacies interaction being the same.

Hence in Fig. 6.1(c), we set $U_A = U$ and $U_B = U_C = 0.9U$, a part of the phase boundary for specie A separates out from that of B or C components giving rise to a new phase which can be termed as Mott insulator-superfluid-superfluid (MSS) in the region of the $U - \mu$ plane that is intervening the black solid line and green dashed line or magenta dot-dashed line. In this region, A specie belongs to the MI phase, with $n_A = 1$ (called it $\mathrm{MI}(1)_A$), whereas B and C components remain in SF phase with a gapless excitation spectrum for each.

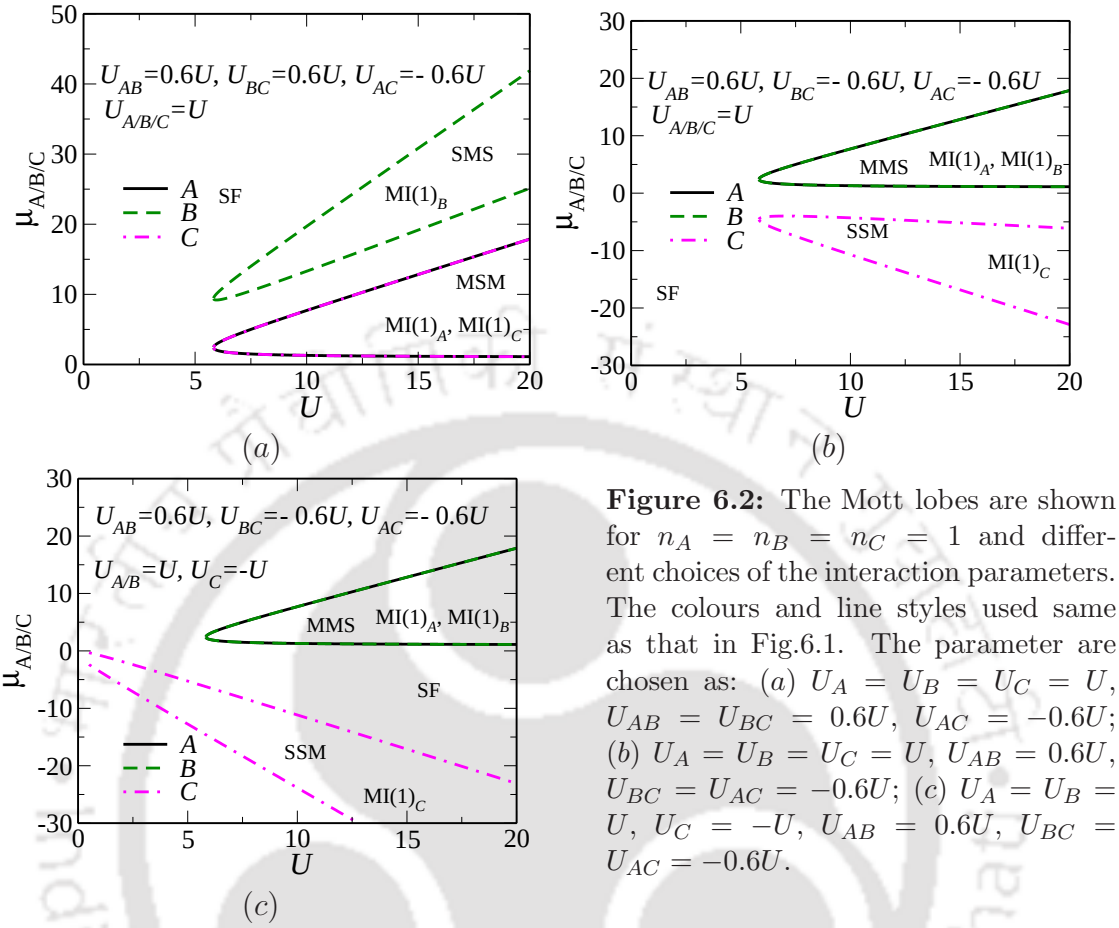

Figure 6.2: The Mott lobes are shown for $n_A = n_B = n_C = 1$ and different choices of the interaction parameters. The colours and line styles used same as that in Fig.6.1. The parameter are chosen as: (a) $U_A = U_B = U_C = U$, $U_{AB} = U_{BC} = 0.6U$, $U_{AC} = -0.6U$; (b) $U_A = U_B = U_C = U$, $U_{AB} = 0.6U$, $U_{BC} = U_{AC} = -0.6U$; (c) $U_A = U_B = U$, $U_C = -U$, $U_{AB} = 0.6U$, $U_{BC} = U_{AC} = -0.6U$.

In Fig. 6.2, we show the phase diagram for the Mott lobes for three sets of interaction parameter values, with both repulsive and attractive combination of the interspecies and intraspecies interaction terms since the possibility of an attraction among different or same species have been predicted by experiments[164]. In Fig. 6.2(a), we keep intraspecies interaction $U_A = U_B = U_C = U$ and interspecies interactions $U_{AB} = U_{BC} = 0.6U$ (all repulsive) while the remaining interspacies interaction, $U_{AC} = -0.6U$ as attractive. The boundary of MI$(1)_B$ for B specie now separates out from the that of the A and C species, creating a superfluid-Mott insulating-superfluid (SMS) and Mott insulating-superfluid-Mott insulating (MSM) mixed phases as indicated in the figure.

In Fig. 6.2(b) we show the phase diagrams keeping the interaction parameters same in magnitude as in Fig. 6.2(a) but with different set of choices for the attractive and repulsive interactions. In Fig. 6.2(b), the phase boundary of the MI(1) lobe for the C specie separates out from the other two species when $U_{BC} = U_{AC} = -0.6U$ and hence create superfluid-superfluid-Mott insulating (SSM) and Mott insulating-Mott insulating-superfluid (MMS) mixed phases. Importantly, the lobe (MI$(1)_C$)

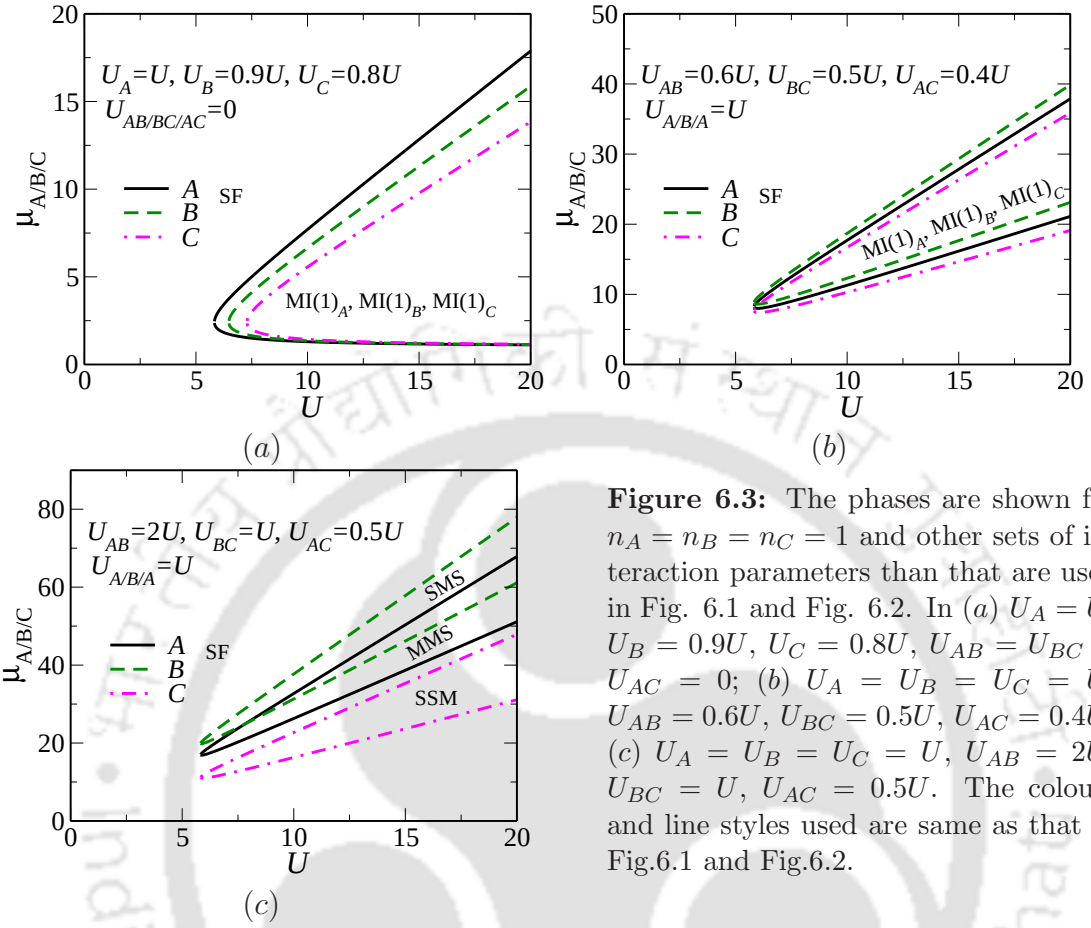

Figure 6.3: The phases are shown for $n_A = n_B = n_C = 1$ and other sets of interaction parameters than that are used in Fig. 6.1 and Fig. 6.2. In (a) $U_A = U$, $U_B = 0.9U$, $U_C = 0.8U$, $U_{AB} = U_{BC} = U_{AC} = 0$; (b) $U_A = U_B = U_C = U$, $U_{AB} = 0.6U$, $U_{BC} = 0.5U$, $U_{AC} = 0.4U$; (c) $U_A = U_B = U_C = U$, $U_{AB} = 2U$, $U_{BC} = U$, $U_{AC} = 0.5U$. The colours and line styles used are same as that in Fig.6.1 and Fig.6.2.

occurs at negative values of the chemical potential, with the lobes corresponding to the other two components occur at positive μ values.

In Fig. 6.2(c), it is observed that when U_C, U_{BC} and U_{AC} are made attractive, the Mott boundary for C specie separates away and its tip also shifts towards significantly lower values of U as shown in Fig. 6.2(c). Again the Mott lobe for the C specie is found in the negative μ regime. The orientation of the MI$(1)_C$ is also considerably altered with its tip pointing upwards, that is, towards less negative μ values. Further such choices for the intra and interspecies interactions will give rise to additional features, however a few representative cases showing mixed phases were sufficient to demonstrate the interest contained therein.

In Fig. 6.3, we present the phase diagram for mutually unequal strengths of the interspecies and intraspecies interactions. In Fig. 6.3(a), the parameter values are taken as: $U_{AB} = U_{BC} = U_{AC} = 0$ and $U_A = U$, $U_B = 0.9U$ and $U_C = 0.8U$. The upper phase boundary of the MI$(1)_B$ and MI$(1)_C$ lobes shifts to lower values of μ, as the intraspecies interaction strengths are reduced. When the intraspecies interactions are same, but interspecies interaction are slightly different form each

other ($U_{AB} = 0.6U, U_{BC} = 0.5U, U_{AC} = 0.4U$), both the upper and lower boundaries get separated for the three species and also shift to higher values of the chemical potential and are shown in Fig. 6.3(b). In Fig. 6.3(c), when the difference between the values of interspecies is somewhat large ($U_{AB} = 2U$, $U_{BC} = U$, $U_{AC} = 0.5U$), the MI$(1)_C$ lobe for C component gets completely separated out and gives rise to various mixed phases.

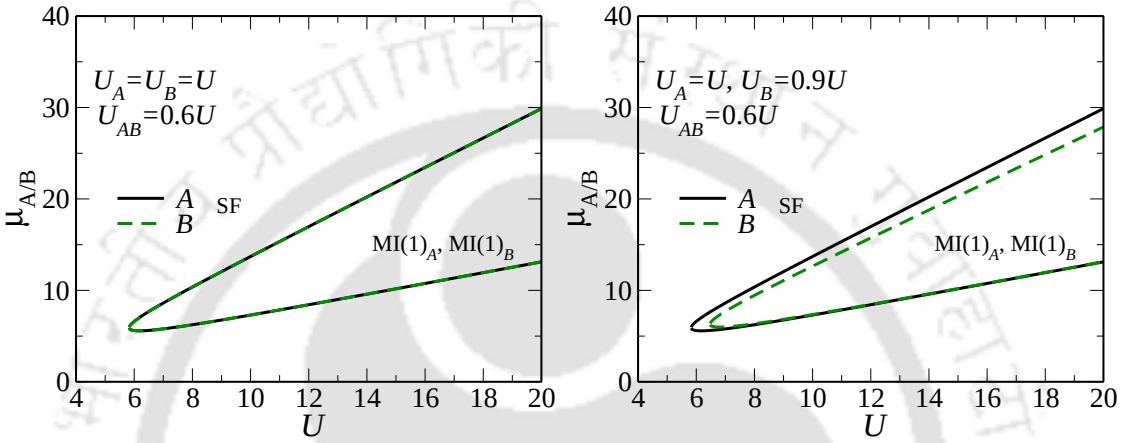

Figure 6.4: The phase boundaries of two component BHM in the $U-\mu$ plane as obtained via perturbation technique for parameter values $U_A = U_B = U$, $U_{AB} = 0.6U$ in (a) and $U_A = U$, $U_B = 0.9U$, $U_{AB} = 0.6U$ in (b). The colours and line styles used as black solid line and green dashed line for A and B species respectively.

To complete the discussion on the phase diagrams that are obtained from perturbation technique, we present the results for a two component bosonic mixture that can be found in our calculation by putting one of the onsite intraspecies interaction and two of the interspecies interaction to be zero. For example, we can put $U_C = U_{AC} = U_{BC} = 0$ to describe a two component mixture as shown in Fig. 6.4. To compare the results with those for three component mixtures presented in Fig. 6.1(b) and (c), we choose the parameter values as $U_A = U_B = U$, $U_{AB} = 0.6U$ in Fig. 6.4(a) and $U_A = U$ $U_B = 0.9U$, $U_{AB} = 0.6U$ in Fig. 6.4(b) respectively. In both the cases the MI$(1)_A$-MI$(1)_B$ (MM) and MI$(1)_A$-SF$_B$ (MS) phase occur at lower values of μ compared to MI$(1)_A$-MI$(1)_B$-MI$(1)_C$ and MI$(1)_A$-SF$_B$-SF$_C$ phases in Fig. 6.1(b) and (c). Qualitatively similar results are obtained in Ref.[166].

6.5.2 The Numerical Phase Diagram

A corroboration of the above results can be obtained via numerical solution of the MF Hamiltonian in Eq. (6.3). Quite interestingly, there are emergence of insulating

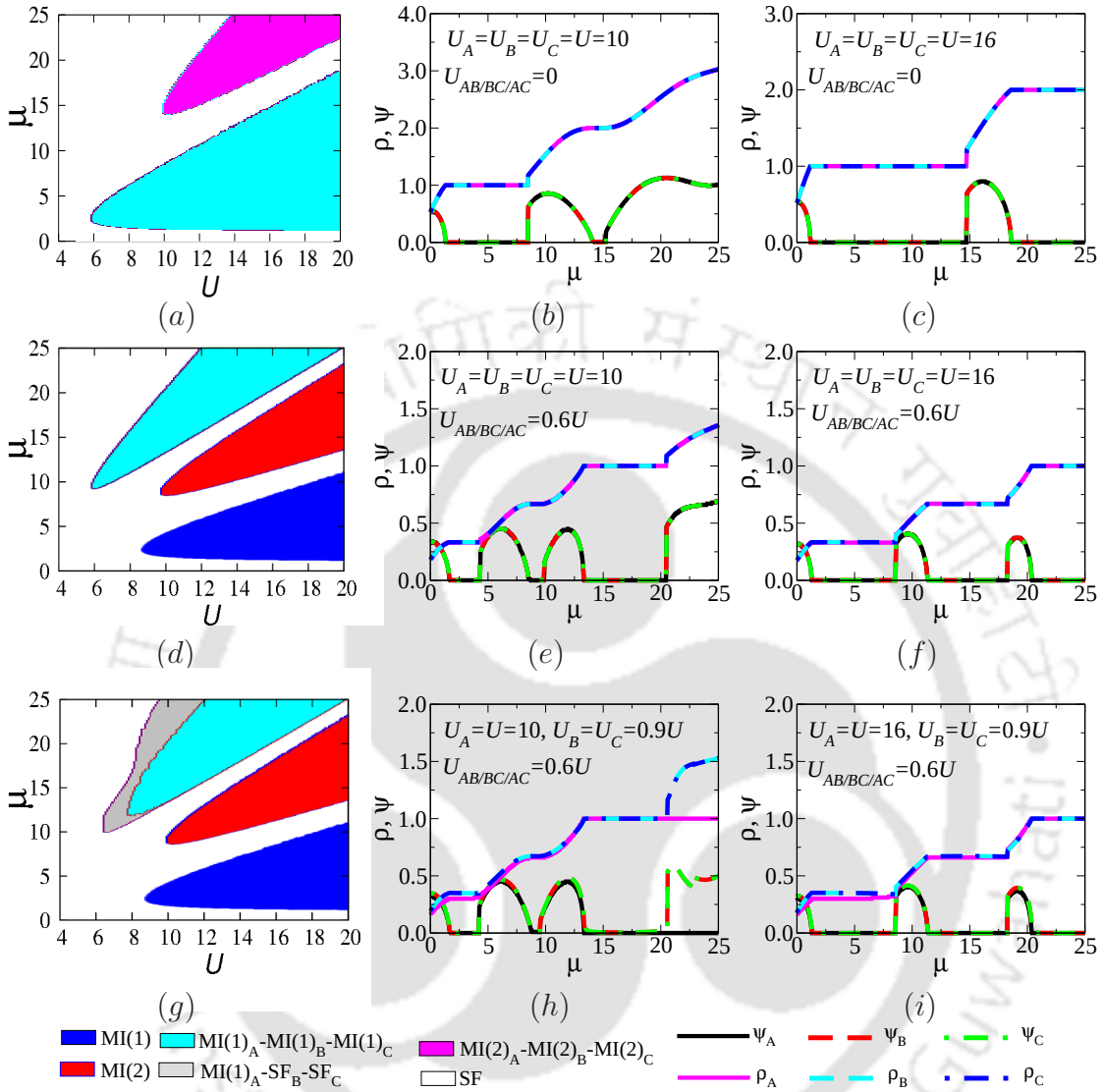

Figure 6.5: The plots show the numerically obtained phase diagrams in (a), (d) and (g) and in second and third columns we show the 1D plots of ψ and ρ as a function of chemical potential, μ for $U = 10$. (see $(b), (e), (h)$) and $U = 16$ (see $(c), (f), (i)$) respectively. The colours for different phases and colour codes and line styles for 1D plots are indicated below the figure. For comparison, in first column, we present the phase diagrams for the same parameter values as that used in Fig. 6.1.

phases formed by fractional occupancies of the individual components, which when summed over yields an integer. These insulating phase could not be accessed earlier via the strong coupling methods. In Fig. 6.5, we show results obtained from these numerical calculations. In the first column (Figs. (a), (d) and (g)), we present the phase diagrams based upon the behaviour of SF order parameters, ψ_α and densities, ρ_α (same as that of n as used in the strong coupling expansion section) corresponding

to the three bosonic components for different choices of the parameter values of the Hamiltonian. While in second and third columns, we show the variation of SF order parameters and densities corresponding vertical scan of the phase diagram, that is as a function of the chemical potential at few different values of the onsite potential, U. To distinguish the different phases in the phase diagrams, we use certain colour codes based on the values of ψ_α and ρ_α that are presented in table 6.1. The phase diagrams are presented in Figs. 6.5 (a), (d) and (g) for the parameter values same as that in Figs. 6.1(a), (b) and (c) respectively. The variation of ψ_α and ρ_α as a function of μ at two different values of U ($U = 10$ and $U = 16$) for each of the three phase diagrams are shown in Figs. 6.5 (b), (c) Figs. 6.5 (e), (f) and Figs. 6.5 (h), (i) respectively. For this purpose we use black (magenta) solid line, red (cyan) dashed line and green (blue) dot-dashed line are used for ψ_A (ρ_A), ψ_B (ρ_B) and ψ_C (ρ_C) respectively. These vertical scans of the phase diagrams yield values of ψ_α and ρ_α corresponding to different phases which are are presented in table 6.1.

Colour	(ψ_A, ρ_A)	(ψ_B, ρ_B)	(ψ_C, ρ_C)	(ψ, ρ)	Phase
blue	$(0, \frac{1}{3})$	$(0, \frac{1}{3})$	$(0, \frac{1}{3})$	(0,1)	MI(1)
red	$(0, \frac{2}{3})$	$(0, \frac{2}{3})$	$(0, \frac{2}{3})$	(0, 2)	MI(2)
cyan	(0, 1)	(0, 1)	(0, 1)	(0, 3)	$\text{MI}(1)_A$-$\text{MI}(1)_B$-$\text{MI}(1)_C$
grey	(0, 1)	(>0, >0)	(>0, >0)	(0, > 1)	$\text{MI}(1)_A$-SF_B-SF_C
magenta	(0, 2)	(0, 2)	(0, 2)	(0, 6)	$\text{MI}(2)_A$-$\text{MI}(2)_B$-$\text{MI}(2)_C$
white	(>0, >0)	(>0, >0)	(>0, >0)	(>0, >0)	SF

Table 6.1: The table represents the value of the order parameters ψ_α, and occupation densities, ρ_α that characterize the different compressible and insulating phases in Figs. 6.5 (a), (d) and (g). Also the colour codes that are used to differentiate various phases in the phase diagrams are mentioned.

It is interesting to note that the first Mott lobe is formed with $\rho_A = \rho_B = \rho_C \simeq \frac{1}{3}$ such that the total density becomes unity and the second lobe ($\rho = 2$) corresponds to each of the densities being $\frac{2}{3}$. Other fractional values for the densities which add up to an integer, such as a combination $(\frac{1}{4}, \frac{1}{4}, \frac{1}{2})$ (or a combination of fractional and integer occupancies, such as $(\frac{1}{2}, \frac{1}{2}, 1)$ or any permutation therein) may or may not appear in the phase diagram. A lot will depend upon the choice of the interaction parameters. We indeed have scanned the scenario for a few other sets of values for the interaction parameters, however have found no evidence for phases with such different combinations as cited above; although not ruling out their possibilities.

As earlier, the results corresponding to a two component mixture can be useful for a comparison with those for the three component mixtures. For this purpose,

we solved the MF Hamiltonian for a two component bosonic mixture and presented the results in Fig. 6.6. Again we choose the parameter values as $U_A = U_B = U$, $U_{AB} = 0.6U$ in Fig. 6.6(a) and $U_A = U$, $U_B = 0.9U$, $U_{AB} = 0.6U$ in Fig. 6.6(d) in order to make a comparison with the results for three species as presented in Figs. 6.5 (d), (g) respectively. The phase diagrams presented in Fig. 6.6(a) and (d) show:

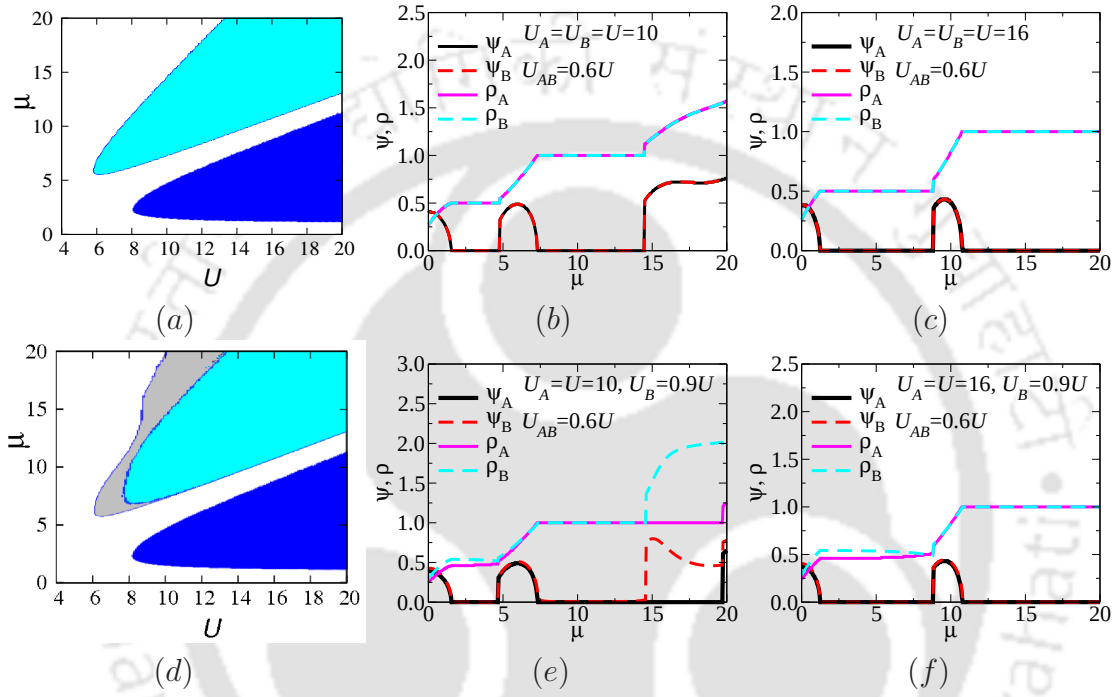

Figure 6.6: The numerically obtained phase diagrams in the $U-\mu$ plane for the parameter values $U_A = U_B = U$, $U_{AB} = 0.6U$ in (a) and $U_A = U$, $U_B = 0.9U$, $U_{AB} = 0.6U$ in (d). The colours blue, cyan and gray are used to indicate the MI(1), MI(1)$_A$-MI(1)$_B$ and MI(1)$_A$-SF$_B$ respectively (see text for detailed discussion). In second and third columns we show the 1D plots of ψ and ρ as a function of chemical potential, μ for $U = 10$. (see (b), (e)) and $U = 16$ (see (c), (f)) respectively. The black and magenta solid lines are used for ψ_A and ρ_A and red and cyan dashed lines are used for ψ_B and ρ_B.

(i) an SF phase (white colour) in which both species are superfluid ($\psi_A \neq \psi_B > 0$), (ii) a MI(1) lobe (blue colour) denoting a MI phase in which $\psi_A \neq \psi_B = 0$ and $\rho_A \simeq \rho_B = \frac{1}{2}$, ($iii$) a Mott insulating phase, MI(1)$_A$-MI(1)$_B$ (cyan colour) and (iv) a Mott insulating-superfluid (MI(1)$_A$-SF$_B$) phase (gray colour) in which $\psi_A = 0$, $\rho_A = 1$, $\psi_B > 0$ and $\rho_B > 0$. Figs. 6.6(b), (c), (e) and (f) show the variation of ψ and ρ for two species A and B as a function of μ that correspond to the vertical scans of the phase diagrams in Figs. 6.6(a) and (d) at $U = 10$ ($U = 16$) in Figs. 6.6(b) and (d) (Figs. 6.6(c) and (f)) respectively. Thus the ψ and ρ values that define different phases can be seen from the one dimensional plots.

6.5.3 Compressibility

To see the behaviour of a physical quantity for a three component mixture, we compute the compressibility corresponding to the three species defined as $\kappa_\alpha = \frac{\partial \rho_\alpha}{\partial \mu}$ as a function of chemical potential are shown in Fig. 6.7. It is obvious that the compressibility is finite for the superfluid phase while it vanishes in the Mott insulator phase. In Fig. 6.7 we have shown the variation of κ_α ($\alpha \in A, B, C$) as μ increases for the interaction parameters, $U_A = U$, $U_B = U_C = 0.9U$, and $U_{AB} = U_{BC} = U_{AC} = 0.6U$ at $U = 10$ in Fig. 6.7(a) and $U = 16$ in Fig. 6.7(b) (same parameters as in Fig. 6.5(h) and (i) respectively). It is found that the κ_α is zero in the MI(1), MI(2) and MI$(1)_A$-MI$(1)_B$-MI$(1)_C$. But in the MI$(1)_A$-SF$_B$-SF$_C$ phase, the compressibility is zero for component A, while it is non zero for B and C species, thereby strengthening the claim for occurrence of the mixed phases.

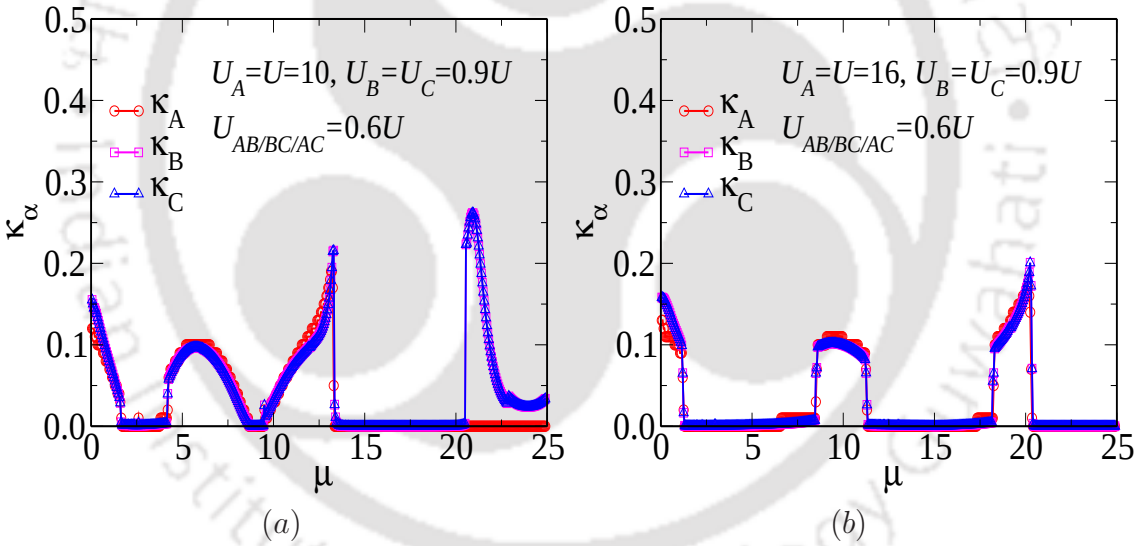

Figure 6.7: The variation of compressibility, κ_α ($\alpha \in A, B, C$) as a function of chemical potential, μ for the values of interaction parameters chosen for (a) and (b) same as that used in Fig. 6.5(h) and (i) respectively.

6.6 Possible Relevance on the Experimental Scenario

The stability criterion of a bosonic mixtures can be determined by the intra and interparticle interaction parameters which in turn depend on the s-wave scattering lengths (see section 6.1) . Hence we attempt to find out possible conditions on the interaction parameters for a three component bosonic mixture that is of interest

to us. To find the condition for a uniform ground state, we looked at the energy landscape. Assuming it is to be quadratic in terms of bosonic densities, one can write the ground state energy as,

$$\begin{aligned} E_{gs} = \quad & \frac{1}{2}\big[U_A n_A^2 + U_B n_B^2 + U_C n_C^2 \\ & +2(U_{AB} n_A n_B + U_{BC} n_B n_C + U_{AC} n_A n_C)\big]. \end{aligned} \tag{6.20}$$

Rewriting the above equation in matrix notations (in the bases of n_A, n_B and n_C), we get,

$$E_{gs} = \begin{bmatrix} \frac{U_A}{4} & \frac{U_{AB}}{2} \\ \frac{U_{AB}}{2} & \frac{U_B}{4} \end{bmatrix} + \begin{bmatrix} \frac{U_B}{4} & \frac{U_{BC}}{2} \\ \frac{U_{BC}}{2} & \frac{U_C}{4} \end{bmatrix} + \begin{bmatrix} \frac{U_A}{4} & \frac{U_{AC}}{2} \\ \frac{U_{AC}}{2} & \frac{U_C}{4} \end{bmatrix}. \tag{6.21}$$

Then we diagonalize each of the 2×2 matrices to obtain their eigenvalues. For example, the eigenvalues of the first matrix on the left hand side of Eq. (6.21) is given by,

$$\lambda_{\pm} = \frac{1}{8}\left[(U_A + U_B) \pm \sqrt{(U_A + U_B)^2 + 4\left(U_{AB}^2 - \frac{U_A U_B}{4}\right)}\right]. \tag{6.22}$$

To avoid λ_- from being negative, U_A, U_B and U_{AB} must satisfy the following condition,

$$U_{AB}^2 \leq \frac{1}{4} U_A U_B. \tag{6.23}$$

Similarly, from the other matrices, the relations between the other interaction parameters can be found as,

$$U_{BC}^2 \leq \frac{1}{4} U_B U_C \tag{6.24}$$

and

$$U_{AC}^2 \leq \frac{1}{4} U_A U_C. \tag{6.25}$$

Thus combining all the three conditions appearing in Eqs. (6.23)-(6.24) we find,

$$U_{AB}^2 + U_{BC}^2 + U_{AC}^2 \leq \frac{1}{4}\big[U_A U_B + U_B U_C + U_A U_C\big] \tag{6.26}$$

which may be considered as the stability criterion for the three component bosonic mixture.

To establish a connection with experiments, we look for the s-wave scattering lengths of bosonic atoms that were used in experiments with two component mix-

tures. Let us take a particular case of a two component $^{168}Yb -^{170} Yb$ bosonic mixture[164]. The s-wave scattering lengths of $^{168}Yb -^{168} Yb$, $^{168}Yb -^{170} Yb$ and $^{170}Yb -^{170} Yb$ are 13.33, 6.19 and 3.38 (in units of a_0, a_0 being the Bohr radius) respectively. The masses of these isotopes being almost the same, the onsite interaction parameter is expected to depend solely on the s-wave scattering lengths. Thus we see that the intraspecies interaction strengths, viz. $^{168}Yb -^{170} Yb$ (that is U_{AB} (say)) is greater than $^{170}Yb -^{170} Yb$ (U_B (say)). Thus the condition obtained in Eq. (6.23) is violated. Hence an immediate connection with experiments can not be established. However, without trepidation it can be said that the intra and interatomic interaction between bosons play a crucial role for the stability of the mixture. Possibly a more refined treatment is needed to address the issue.

6.7 Conclusions

Analytic computation of the strong coupling phase diagram for a system comprising of a mixture of three bosonic species yields interesting mixed phases. Example of such mixed phases consists of one specie of atoms being in the superfluid phase, denoting a zero gap in the excitation spectrum for that specie, with the other two species showing an insulating behaviour. If "*time of flight*" experiments are selectively possible for the individual components, which may be feasible if the masses (and hence the interaction parameters) of the participating species are considerably different from each other, then such mixed phases may be experimentally realizable. Further, signatures of insulating phases with fractional occupancies for the individual components emerge from the numerical studies of the mean field Bose Hubbard model.

Chapter 7

Summary and Conclusions

Investigation of Model Hamiltonians with competing interactions and their relevance to the experimental paradigm has always been fascinating to the condensed matter physicists. With the realization of Bose Einstein condensation in the laboratories and creation of lattice structures using laser beams have contributed immensely to the study of atomic gases in a periodic environment. What made such systems more appealing than electrons in a crystal lattice, is that its availability in a pure form, that is without defects and phonons, easy tunability of the interatomic interactions and a very large lattice constant. A number of quantum phenomena, which were otherwise difficult to observe in crystal lattices, can therefore have the possibility of being observed in optical lattices.

Mott insulator (MI) to a superfluid (SF) transition in a system of interacting bosons is one such phenomenon which was observed experimentally via *"time of flight"* spectroscopic methods. The SF-MI transition can easily be captured theoretically using a Bose Hubbard model (BHM). A simple minded single site mean field theory on the BHM predicts the qualitatively correct phase diagram.

After a quick survey of literature, during the early days of working on the thesis, we found that the mean field theory, albeit simple, still holds the promise of answering a few questions that we have in mind. The questions mainly were concerned about the roles of the optical lattice, disorder and the Bose glass (BG) phase, dipolar interactions, multi-component mixtures etc. Hopefully we have been able to answer some of them to our satisfaction. A brief recap of the main results follows after this.

In this thesis we have studied the ground state properties of interacting bosons on a lattice for a few different cases. The first one deals with the condensate properties of bosons in different 2D lattice geometries. The second problem deals with the disordered BHM to characterize and contrast the BG phase from MI and SF phases

in the phase diagram defined by the plane formed of the chemical potential and the onsite interaction. Next we investigate the existence of different exotic density ordered phases in presence of exchange interaction in the BHM for non-bipartite lattice for homogeneous case. Then we extend this work in presence of a quadratic confining potential. Finally we observed the possible emergence of various phases in a three component bosonic mixture. A little more elaboration of the main results obtained by us in the preceding chapters is included here.

We have investigated how the condensate properties depend on the coordination number and the underlying geometry of interacting bosons in 2D optical lattices. For this purpose we have chosen square, triangular, honeycomb and kagome lattice geometries. The condensate properties, showed an enhanced condensate density for the triangular lattice geometry, followed by square and honeycomb lattices. The results can be explained by noting a large coordination number, a large quasiparticle velocity, the quasiparticle density of states data corresponding to the geometry. Further to investigate whether the condensate properties solely depends on the coordination number, we have compared the condensate fraction data for square and kagome lattice geometries as both these have the same coordination number. The result indeed showed enhanced condensate density fraction for the square lattice compared to that of the kagome lattice. All the above mentioned results form the content of chapter 2.

In chapter 3, we have presented the phase diagram of disordered BHM via a percolation scenario in presence of random onsite disorder. The different emerging phases were characterized by various physical quantities such as the ratio of the sites having integer occupancies and vanishing SF order parameter to the total number of sites, relative fluctuation of the boson densities and the information entropy. The onset of the BG phase was found to occur as the sites with integer density started percolating through the lattice. This happened very nearly at the percolation threshold of 0.598, a value well known for the random site percolation model in 2D. We succeeded in obtaining the phase diagram of the disordered BHM only by looking the γ values. It is observed that in presence of disorder, the SF phase persisted till large value of U and the BG phase itself increased in size as disorder strength was increased.

Further we studied the phase diagram of dipolar bosons in non-bipartite lattices by solving the extended BHM (EBHM). Prototype of a kagome lattice was considered as an example here. We performed strong coupling expansion on the EBHM,

and hence supported it by the numerical solution of the mean field Hamiltonian. We found that the *'chemical potential width'* of DW phases only depends of the exchange interaction strengths while for MI phases depends on onsite interaction strengths. We observed emergence of exotic density ordered phases such as DW($\frac{1}{3}$), DW($\frac{2}{3}$) etc. and a supersolid phase. Various physical properties, such as structure factor, superfluid stiffness, compressibility etc. were computed to characterize all the compressible (SF, SS) and insulating (MI, DW) phases. The discussions were included in chapter 4.

We extended the work of chapter 4 by including the effects of harmonic trapping in chapter 5. The EBHM with a quadratic potential term is studied via inhomogeneous mean field theory. We observed the coexistence of different phases, such as SF, MI, supersolid, density ordered phases etc. The lattice had split into various concentric shells owing to the symmetry of the onsite potential. The corresponding scenario for the bipartite lattices was compared and contrasted. Physical quantities, such as order parameter and density in the momentum space compressibility were computed.

Finally we have studied a three component BHM. We observed various kinds of mixed phases, with one component in the MI phase and the other two in the SF phase (denoted by MSS) etc. Cases corresponding to the same and different, attractive and repulsive inter and intraspecies interaction parameters were considered. MI phases with fractional occupancies for the individual components were noted. The compressibility for different component of bosons are computed to characterize different superfluid and insulating phases. Further we have observed MI phases formed by fractional densities of the individual components which of course, sum up to an integer. We have also included the results for two component mixtures for comparison. Chapter 6 comprises of the above findings.

Appendix A

Number Fluctuations of the Condensate Atoms

First we consider a condensate of bosonic atoms in a double well potential[126]. In the *'two mode'* approximation, the number fluctuation is given by,

$$(\Delta n)^2 = \langle(\hat{n}_1 - \hat{n}_2)^2\rangle - \langle(\hat{n}_1 - \hat{n}_2)\rangle^2 \tag{A.1}$$

where $\hat{n}_i = a_i^\dagger a_i$ represents the bosonic density in a given well labeled by i. Applying Bogoliubov approximation, the number operators can be written as,

$$\begin{aligned} \hat{n}_1 &= (z_0^* + \hat{\delta}_1^\dagger)(z_0 + \hat{\delta}_1) \\ \hat{n}_2 &= (z_0^* + \hat{\delta}_2^\dagger)(z_0 + \hat{\delta}_2) \end{aligned} \tag{A.2}$$

z_0 being the average value of bosonic operators which is a real quantity and $\hat{\delta}$ be the fluctuation around the ground state. Neglecting the higher order fluctuation terms, the quantity $(\hat{n}_1 - \hat{n}_2)$ in Eq. (A.1) can be written as,

$$(\hat{n}_1 - \hat{n}_2) = z_0\left[(\hat{\delta}_1^\dagger + \hat{\delta}_1) - (\hat{\delta}_2^\dagger + \hat{\delta}_2)\right]. \tag{A.3}$$

By introducing, $\hat{\delta}_\pm$ defined by,

$$\hat{\delta}_\pm = \frac{1}{\sqrt{2}}(\hat{\delta}_1 \pm \hat{\delta}_2). \tag{A.4}$$

Eq. (A.3) becomes

$$(\hat{n}_1 - \hat{n}_2) = \sqrt{2}z_0(\hat{\delta}_- + \hat{\delta}_-^\dagger). \tag{A.5}$$

We then use Bogoliubov transformation for the operators $\hat{\delta}_{\pm}$ as,

$$\hat{\delta}_{\pm} = u_{\pm}\hat{\alpha} + v_{\pm}^{*}\hat{\alpha}^{\dagger} \tag{A.6}$$

where $u_{\pm}$, $v_{\pm}$ are amplitudes and the operators $\hat{\alpha}$ and $\hat{\alpha}^{\dagger}$ follow the usual bosonic commutation relation, $[\hat{\alpha}_{\mathbf{k}}, \hat{\alpha}^{\dagger}_{\mathbf{k}'}] = \delta_{\mathbf{k}\mathbf{k}'}$. In terms of $\hat{\alpha}$ and $\hat{\alpha}^{\dagger}$, Eq. (A.5) reduces to

$$(\hat{n}_1 - \hat{n}_2) = \sqrt{2}z_0 \left[(u_{-}\hat{\alpha} - v_{-}^{*}\hat{\alpha}^{\dagger}) + (u_{-}^{*}\hat{\alpha}^{\dagger} - v_{-}\hat{\alpha})\right]. \tag{A.7}$$

Hence, the mean square fluctuation can be written as,

$$\begin{aligned}(\Delta n)^2 &= \langle(\hat{n}_1 - \hat{n}_2)^2\rangle - \langle(\hat{n}_1 - \hat{n}_2)\rangle^2 \\ &= 2z_0^2 \left\langle((u_{-}\hat{\alpha} - v_{-}^{*}\hat{\alpha}^{\dagger}) + (u_{-}^{*}\hat{\alpha}^{\dagger} - v_{-}\hat{\alpha}))^2\right\rangle \\ &= N_0(u_{-} - v_{-})^2 \end{aligned} \tag{A.8}$$

where N_0 is the total number of atoms in the two wells.

Generalizing it to a lattice in a similar manner, the fluctuation of the number of atoms in the same manner can be found to acquire the following form.

$$(\Delta n_0)^2 = \langle(\hat{n}_i)^2 - \langle(\hat{n}_i)\rangle^2\rangle = \frac{n_0}{N}\sum_{\mathbf{k}} |u_{\mathbf{k}} - v_{\mathbf{k}}|^2 \tag{A.9}$$

where n_0 is the condensate density and N denote the total number of k-points in the sum.

Appendix B

Obtaining Phase Diagram via perturbation Calculation for Uniform Disorder

The mean field Hamiltonian from Eq. (3.3) is,

$$H^{MF} = \frac{1}{2}U\hat{n}(\hat{n}-1)(\mu-\epsilon)\hat{n} - \phi(b+b^{\dagger}) + |\psi|^2 \tag{B.1}$$

where we have ignored the site indices. First we shall describe the phase boundary for the homogeneous system. We resort to a strong coupling theory and treat the kinetic energy term as perturbation.

$$H^{eff} = H^0 + \psi H^{'}$$

where $H^{(0)}$ and $H^{'}$ is given by,

$$H^0 = \frac{1}{2}U\hat{n}(\hat{n}-1) - \mu\hat{n} + \psi^2 \tag{B.2}$$

and

$$H^{'} = -(b+b^{\dagger}). \tag{B.3}$$

The unperturbed ground state energy with g particle in its ground state is

$$E_g^{(0)} = \frac{1}{2}Ug(g-1) - \mu g + \psi^2. \tag{B.4}$$

The second order energy correction is given by,

$$\begin{aligned} E_g^{(2)} &= \sum_{n \neq g} \frac{|\langle g|H^{'}|n\rangle|^2}{E_g^{(0)} - E_n^{(0)}} \\ &= \psi^2 \left[\frac{g}{U(g-1)-\mu} + \frac{g+1}{\mu - Ug} \right]. \end{aligned} \tag{B.5}$$

Following the Landau procedure for second order phase transitions, the free energy in terms of the order parameter ψ is given by,

$$F(\psi) = a_0 + a_2|\psi|^2 + a_4|\psi|^4 + ... \tag{B.6}$$

The phase boundary between the SF and MI phases can be obtained by equating the coefficient of $|\psi|^2$ that is, $a_2 = 0$ which gives

$$a_2 = \left[\frac{g}{U(g-1)-\mu} + \frac{g+1}{\mu - Ug} \right] + 1 = 0. \tag{B.7}$$

The above equation yields the phase boundary and is given by the bounding values of the chemical potential, μ,

$$\mu^{\pm} = \frac{1}{2}[U(2g-1)-1] \pm \frac{1}{2}\sqrt{U^2 - 2U(2g+1)+1}. \tag{B.8}$$

In presence of an on-site random disorder with a homogeneous distribution, the chemical potential is rendered inhomogeneous, and hence one has to calculate the disorder averaged free energy of the system $\overline{F(\psi)}$[136]. In this case, the equation $\overline{a_2} = 0$ will give the phase boundary. Where $\overline{a_2} = 0$ represents the disorder average coefficient. Hence

$$\int_{-\infty}^{+\infty} d\mu^{'} p(\mu - \mu^{'}) \left[\frac{g}{U(g-1)-\mu^{'}} + \frac{g+1}{\mu^{'} - Ug} \right] + 1 = 0. \tag{B.9}$$

For a homogeneous disorder distribution in the interval $\epsilon \in [-\Delta, \Delta]$

$$p(\epsilon) = \frac{1}{2}\left[\Theta(\epsilon + \Delta) - \Theta(\epsilon - \Delta)\right]. \tag{B.10}$$

See Fig. 3.1. Eq. (B.9) reduces to,

$$\frac{1}{2\Delta}\int_{\mu-\Delta}^{\mu+\Delta} d\mu^{'}\left[\frac{g}{U(g-1)-\mu^{'}}+\frac{g+1}{\mu^{'}-Ug}\right]=-1$$

$$\Rightarrow \quad \frac{1}{2\Delta}\left[g \;\; ln\frac{\mu-U(g-1)+\Delta}{\mu-U(g-1)-\Delta}-(g+1) \;\; ln\frac{Ug-\mu-\Delta}{Ug-\mu+\Delta}\right]=1. \quad \text{(B.11)}$$

Solving this equation numerically, we have shown the phase boundary (see Fig. B.1) of the SF and the MI phases in the $U-\mu$ plane for $\Delta=4$. The results for $\Delta=0$ using Eq. (B.8) is introduced for comparison. The region intervening between $\Delta=0$

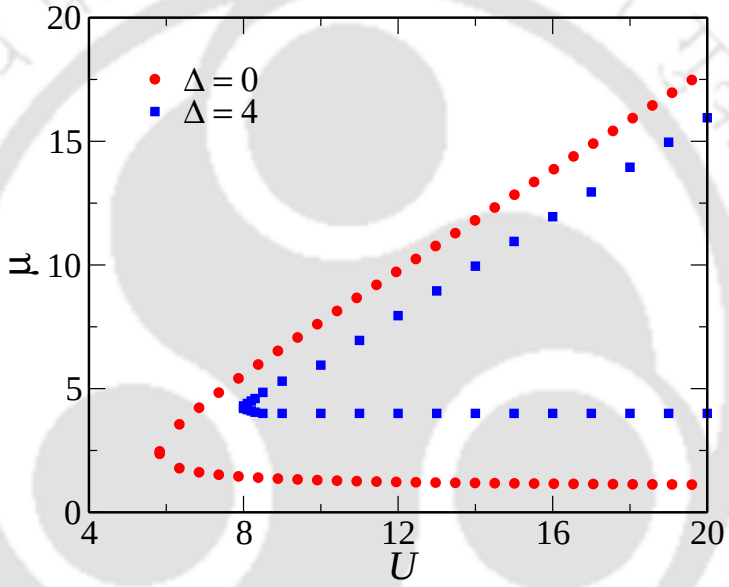

Figure B.1: The plot shows the phase boundaries between SF and MI phases for $\Delta=4$ are obtained from perturbation calculation. $\Delta=0$ case is introduced to demarcate the BG region.

and $\Delta=4$ represents the Bose glass phase.

Appendix C

Calculation of 'Chemical Potential Width' of Various Incompressible (DW, MI) Phases for EBHM

In the atomic $t = 0$ limit, the kinetic energy vanishes, hence the boson number operator $\hat{n}_i$ commutes with all of the remaining term of the Hamiltonian[67]. Therefore each lattice site is occupied with a fixed number of bosons, n and hence the system is said to be in an insulating phase. In this limit the single site Hamiltonian can be written as,

$$H_j = \frac{U}{2}\hat{n}_j(\hat{n}_j - 1) - \mu_j\hat{n}_j + \frac{1}{2}V\hat{n}_j(\hat{n}_k + \hat{n}_l) \tag{C.1}$$

where k and l are neighbours of j. For example, if $j \in A$ sublattice, then k and l belong to B and C sublattices respectively and so on. We consider the boson occupancies of sublattices A, B and C to be n_A, n_B and n_C respectively. Thus energies corresponding to the Mott phase for $n_A = n_B = n_C = n_0$ at each site of the three sublattices are same and hence given by,

$$E_g^{A/B/C}(n_0, n_0, n_0) = \frac{U}{2}n_0(n_0 - 1) - \mu n_0 + \frac{1}{2}Vn_0(n_0 + n_0). \tag{C.2}$$

In the DW phase, occupancies can assume $n_A = n_B = n_0$ and $n_c = n_0 + 1$. Again the energies at different lattice sites are given by,

$$E_g^A(n_0, n_0, n_0+1) = \frac{U}{2}n_0(n_0-1) - \mu n_0 + \frac{1}{2}Vn_0(n_0+n_0+1) \quad \text{(C.3)}$$

$$E_g^B(n_0, n_0, n_0+1) = \frac{U}{2}n_0(n_0-1) - \mu n_0 + \frac{1}{2}Vn_0(n_0+n_0+1) \quad \text{(C.4)}$$

$$E_g^C(n_0, n_0, n_0+1) = \frac{U}{2}(n_0+1)n_0 - \mu(n_0+1) + \frac{1}{2}V(n_0+1)(n_0+n_0). \quad \text{(C.5)}$$

Since the phase is homogeneous, the energy must be same at all lattice sites belonging to the same sublattice. So $E_g^C - E_g^A = 0$, yields $\mu = Un_0 - \frac{1}{2}Vn_0$, at which the energy corresponding to the state ($n_A = n_0$, $n_B = n_0$, $n_C = n_0$) is degenerate with that of the state ($n_A = n_0$, $n_B = n_0$, $n_C = n_0 + 1$).

For $n_A = n_0$ and $n_B = n_c = n_0 + 1$, the energies at different sublattice sites are given by,

$$E_g^A(n_0, n_0+1, n_0+1) = \frac{U}{2}n_0(n_0-1) - \mu n_0 \frac{1}{2}Vn_0(n_0+n_0+2) \quad \text{(C.6)}$$

$$E_g^B(n_0, n_0+1, n_0+1) = \frac{U}{2}(n_0+1)n_0 - \mu(n_0+1) + \frac{1}{2}V(n_0+1)(n_0+n_0+1) \quad \text{(C.7)}$$

$$E_g^C(n_0, n_0+1, n_0+1) = \frac{U}{2}(n_0+1)n_0 - \mu(n_0+1) + \frac{1}{2}V(n_0+1)(n_0+n_0+1). \quad \text{(C.8)}$$

Again in this phase, the energy must be same at each lattice site belonging to the same sublattice. Hence $E_g^C - E_g^A = 0$ yields $\mu = Un_0 - \frac{1}{2}V(n_0+1)$, at which the energy corresponding to the state ($n_A = n_0$, $n_B = n_0$, $n_C = n_0 + 1$) is degenerate with that of the state ($n_A = n_0$, $n_B = n_0 + 1$, $n_C = n_0 + 1$).

Similarly it turns out that the ground state energy of ($n_A = n_0$, $n_B = n_0 + 1$, $n_C = n_0 + 1$) state is degenerate with the ($n_A = n_0 + 1$, $n_B = n_0 + 1$, $n_C = n_0 + 1$) states at $\mu = Un_0 + V(n_0 + 1)$ respectively.

For the higher occupancy states such as ($n_A = n_0+1$, $n_B = n_0+1$, $n_C = n_0+2$) state, the energy is degenerate with those of the ($n_A = n_0 + 1$, $n_B = n_0 + 1$, $n_C = n_0+1$) and ($n_A = n_0+1$, $n_B = n_0+2$, $n_C = n_0+2$) states at $\mu = U(n_0+1)+V(n_0+1)$ and $\mu = U(n_0 + 1) + \frac{1}{2}V(n_0 + 3)$ respectively. This is how we have generated the information presented in table 4.1.

Appendix D

Second Order Perturbation Theory on the Extended Bose Hubbard Model (EBHM)

Considering the kinetic energy term as perturbation, the mean field Hamiltonian in Eq. 4.3 can be written as,

$$H^{eff} = H^{(0)} + \phi H^{'}$$

where $H^{(0)}$ and $H^{'}$ is given by,

$$H^{(0)} = \frac{1}{2}U\hat{n}(\hat{n}-1) - \mu\hat{n} + \phi\psi + V(\hat{n}\bar{\rho} - \rho\bar{\rho}) \tag{D.1}$$

and

$$H^{'} = -(b + b^{\dagger}). \tag{D.2}$$

we skip the site index. If $|n\rangle$ denotes the unperturbed state with n particle of which $n = g$ are in the ground state then ground state energy can be calculated using $\langle n|H^{(0)}|n\rangle$ and is given by,

$$E_g^{(0)} = \frac{1}{2}Ug(g-1) - \mu g + \phi\psi + V(g\bar{\rho} - \rho\bar{\rho}). \tag{D.3}$$

The second order correction to the energy with Eq. (D.2) as the perturbation is,

$$\begin{aligned} E_g^{(2)} &= \sum_{n\neq g} \frac{|\langle g|H^{'}|n\rangle|^2}{E_g^{(0)} - E_n^{(0)}} \\ &= \phi^2 \left[\frac{g}{U(g-1) - \mu + V\bar{\rho}} - \frac{g+1}{\mu - Ug - V\bar{\rho}} \right]. \end{aligned} \tag{D.4}$$

Hence the total ground state energy up to second order correction is given by (for our convenience we use occupation density g as ρ),

$$\begin{aligned} E_g(\phi) &= \frac{1}{2}U\rho(\rho-1) - \mu\rho + \phi\psi + V(\rho\bar{\rho} - \rho\bar{\rho}) \\ &+ \phi^2\left[\frac{\rho}{U(\rho-1)-\mu+V\bar{\rho}} - \frac{\rho+1}{\mu - U\rho - V\bar{\rho}}\right]. \end{aligned} \tag{D.5}$$

The minimization of the above energy with respect to order parameter ϕ gives rise to order parameter equation which is given by,

$$\psi = 2\phi\left[\frac{\rho+1}{U\rho+V\bar{\rho}-\mu} - \frac{\rho}{U(\rho-1)-\mu+V\bar{\rho}}\right]. \tag{D.6}$$

This order parameter equation consists of three coupled equations for the three sublattices and need to be solved simultaneously. They are given by,

$$\psi_A = (\psi_B+\psi_C)\left[\frac{\rho_A+1}{U\rho_A+\frac{1}{2}V(\rho_B+\rho_C)-\mu} - \frac{\rho_A}{U(\rho_A-1)-\mu+\frac{1}{2}V(\rho_B+\rho_C)}\right], \tag{D.7}$$

$$\psi_B = (\psi_C+\psi_A)\left[\frac{\rho_B+1}{U\rho_B+\frac{1}{2}V(\rho_C+\rho_A)-\mu} - \frac{\rho_B}{U(\rho_B-1)-\mu+\frac{1}{2}V(\rho_C+\rho_A)}\right], \tag{D.8}$$

and

$$\psi_C = (\psi_A+\psi_B)\left[\frac{\rho_C+1}{U\rho_C+\frac{1}{2}V(\rho_A+\rho_B)-\mu} - \frac{\rho_C}{U(\rho_C-1)-\mu+\frac{1}{2}V(\rho_A+\rho_B)}\right]. \tag{D.9}$$

At the phase boundary ψ_A, ψ_B and ψ_C vanishes and the boundary between SF and various incompressible phases can be found from the following equation,

$$\begin{aligned} &\left[\frac{\rho_A+1}{U\rho_A+\frac{1}{2}V(\rho_B+\rho_C)-\mu} - \frac{\rho_A}{U(\rho_A-1)-\mu+\frac{1}{2}V(\rho_B+\rho_C)}\right] \\ &\times\left[\frac{\rho_B+1}{U\rho_B+\frac{1}{2}V(\rho_C+\rho_A)-\mu} - \frac{\rho_B}{U(\rho_B-1)-\mu+\frac{1}{2}V(\rho_C+\rho_A)}\right] \\ &\times\left[\frac{\rho_C+1}{U\rho_C+\frac{1}{2}V(\rho_A+\rho_B)-\mu} - \frac{\rho_C}{U(\rho_C-1)-\mu+\frac{1}{2}V(\rho_A+\rho_B)}\right] = 1 \end{aligned} \tag{D.10}$$

Bibliography

[1] M. H. Anderson, J. R. Ensher, M. R. Matthews, C. E. Wieman, and E. A. Cornell, Science **269**, 198 (1995).

[2] C. C. Bradley, C. A. Sackett, J. J. Tollett, and R. G. Hulet, Phys. Rev. Lett. **75**, 1687 (1995).

[3] K. B. Davis, M. O. Mewes, M. R. Andrews, N. J. van Druten, D. S. Durfee, D. M. Kurn, and W. Ketterle, Phys. Rev. Lett. **75**, 3969 (1995).

[4] H. J. Metcalf and P. van der Straten, J. Opt. Soc. Am. B **20**, 887 (2003).

[5] W. Ketterle and N. Van Druten, Adv. At., Mol., Opt. Phys. **37**, 181 (1996).

[6] D. Jaksch, C. Bruder, J. I. Cirac, C. W. Gardiner, and P. Zoller, Phys. Rev. Lett. **81**, 3108 (1998).

[7] M. Greiner, O. Mandel, T. Esslinger, T. W. Hänsch, and I. Bloch, Nature **415**, 39 (2002).

[8] S. Chu, Rev. Mod. Phys. **70**, 685 (1998).

[9] C. N. Cohen-Tannoudji, Rev. Mod. Phys. **70**, 707 (1998).

[10] W. D. Phillips, Rev. Mod. Phys. **70**, 721 (1998).

[11] T. W. Hansch and A. L. Schawlow, Opt. Comm. **13**, 68 (1975).

[12] D. J. Wineland, J. Dalibard, and C. Cohen-Tannoudji, J. Opt. Soc. Am. B **9**, 32 (1992).

[13] D. J. Wineland, J. Dalibard, and C. Cohen-Tannoudji, J. Opt. Soc. Am. B **9**, 32 (1992).

[14] R. Grimm, M. Weidemüller, and Y. B. Ovchinnikov, Adv. At. Mol. Opt. Phy. **42**, 95 (2000).

[15] P. Jessen and I. Deutsch, Adv. At. Mol. Opt. Phy. **37**, 95 (1996).

[16] P. B. Blakie and C. W. Clark, J. Phys. B: At., Mol. Opt. Phys **37**, 1391 (2004).

[17] I. Bloch, J. Dalibard, and W. Zwerger, Rev. Mod. Phys. **80**, 885 (2008).

[18] C. Chin, R. Grimm, P. Julienne, and E. Tiesinga, Rev. Mod. Phys. **82**, 1225 (2010).

[19] A. J. Moerdijk, B. J. Verhaar, and A. Axelsson, Phys. Rev. A **51**, 4852 (1995).

[20] P. Horak, J.-Y. Courtois, and G. Grynberg, Phys. Rev. A **58**, 3953 (1998).

[21] D. Clément et al., Phys. Rev. Lett. **95**, 170409 (2005).

[22] J. E. Lye, L. Fallani, M. Modugno, D. S. Wiersma, C. Fort, and M. Inguscio, Phys. Rev. Lett. **95**, 070401 (2005).

[23] M. White, M. Pasienski, D. McKay, S. Q. Zhou, D. Ceperley, and B. DeMarco,

Phys. Rev. Lett. **102**, 055301 (2009).
[24] R. Roth and K. Burnett, Phys. Rev. A **68**, 023604 (2003).
[25] G. Roati et al., Nature **453**, 895 (2008).
[26] B. Damski, J. Zakrzewski, L. Santos, P. Zoller, and M. Lewenstein, Phys. Rev. Lett. **91**, 080403 (2003).
[27] U. Gavish and Y. Castin, Phys. Rev. Lett. **95**, 020401 (2005).
[28] D. Clément, A. F. Varòn, J. A. Retter, L. Sanchez-Palencia, A. Aspect, and P. Bouyer, New J. Phys. **8**, 165 (2006).
[29] L. Guidoni, C. Triché, P. Verkerk, and G. Grynberg, Phys. Rev. Lett. **79**, 3363 (1997).
[30] M. P. A. Fisher, P. B. Weichman, G. Grinstein, and D. S. Fisher, Phys. Rev. B **40**, 546 (1989).
[31] G. H. Wannier, Rev. Mod. Phys. **34**, 645 (1962).
[32] W. Zwerger, J. Opt. B: Quantum Semi. Opt. **5**, S9 (2003).
[33] T. Stöferle, H. Moritz, C. Schori, M. Köhl, and T. Esslinger, Phys. Rev. Lett. **92**, 130403 (2004).
[34] I. B. Spielman, W. D. Phillips, and J. V. Porto, Phys. Rev. Lett. **98**, 080404 (2007).
[35] V. Ahufinger, L. Sanchez-Palencia, A. Kantian, A. Sanpera, and M. Lewenstein, Phys. Rev. A **72**, 063616 (2005).
[36] A. Niederberger, T. Schulte, J. Wehr, M. Lewenstein, L. Sanchez-Palencia, and K. Sacha, Phys. Rev. Lett. **100**, 030403 (2008).
[37] L. Sanchez-Palencia, D. Clément, P. Lugan, P. Bouyer, G. V. Shlyapnikov, and A. Aspect, Phys. Rev. Lett. **98**, 210401 (2007).
[38] D. A. Abanin, P. A. Lee, and L. S. Levitov, Phys. Rev. Lett. **98**, 156801 (2007).
[39] G. Roati et al., Phys. Rev. Lett. **99**, 010403 (2007).
[40] G. Thalhammer, G. Barontini, L. De Sarlo, J. Catani, F. Minardi, and M. Inguscio, Phys. Rev. Lett. **100**, 210402 (2008).
[41] S. B. Papp, J. M. Pino, and C. E. Wieman, Phys. Rev. Lett. **101**, 040402 (2008).
[42] A. Albus, F. Illuminati, and J. Eisert, Phys. Rev. A **68**, 023606 (2003).
[43] S. Ospelkaus, C. Ospelkaus, O. Wille, M. Succo, P. Ernst, K. Sengstock, and K. Bongs, Phys. Rev. Lett. **96**, 180403 (2006).
[44] J. K. Freericks and H. Monien, Phys. Rev. B **53**, 2691 (1996).
[45] N. Elstner and H. Monien, Phys. Rev. B **59**, 12184 (1999).
[46] W. Krauth, M. Caffarel, and J.-P. Bouchaud, Phys. Rev. B **45**, 3137 (1992).
[47] C. Trefzger and K. Sengupta, Phys. Rev. Lett. **106**, 095702 (2011).
[48] S. R. Clark and D. Jaksch, Phys. Rev. A **70**, 043612 (2004).
[49] L. D. Carr, R. Chiaramonte, and M. J. Holland, Phys. Rev. A **70**, 043609 (2004).
[50] M. Niemeyer, J. K. Freericks, and H. Monien, Phys. Rev. B **60**, 2357 (1999).
[51] A. Sewer, X. Zotos, and H. Beck, Phys. Rev. B **66**, 140504 (2002).
[52] L. Amico and V. Penna, Phys. Rev. B **62**, 1224 (2000).
[53] R. V. Pai, K. Sheshadri, and R. Pandit, Phys. Rev. B **77**, 014503 (2008).
[54] P. Buonsante and A. Vezzani, Phys. Rev. A **70**, 033608 (2004).

[55] D. S. Rokhsar and B. G. Kotliar, Phys. Rev. B **44**, 10328 (1991).
[56] N. Prokof'ev, B. Svistunov, and I. Tupitsyn, Phys. Lett. A **238**, 253 (1998).
[57] F. Alet, S. Wessel, and M. Troyer, Phys. Rev. E **71**, 036706 (2005).
[58] B. Capogrosso-Sansone, N. V. Prokof'ev, and B. V. Svistunov, Phys. Rev. B **75**, 134302 (2007).
[59] P. Sengupta and S. Haas, Phys. Rev. Lett. **99**, 050403 (2007).
[60] Y. Kato and N. Kawashima, Phys. Rev. E **79**, 021104 (2009).
[61] B. Capogrosso-Sansone, S. G. Söyler, N. Prokof'ev, and B. Svistunov, Phys. Rev. A **77**, 015602 (2008).
[62] B. Capogrosso-Sansone, M. Guglielmino, and V. Penna, Laser Phys. **21**, 1443 (2011).
[63] A. Griesmaier, J. Werner, S. Hensler, J. Stuhler, and T. Pfau, Phy. Rev. Lett. **94**, 160401 (2005).
[64] R. V. Pai and R. Pandit, Phys. Rev. B **71**, 104508 (2005).
[65] G. Mazzarella, S. Giampaolo, and F. Illuminati, Phys. Rev. A **73**, 013625 (2006).
[66] K. Yamamoto, S. Todo, and S. Miyashita, Phys. Rev. B **79**, 094503 (2009).
[67] M. Iskin and J. K. Freericks, Phys. Rev. A **79**, 053634 (2009).
[68] A. M. Rey, *Ultracold bosonic atoms in optical lattices*, PhD thesis, University of Maryland, 2004.
[69] J. Carrasquilla, *The Bose-Hubbard model with disorder in low-dimensional lattices*, PhD thesis, SISSA, 2010.
[70] K. Sheshadri, H. R. Krishnamurthy, R. Pandit, and T. V. Ramakrishnan, Europhys. Lett. **22**, 257 (1993).
[71] D. van Oosten, P. van der Straten, and H. T. C. Stoof, Phys. Rev. A **63**, 053601 (2001).
[72] B. C. Crooker, B. Hebral, E. N. Smith, Y. Takano, and J. D. Reppy, Phys. Rev. Lett. **51**, 666 (1983).
[73] L. Pollet, N. V. Prokof'ev, B. V. Svistunov, and M. Troyer, Phys. Rev. Lett. **103**, 140402 (2009).
[74] W. Krauth, N. Trivedi, and D. Ceperley, Phys. Rev. Lett. **67**, 2307 (1991).
[75] L. Zhang and M. Ma, Phys. Rev. B **45**, 4855 (1992).
[76] K. G. Singh and D. S. Rokhsar, Phys. Rev. B **46**, 3002 (1992).
[77] R. V. Pai, R. Pandit, H. R. Krishnamurthy, and S. Ramasesha, Phys. Rev. Lett. **76**, 2937 (1996).
[78] I. F. Herbut, Phys. Rev. Lett. **79**, 3502 (1997).
[79] P. Sen, N. Trivedi, and D. M. Ceperley, Phys. Rev. Lett. **86**, 4092 (2001).
[80] P. B. Weichman and R. Mukhopadhyay, Phys. Rev. B **77**, 214516 (2008).
[81] P. Buonsante, F. Massel, V. Penna, and A. Vezzani, Phys. Rev. A **79**, 013623 (2009).
[82] F. Krüger, J. Wu, and P. Phillips, Phys. Rev. B **80**, 094526 (2009).
[83] H. Lin, Phys. Rev. B **42**, 6561 (1990).
[84] J. Zhang and R. Dong, Eur. J. Phys. **31**, 591 (2010).
[85] W. Krauth, M. Caffarel, and J.-P. Bouchaud, Phys. Rev. B **45**, 3137 (1992).
[86] C. Schroll, F. Marquardt, and C. Bruder, Phys. Rev. A **70**, 053609 (2004).

[87] J. Zakrzewski, Phys. Rev. A **71**, 043601 (2005).
[88] R. V. Pai, J. M. Kurdestany, K. Sheshadri, and R. Pandit, Phys. Rev. B **85**, 214524 (2012).
[89] P. Sengupta, M. Rigol, G. Batrouni, P. Denteneer, and R. Scalettar, Phys. Rev. Lett. **95**, 220402 (2005).
[90] V. Kashurnikov, N. Prokof'ev, and B. Svistunov, Phys. Rev. A **66**, 031601(R) (2002).
[91] S. Wessel, F. Alet, M. Troyer, and G. G. Batrouni, Phys, Rev. A **70**, 053615 (2004).
[92] M. Capello, F. Becca, M. Fabrizio, and S. Sorella, Phys. Rev. Lett. **99**, 056402 (2007).
[93] M. Capello, F. Becca, M. Fabrizio, and S. Sorella, Phys. Rev. B **77**, 144517 (2008).
[94] J. Kurdestany, R. Pai, and R. Pandit, Ann. Phys. **524**, 234 (2012).
[95] L. Pollet, Rep. Prog. Phys. **75**, 094501 (2012).
[96] K. Sheshadri, H. R. Krishnamurthy, R. Pandit, and T. V. Ramakrishnan, Phys. Rev. Lett. **75**, 4075 (1995).
[97] T. McIntosh, P. Pisarski, R. J. Gooding, and E. Zaremba, Phys. Rev. A **86**, 013623 (2012).
[98] P. Jain and C. W. Gardiner, J. Phys. B: At., Mol. Opt. Phys. **37**, 3649 (2004).
[99] P. Buonsante, V. Penna, and A. Vezzani, Phys. Rev. A **70**, 061603 (2004).
[100] P. Buonsante, V. Penna, and A. Vezzani, Laser Phys. **15**, 361 (2005).
[101] P. Pisarski, R. M. Jones, and R. J. Gooding, Phys. Rev. A **83**, 053608 (2011).
[102] J. K. Freericks and H. Monien, Europhys. Lett. **26**, 545 (1994).
[103] F. E. A. dos Santos and A. Pelster, Phys. Rev. A **79**, 013614 (2009).
[104] W. L. McMillan, Phys. Rev. **138**, A442 (1965).
[105] D. Ceperley, G. Chester, and M. Kalos, Phys. Rev. B **16**, 3081 (1977).
[106] M. Kalos, Phys. Rev. **128**, 1791 (1962).
[107] M. C. Buonaura and S. Sorella, Phys. Rev. B **57**, 11446 (1998).
[108] G. Grynberg, B. Lounis, P. Verkerk, J.-Y. Courtois, and C. Salomon, Phys. Rev. Lett. **70**, 2249 (1993).
[109] K. S. Novoselov et al., Science **306**, 666 (2004).
[110] K. Novoselov et al., Nature **438**, 197 (2005).
[111] Y. Zhang, Y.-W. Tan, H. L. Stormer, and P. Kim, Nature **438**, 201 (2005).
[112] M. Boninsegni and N. Prokof'ev, Phys. Rev. Lett. **95**, 237204 (2005).
[113] L. Mathey, S.-W. Tsai, and A. H. Castro Neto, Phys. Rev. B **75**, 174516 (2007).
[114] C. Becker, P. Soltan-Panahi, J. Kronjger, S. Drscher, K. Bongs, and K. Sengstock, New J. Phys. **12**, 065025 (2010).
[115] S. Wessel, Phys. Rev. B **75**, 174301 (2007).
[116] B. Wunsch, F. Guinea, and F. Sols, New J. Phys. **10**, 103027 (2008).
[117] C. Wu, D. Bergman, L. Balents, and S. Das Sarma, Phys. Rev. Lett. **99**, 070401 (2007).
[118] C. Wu and S. Das Sarma, Phys. Rev. B **77**, 235107 (2008).
[119] F. S. Cataliotti, S. Burger, C. Fort, P. Maddaloni, F. Minardi, A. Trombettoni, A.

Smerzi, and M. Inguscio, Science **293**, 843 (2001).
[120] S. Burger, F. S. Cataliotti, C. Fort, P. Maddaloni, F. Minardi, and M. Inguscio, Europhys. Lett. **57**, 1 (2002).
[121] B. Damski, H. Fehrmann, H.-U. Everts, M. Baranov, L. Santos, and M. Lewenstein, Phys. Rev. A **72**, 053612 (2005).
[122] L. Santos, M. A. Baranov, J. I. Cirac, H.-U. Everts, H. Fehrmann, and M. Lewenstein, Phys. Rev. Lett. **93**, 030601 (2004).
[123] J. K. Block and N. Nygaard, Phys. Rev. A **81**, 053421 (2010).
[124] K. L. Lee, B. Grémaud, R. Han, B.-G. Englert, and C. Miniatura, Phys. Rev. A **80**, 043411 (2009).
[125] T. Hanisch, B. Kleine, A. Ritzl, and E. Müller-Hartmann, Ann. Phys. **507**, 303 (1995).
[126] K. Burnett, M. Edwards, C. W. Clark, and M. Shotter, J. Phys. B: At., Mol. Opt. Phys. **35**, 1671 (2002).
[127] A. O'Brien, F. Pollmann, and P. Fulde, Phys. Rev. B **81**, 235115 (2010).
[128] C. Fort, L. Fallani, V. Guarrera, J. E. Lye, M. Modugno, D. S. Wiersma, and M. Inguscio, Phys. Rev. Lett. **95**, 170410 (2005).
[129] T. Schulte et al., Phys. Rev. Lett. **95**, 170411 (2005).
[130] P. Vignolo, Z. Akdeniz, and M. P. Tosi, J. Phys. B: At., Mol. Opt. Phys. **36**, 4535 (2003).
[131] T. Giamarchi and H. J. Schulz, Phys. Rev. B **37**, 325 (1988).
[132] A. Aharony and D. Stauffer, *Introduction to percolation theory*, Taylor & Francis, 2003.
[133] B. M. Kemburi and V. W. Scarola, Phys. Rev. B **85**, 020501 (2012).
[134] H. Gould, J. Tobochnik, W. Christian, and E. Ayars, *An introduction to computer simulation methods: applications to physical systems*, volume 1, Addison-Wesley Reading, 1988.
[135] The proportionality holds strictly in one dimension. In higher dimensions, the relationship is more complicated.
[136] K. V. Krutitsky, A. Pelster, and R. Graham, New J. of Phys. **8**, 187 (2006).
[137] S. Chakravarty, Int. J. Mod. Phys. B **24**, 1823 (2010).
[138] We choose the value μ (or U) such that we are at the vicinity of the MI-SF boundary and thus can access all the three *viz.* SF, BG and MI phases distinctly.
[139] E. Kreyszig, *Advanced engineering mathematics*, John Wiley & Sons, 2007.
[140] H.-C. Jiang, L. Fu, and C. Xu, Phys. Rev. B **86**, 045129 (2012).
[141] J.-Y. Ye, V. Mizeikis, Y. Xu, S. Matsuo, and H. Misawa, Opt. Comm. **211**, 205 (2002).
[142] Z. Chen and B. Wu, Phys. Rev. Lett. **107**, 065301 (2011).
[143] L. Tarruell, D. Greif, T. Uehlinger, G. Jotzu, and T. Esslinger, Nature **483**, 302 (2012).
[144] G.-B. Jo, J. Guzman, C. K. Thomas, P. Hosur, A. Vishwanath, and D. M. Stamper-

Kurn, Phys. Rev. Lett. **108**, 045305 (2012).
[145] D. Yamamoto, I. Danshita, and C. A. R. Sá de Melo, Phys. Rev. A **85**, 021601 (2012).
[146] S. V. Isakov, K. Sengupta, and Y. B. Kim, Phys. Rev. B **80**, 214503 (2009).
[147] A. A. Burkov and E. Demler, Phys. Rev. Lett. **96**, 180406 (2006).
[148] M. Iskin, Phys. Rev. A **83**, 051606 (2011).
[149] U. Bissbort and W. Hofstetter, Europhys. Lett. **86**, 50007 (2009).
[150] J. Ruostekoski, Phys. Rev. Lett. **103**, 080406 (2009).
[151] P. Dean, Math. Proc. Cam. Phil. Soc. **59**, 397 (1963).
[152] B. Krishna and C. K. Majumdar, Pramana - J. Phys. **20**, 73 (1983).
[153] T. A. Zaleski and T. K. Kopeć, Phys. Rev. A **84**, 053613 (2011).
[154] G. K. Walters and W. M. Fairbank, Phys. Rev. **103**, 262 (1956).
[155] E. H. Graf, D. M. Lee, and J. D. Reppy, Phys. Rev. Lett. **19**, 417 (1967).
[156] G. Modugno, M. Modugno, F. Riboli, G. Roati, and M. Inguscio, Phys. Rev. Lett. **89**, 190404 (2002).
[157] T.-L. Ho and V. B. Shenoy, Phys. Rev. Lett. **77**, 3276 (1996).
[158] B. D. Esry, C. H. Greene, J. P. Burke, Jr., and J. L. Bohn, Phys. Rev. Lett. **78**, 3594 (1997).
[159] E. Timmermans, Phys. Rev. Lett. **81**, 5718 (1998).
[160] H. Pu and N. P. Bigelow, Phys. Rev. Lett. **80**, 1134 (1998).
[161] F. Riboli and M. Modugno, Phys. Rev. A **65**, 063614 (2002).
[162] J. P. Burke, J. L. Bohn, B. D. Esry, and C. H. Greene, Phys. Rev. Lett. **80**, 2097 (1998).
[163] G. Modugno, G. Ferrari, G. Roati, R. Brecha, A. Simoni, and M. Inguscio, Science **294**, 1320 (2001).
[164] M. Kitagawa, K. Enomoto, K. Kasa, Y. Takahashi, R. Ciuryło, P. Naidon, and P. S. Julienne, Phys. Rev. A **77**, 012719 (2008).
[165] K. Kasamatsu and M. Tsubota, J. Low Temp. Phys. **150**, 599 (2008).
[166] G.-H. Chen and Y.-S. Wu, Phys. Rev. A **67**, 013606 (2003).

Vita

Apurba Barman was born on 27th November 1985 in West Bengal, India. He did his B.Sc. with Physics Honours in 2007 from Dinhata College, under University of North Bengal, Siliguri and M.Sc. in Physics from Indian Institute of Technology Guwahati, Guwahati in 2009. He enrolled into the Ph.D programme at Indian Institute of Technology Guwahati in 2009. He qualified both Graduate Aptitude Test in Engineering (GATE) and CSIR-UGC NET in 2009. He earned the Senior Research Fellowship in 2011 by Indian Institute of Technology Guwahati, Guwahati.